HIGH-FREQUENCY TRI-AXIAL RESONANT GYROSCOPES

A Dissertation
Presented to
The Academic Faculty

by

Wang-Kyung Sung

In Partial Fulfillment
Of the Requirements for the Degree
Doctor of Philosophy in the
School of Electrical and Computer Engineering

Georgia Institute of Technology

December 2013

HIGH-FREQUENCY TRI-AXIAL RESONANT GYROSCOPES

Approved by:

Dr. Farrokh Ayazi, Chair, Advisor
School of Electrical and Computer Engineering
Georgia Institute of Technology

Dr. Pamela T. Bhatti
School of Electrical and Computer Engineering
Georgia Institute of Technology

Dr. Mark G. Allen, Co-advisor
School of Electrical and Computer Engineering
Georgia Institute of Technology

Dr. Madhavan Swaminathan
School of Electrical and Computer Engineering
Georgia Institute of Technology

Dr. Oliver Brand
School of Electrical and Computer Engineering
Georgia Institute of Technology

Dr. Paul Kohl
School of Chemical and Biomolecular Engineering
Georgia Institute of Technology

Date Approved: 8/19/2013

I dedicate this dissertation to my family.

ACKNOWLEDGEMENTS

I would like to deliver my gratefulness to my advisor and mentor, Dr. Farrokh Ayazi, for his incessant dedication to his students, research projects, and guidance to constitute this dissertation. Without his encouragement, my expertise and knowledge toward the accomplishment of the research would never be attained. In addition, the source of inspiration transferred from Dr. Ayazi's vision to my deep mindset will go throughout my entire life regardless of the level of challenges and hardship in the future duties. I hope to thank to my dissertation committee professors, Dr. Mark G. Allen, Dr. Oliver Brand, Dr. Pamela T. Bhatti, Dr. Madhavan Swaminathan, and Dr. Paul Kohl for evaluating and providing valuable comments on my work spending their precious time.

I also hope to express my sincere gratitude to my senior, Dr. Mohammad Faisal Zaman, for his uncountable ideas on MEMS designs and thorough supports towards the completion of the projects. In addition, I would like to mention my colleague, Dr. Ashwin Kumar Samarao and Dr. Wanling Pan, who gave massive fabrication skills and techniques. Without their solid companionship with badminton plays, tons of coffees drank together, and exhaustive discussions on every topic, I cannot think this dissertation could be finished. Also, I hope to remark my senior friend, Dr. Milap Jayesh Dalal, with highlighted voice for his patience helping all of the complicated measurements as well as chatting all the time to forget the stressfulness and bores. They converted my entire graduate-years to full of fun and learning. I would like to express my gratefulness to the IMEMS group, which has been another home for the many years, and every single person should be appreciated. Gary Spinner, Vinh Nguyen, William Kimes, Eric Woods, and all

nano-research center (NRC) staffs should deserve plenty of thankfulness for helping all of equipment kept up and running all the time, especially in the presence of numerous deadlines, that could never be possible without their dedicated helps.

In addition, I thank people at Qualtré Inc., Mr. Edgar Masri for offering my internship opportunity and leading the company with great deal of enthusiasm, Dr. Ijaz Jafri for allowing various experiment materials with very considerate cares toward all people, Mr. Craig Core for teaching me his life-long expertise in fabrication technologies and incessant curiosities in the emerging MEMS processes, Varun Keesara for his kind demonstrations and discussions on the fabrication process and professional foundry layout techniques, and Diego Serrano for helping the measurements done at Qualtré Inc.

Lastly, I thank my family and Dr. Jinmi Heo for their invaluable supports and encouragements. The only reason I could survive with sound mindset was from their profound wisdom and lesson that made me feel full of love and affection.

TABLE OF CONTENTS

LIST OF TABLES

LIST OF FIGURES

SUMMARY

Microelectromechanical systems (MEMS) gyroscopes are attractive alternatives to conventional mechanical gyroscopes and fiber-optical gyroscopes because of their small size, low cost, low power consumption, and integration capability. The application domains of the devices have expanded from the traditional realms of inertial sensors, which are automotive and aerospace, to the emerging consumer electronics markets. When gyroscopes with tri-axial rotation-sensing capability are integrated with tri-axial accelerometers, six degrees-of-freedom (DoF) motion recognition is realized for the accurate positioning of an object, thus retaining the attributes required for the precise inertial navigation systems (INS).

This dissertation reports on the design and implementation of a high-frequency, tri-axial capacitive resonant gyroscopes integrated on a single chip. The components that construct tri-axial rotation sensing consist of a yaw, a pitch and a roll device. The yaw-rate gyroscope has a wide bandwidth and a large full-scale range, and operates at a mode-matched condition with DC polarization voltage of 10V without frequency tuning requirement. The large bandwidth of 3kHz and expected full-scale range over 30,000 $^{\circ}$/sec make the device exhibit fast rate response for rapid motion sensing application. For the pitch-and-roll rate sensing, an in-plane drive-mode and two orthogonal out-of-plane sense modes are employed. The rotation-rate sensing from lateral axes is performed by mode-matching the in-plane drive-mode with out-of-plane sense-modes to detect Coriolis-force induced deflection of the resonant mass. To compensate process variations and thickness deviations in the employed silicon-on-insulator (SOI) substrates, large

electrostatic frequency tunings of both the drive and sense modes are realized. A revised high aspect ratio combined polysilicon and silicon (HARPSS^{TM}) process is developed to resolve the Coriolis response that exists toward out-of-plane direction while drive-mode exists on in-plane, and tune individual frequencies with minimal interference to unintended modes.

The primary emphases of this thesis are laid on

(a) operating tri-axial gyroscopes in high-frequency regime with high Q-factors while maintaining large bandwidth to ensure fast sensor response,

(b) eliminating the necessity and challenge in the frequency tuning of a yaw-rate gyroscope with low DC voltage of 10V,

(c) providing the yaw gyroscope with wide full-scale range for rapid motion sensing applications,

(d) achieving sufficient electrostatic frequency tuning for a high-frequency pitch-and-roll annulus gyroscope to guarantee mode-matched operation in the presence of process variations,

(e) creating an integrated tri-axial resonant gyroscopes in a small form factor comparable to commercialized non-resonant silicon gyroscopes available in the market,

(f) and developing a fabrication process platform that can yield tri-axial accelerometers as well as tri-axial gyroscopes to integrate 6 DoF inertial measurement unit (IMU).

To conclude and overcome the performance limitation, design optimization of high-frequency tri-axial gyroscopes is suggested. Q-factor enhancement through

reduction of thermoelastic damping (TED) and optimizations of physical dimensions are suggested for the yaw disk gyroscope. For the pitch-and-roll gyroscope, scaling property of physical dimension and its subsequent performance enhancement are analyzed.

CHAPTER 1

INTRODUCTION

1.1. Tri-axial Gyroscopes in the Market

The motion and position of an object in three-dimensional space can be accurately identified through inertial measurement unit (IMU) which consists of tri-axial gyroscopes and tri-axial accelerometers [1-4]. The tri-axial gyroscopes offer the information on the angle of rotation applied to the system while tri-axial accelerometers measure the linear velocity that the system is undergoing. By integrating the angular velocity given from gyroscopes and linear velocity provided by accelerometers, precise heading information and location of the system in the three-dimensional space can be accurately calculated.

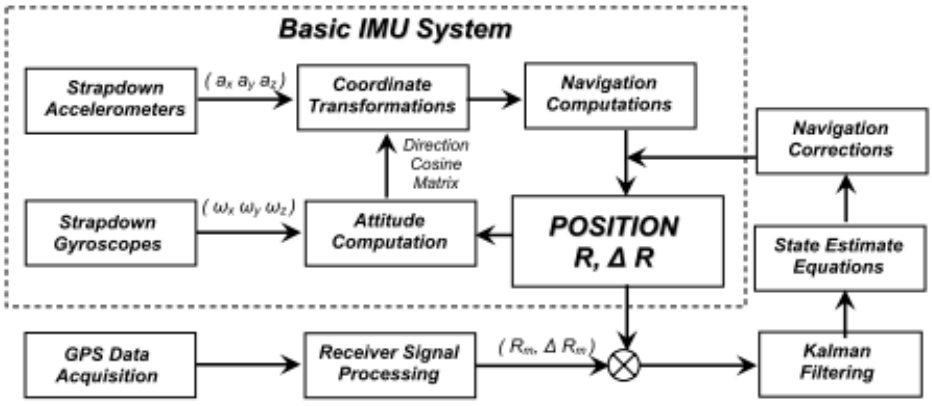

Figure 1: Basic diagram of IMU system.

Figure 1 shows a typical diagram of the IMU system. In traditional applications, IMUs have been equipped in space shuttles, satellites, and ballistic missiles to provide heading and trajectory information without the assistance from GPS signals. Because of

the required high resolution with low noise performance, mechanical gyroscopes and optical gyroscopes (Figure 2) have been used for the aforementioned high-performance application categories.

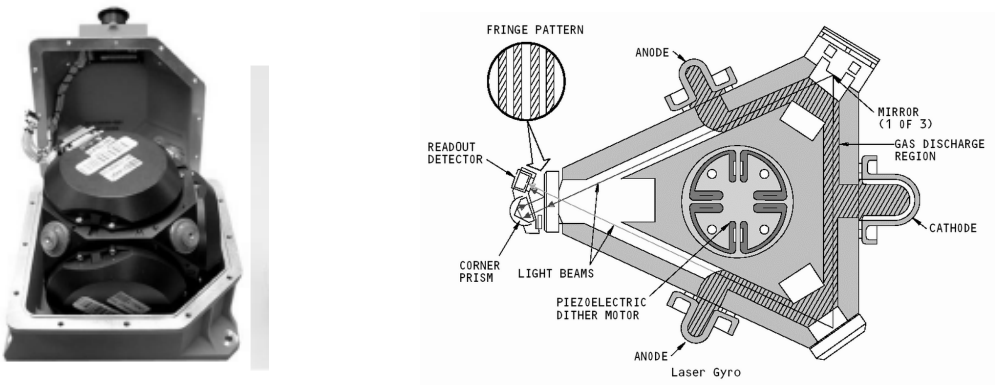

Figure 2: Mechanical spinning wheel gyroscope (left) and optical gyroscope (right).

Due to the recent development in micromachining technology, miniaturization of microelectromechanical systems (MEMS) gyroscopes has been successfully fulfilled. For example, the introduction of accurate silicon deep reactive ion etching (DRIE) method represented by “Bosch Process” helped shaping the micro-scale devices with accurate dimension, while precise lithography process enhanced the accuracy of the transferred patterns to the substrate.

Although the resolution and bias stability of MEMS gyroscopes have not been comparable to the mechanical and optical gyroscopes yet, the small form factor and low power consumption with cheap manufacturing costs let the application domains of MEMS gyroscopes expand to various consumer electronics during the past decades. For instance, the angular velocity information from MEMS gyroscopes enables motion-tracking of the gaming consoles and remote controllers. In addition, low-noise

gyroscopes can resolve trembling of hands to reject vibration noise components injected to the digital cameras (Figure 3).

Figure 3: Illustrations of exemplary MEMS gyroscopes applications.

1.2. Motivation

The objective of this dissertation is to investigate the design, fabrication, and implementation of high-Q, high-frequency, mode-matched tri-axial resonant capacitive gyroscopes. To perform the given tasks, pitch-and-roll gyroscope is integrated with yaw gyroscope through a revised high aspect ratio combined polysilicon and silicon (HARPSS^{TM}) [5, 6] fabrication platform called HARPSS^{TM} ver.4 [7, 8].

The tri-axial capacitive gyroscopes provide a novel approach to realize low mechanical noise floor integrated in a planar configuration. All the three axes devices operate in high-frequency regime to reduce Brownian noise and reject environmental noises [6, 9]. The mode-matched high Q-factors amplify the Coriolis signals in the mechanical domain while the large bandwidth ensures fast sensor response. The planar configuration of devices obviates the angular offset error that can possibly exist if the devices are integrated in a three-dimensional assembly process [7, 8]. In addition, to address process variations existing in the silicon-on-insulator (SOI) substrates, the pitch-

and-roll gyroscopes retain wide frequency tunabilities in each resonance mode while yaw gyroscope has large bandwidth to cover initial frequency split. The process platform, HARPSS^{TM} ver.4, is introduced to broaden and enhance the frequency tunabilities, minimize cross-axis tuning behavior, improve signal isolation between each resonance mode, minimize the quadrature signal component fed through the sense electrode, and integrate tri-axial accelerometers in the same substrate. To integrate IMU in a single chip, tri-axial gyroscopes and accelerometers are integrated and wafer-level packaged. The overall packaging size is proven to be comparable or smaller than commercial IMUs available in the market.

1.3. Dissertation Organization

This dissertation is organized into six chapters. **Chapter 1** summarizes application domains and the market demands and presents motivation behind this research. **Chapter 2** briefly introduces the history of MEMS gyroscopes from the literature based on design and performance followed by commercial multi-axes gyroscopes in the market. **Chapter 3** explains the research works performed for yaw gyroscope. The design strategy and analysis of the high-frequency mode-matched gyroscope are presented with ANSYS Workbench^{TM} simulations. HARPSS^{TM} process is briefly described to explain the fabrication process, and the characterization results are reported. For the performance enhancement of yaw gyroscopes, Q-factor enhancement and optimization of physical dimensions are suggested with the combination of ANSYS Workbench^{TM} and Comsol multiphysics simulations. **Chapter 4** introduces high-frequency pitch-and-roll annulus gyroscopes. Starting from the analysis of annulus gyroscopes, the first part demonstrates the single proof-mass dual-axes gyroscope

operating in mode-matched condition with three resonance modes. The improved design with eliminated cross-axis sensitivity and reduced mechanical noise is shown in the second part of the chapter. The revised version of HARPSS^{TM} process is developed and introduced as an IMU integration platform. **Chapter 5** delivers the contribution of this work with a brief summary and future direction of inertial sensors with design optimization.

CHAPTER 2

REVIEW OF MEMS GYROSCOPES

2.1. Origin of Gyroscope

The word "gyroscope" originated from Greek words "Gyros" which means rotation and "Skopeein" that stands for measurement. By its definition, gyroscope is an apparatus devised to measure the quantity of rotation angle or rotation rate applied to a system. In 1651, an Italian ancient artillery technical manual, Almagestum Novum, described that the rotation of the earth causes a deflection of a cannon ball to east when fired to the north. The first instrument using gyroscope was invented in 1817 by a German astronomer, Johann Bohnenberger, and the first gyroscopic effect was verified by a French physicist, Leon Foucault, by measuring the rotation of the earth using a swinging pendulum. In 1835, a French mathematician, Gaspard-Gustave Coriolis, first explained about the theory on the deflection of a moving object in a rotating system, and named it "Coriolis effect". Since the experimental verification and establishment of the theory on the Coriolis effect, gyroscopes have been developed and equipped in myriad of devices encompassing navigation systems for aerospace and missile guidance.

The early research on gyroscopes had been performed in mechanical gyroscopes that use spinning-wheels and optical gyroscopes that measure interference patterns of light to detect rotation rates and angles [10, 11]. However, the bulky scale, large power consumption, and expensive manufacturing costs restricted application areas narrowly scoped in aerospace and missile guidance. Because of recent developments in micromachining technologies, the attempts to miniaturize gyroscopes have been

successfully fulfilled. MEMS gyroscopes, which retain resonating proof mass without bulky spinning mechanical parts and optical fiber assembly, emerged as a promising alternative type for the gyroscopic devices. Their small form factor, low power consumption, and batch-fabrication capability enabled the gyroscopes to be equipped in various gadgets such as automotive applications, image stabilization for digital cameras, and smart user interfaces equipped in mobile devices.

2.2. General Operation Principle of MEMS Gyroscopes

Resonant gyroscopes utilize two resonant modes, i.e. drive and sense-modes, existing in a mechanical element to transfer Coriolis force. The modes can exist in the same structure or can also be mechanically decoupled to isolate the vibration of drive mode from sense mode. The Coriolis force is an acceleration-induced fictitious force ($\vec{a}_{cor}$) generated in a rotating frame ($\vec{\Omega}_Z$) when an object is in a linear motion ($\vec{v}$) as expressed below:

$$\vec{F}_{cor} = M \cdot \vec{a}_{cor} = M \cdot \left(2 \cdot \vec{v} \times \vec{\Omega}_Z\right) \quad \textbf{(1)}$$

In all types of resonant gyroscopes, a drive resonance mode is excited in a finite mass (M) to induce the linear velocity ($\vec{v}$), then a sense resonance mode is generated in response to the applied angular-rate ($\vec{\Omega}_Z$), as shown in Figure 4. The examples of the resonant gyroscopes include resonating-ring gyroscopes [1, 5, 12, 13], resonating star gyroscopes (RSG) [14, 15], hemispherical resonating gyroscopes (HRG) [16, 17], cylindrical gyroscope [18], tuning-fork gyroscopes (TFG) [19, 20], bulk-acoustic-wave (BAW) disk gyroscopes [6, 9], and annulus resonant gyroscopes [8, 21-24].

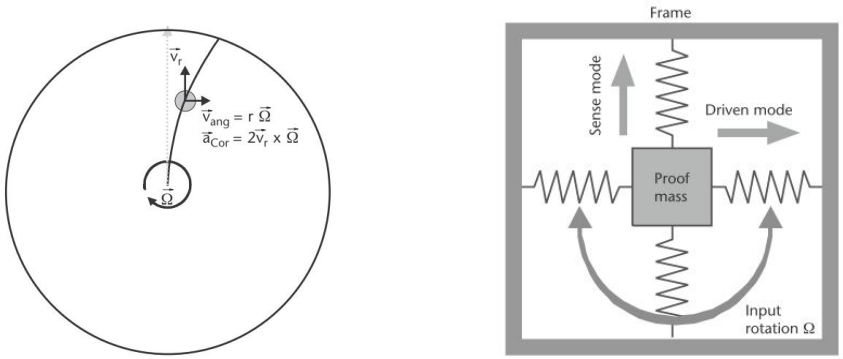

Figure 4: (a) Illustration of Coriolis-force transfer in a rotating frame, and (b) drive and sense-modes oscillation in a resonant gyroscope.

The resonant gyroscopes can magnify Coriolis-force induced signal component through their mechanical quality (Q) factor of the sense mode in the mechanical domain, and therefore can achieve high sensitivity without increasing the size of proof-mass and driving amplitude. The properties and advantages of mode-matched operation in tri-axial gyroscopes will be further discussed in this dissertation.

2.3. History of MEMS Gyroscopes

Initially, researchers investigated surface micromachining of the vibratory gyroscopes using 1-10μm-thick silicon and polysilicon substrates. The thin-layer processing was an inevitable option because of immature micromachining process and its convenience in interfacing with readout circuitry. However, surface micromachining of the thin material limited the volume of resonant mass and capacitive transduction area leading to restricted performance parameters in scale factor and mechanical noise, especially. In addition, reliability issues caused by residual thin-film stress exhibited significant drawbacks in long-term stability as well as large temperature-dependent performance drifts by thermoelastic damping. Bulk micromachining was then introduced as a result of the development in deep reactive ion etching (DRIE) technology by means

of Bosch process and the introduction of silicon-on-insulator (SOI) substrates. Due to the excellent etch-stops using SOI wafers to define the height of mechanical structures during Bosch process, bulk micromachining enabled patterning and shaping of thick silicon substrates typically in 10-100μm range. Therefore, large effective mass and capacitive transduction area could be achieved to yield improved mechanical noise level and Coriolis-force induced output signal. In addition, long-term reliability issues caused by thin-film materials were eliminated.

In this section, the MEMS gyroscopes categorized based on the basic structures and operating principles are presented. Commercially available MEMS gyroscopes and performance summary are described with a brief explanation.

2.3.1. Gimbaled Frame Gyroscope

Greiff et al. at Charles Stark Draper Laboratory, reported the first MEMS silicon yaw vibratory gyroscope in 1991 (Figure 5, left) [25]. The sensor had a proof mass sustained by two torsional gimbaled structures. The inner gimbal was designed to bend toward sensing electrodes when input rotation is applied to the vibrating mass sustained by outer gimbal. Two years later, in 1993, Greiff et al. reported capacitive gyroscope actuated by comb-drive [26]. The structure was established by electrostatic bonding of patterned silicon substrate on glass wafer. In 1996, Clark and Howe introduced the first surface micromachined polysilicon tuning-fork gyroscope (Figure 5, right) [27]. The 2μm-thick polysilicon proof-mass was excited by capacitive comb-drive to induce large deflection in drive-mode to augment $\vec{v}$, and Coriolis-force induced output signal was sensed via capacitive parallel plate.

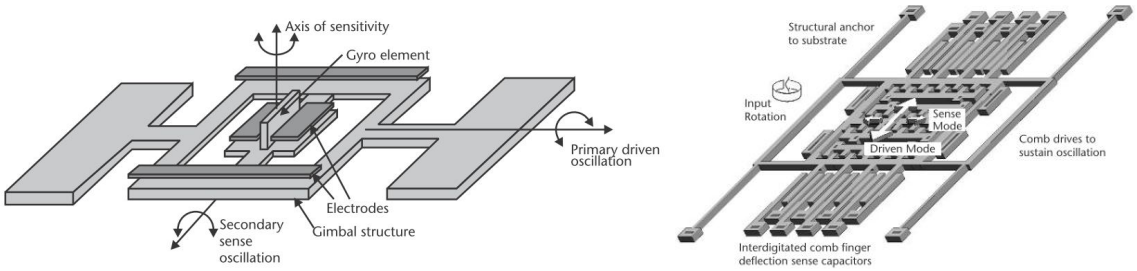

Figure 5: Schematic and operation of the first MEMS gyroscope (left) and the first polysilicon gyroscope (right).

Interestingly, the first lateral-axis gyroscope, i.e. x/y-axis or pitch/roll sensing elements, was introduced using the gimbaled structure in 1997 by Juneau et al (Figure 6 (left)) [28]. It had axis-symmetric resonant mass sustained by silicon beams arranged in radial direction, and excited into rotary modes at 28.2kHz to create drive mode. The capacitive sensing was done through bottom electrodes by detecting the tilting of the resonant mass to out-of-plane direction. The patterned bottom electrodes could sense input rotation rate from x- and y-axes with cross-axis sensitivity of 3-16 % depending on the frequency matching condition.

A single-lateral axis gyroscope processed using surface micromachining was introduced in 1999 by Geiger et al. (Figure 6 (right)) [29]. The structure was made from epitaxially grown polysilicon, and had bottom electrodes to sense out-of-plane Coriolis response. The rotary drive mode is excited by comb-drive, and the sensing signal is detected through electrodes underneath the vibrating mass. Because the structure is constrained by rigid tether at the direction of unwanted sensing axis, the cross-axis sensitivity and quadrature signal was mechanically suppressed.

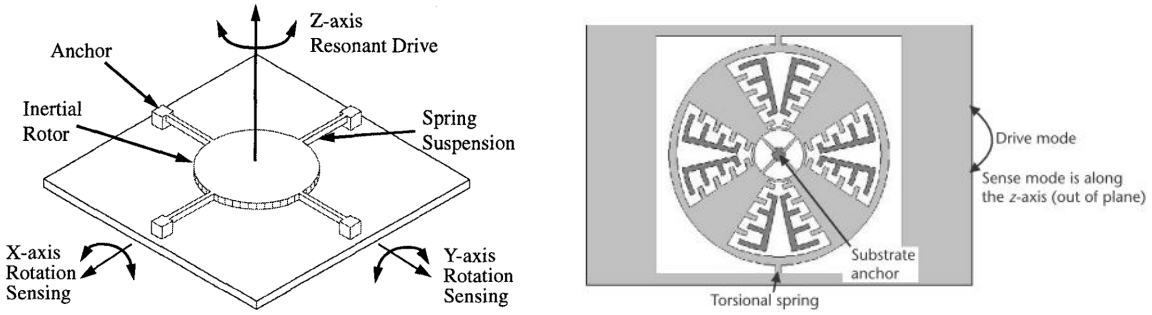

Figure 6: Schematic of dual-axes gyroscope and single lateral-axis gyroscope.

2.3.2. Beam Gyroscopes

A beam with square-shaped cross-section has natural mode-matched frequency that can transfer Coriolis force from principle axis of a resonance mode to another mode. The operating principle can be explained in an identical way with Foucault pendulum except for using a long bar instead of a stretched wire. In general, the closed-loop sensing using a force-rebalance architecture is introduced to readout Coriolis signals to offer increased operational bandwidth [30-35].

Figure 7 shows two typical designs introduced for beam gyroscopes. The prismatic mass is erected on a planar substrate, and the mass is excited into a swinging drive resonance mode. When rotation is applied, the precession of the drive-mode deflects the mass toward its orthogonal direction, and then the system detects rotation rates based on the mechanical deformation. The decoupled vibrating direction of two modes by directional stiffness of the structure can significantly improve quadrature signal due to suppressed mechanical coupling. Both capacitive and piezoelectric sensing are in use depending on the process [30, 31].

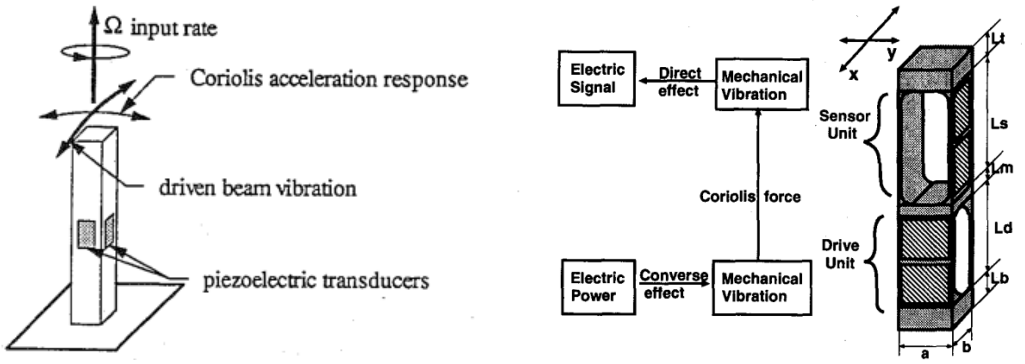

Figure 7: Schematics of exemplary beam gyroscopes.

2.3.3. Gas-convection Gyroscopes

Instead of using mechanical vibration of a resonant mass to detect Coriolis signal by detecting the dislocation or deformation of the proof-mass, a deflection in the heated gas flow can be employed to sense the rotation rate [36-39]. In the gas convection gyroscopes, inert gas, micro-heater, micro- pump, and thermistors are assembled in an isolated package (Figure 8). While the pump is creating a constant linear velocity of the inert gas inside a metallic package, the gas is ejected through the narrow heated nozzle. The hot gas flow is deflected from its normal trajectory when a rotation is applied, and the thermistors detect the amount of deflection in the gas flow and converts it to the output signal.

However, the expensive assembly process and bulky package size are inadequate for most applications, and the environmental susceptibilities, such as temperature variation, remain to be improved.

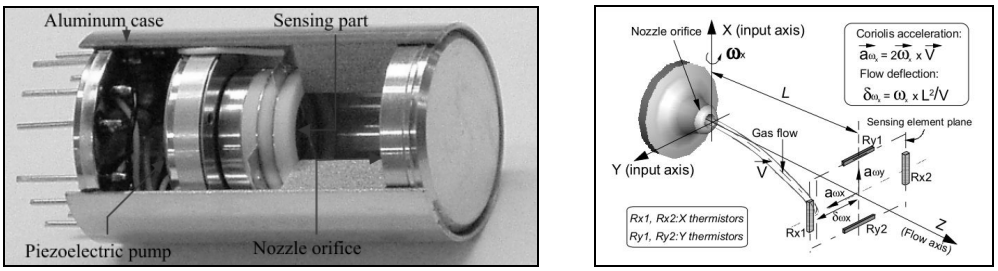

Figure 8: Packaged gas convection gyroscope (left) and operating principle (right).

2.3.4. Tuning Fork Multiple Resonant Mass Gyroscopes

The performance of MEMS gyroscopes is easily improved by adapting large driving deflection and enhanced proof-mass sizes. Tuning fork gyroscopes employ proof-masses sustained by flexural beams, and the drive-mode resonance is usually excited through comb-drive to achieve large driving amplitude. The proof-masses are bulk micromachined to retain large mass for the reduced mechanical noise level.

The first tuning-fork architecture was introduced in 1997 by Lutz et al [40]. It had two epitaxially-grown 12μm-thick polysilicon proof-masses sustained by narrow springs. The electromagnetic excitation and capacitive sensing could satisfy criteria for automotive application. Acar et al. introduced a robust tuning fork architecture with broadened drive-mode bandwidth by incrementally spaced resonance frequencies in 2005 [41]. By electrical trimming procedure, the bandwidth could be increased to improve system response and compensate photolithography-based fabrication processes. Zaman et al. developed a mode-matching of resonance modes in tuning fork gyroscopes (Figure 9 (left)) [19, 20, 42]. The mode-matched tuning fork gyroscope could demonstrate sub-˚/hr Allan bias instability (AVAR) and Coriolis response by Q-times amplification in mechanical domain, which drove the device as a promising replacement for expensive mechanical gyroscopes. Quadruple mass tuning fork gyroscope with extreme high-Q in

excessive of 1 million was developed in 2010 (Figure 9 (right)) [43-47]. The extreme high-Q nature of the device appeared as a miniaturized Foucault pendulum to operate in whole angle mode with protracted ring-down time constant.

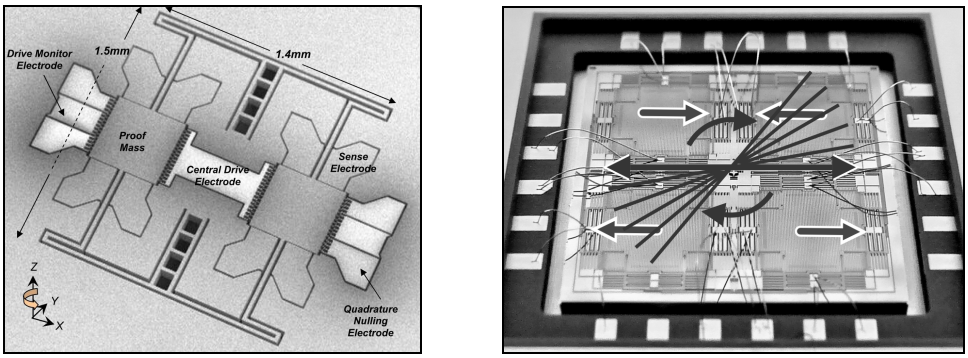

Figure 9: M^2-TFG (left) and QMG (right).

2.3.5. Axis-symmetric Shell-type Gyroscopes

Shell-type gyroscopes employ a center-supported axis-symmetric resonant mass with two resonant modes that are naturally mode-matched at an identical frequency [5, 12, 14, 48]. The resonant modes are from the same in-plane eigen-modes and the two resonant frequencies are tracking each other under process variation, temperature drift, and even different pressure level.

The initial shell-type gyroscope had wine-glass shape with elliptical modes as described in Figure 10. To minimize the loss through the anchor, the hemispherical resonant mass is supported at the center where vibration does not occur. Coriolis-force induced deformation is obtained based on the sense-mode amplitude that is proportional to the input rotation rate.

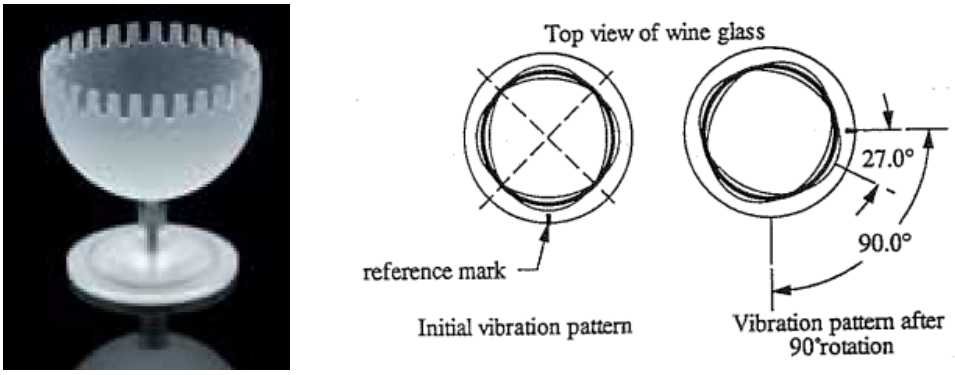

Figure 10: Resonating part of HRG made from quartz (left) and principle resonance modes (right).

The miniaturized types of shell-type gyroscopes have been developed due to the development of micromachining process. Figure 11 shows polysilicon multiple-shell ring resonating gyroscope [12] and star gyroscope [14]. The employed sub-micron capacitive gap defined by HARPSS^{TM} process [5] efficiently increases signal transduction.

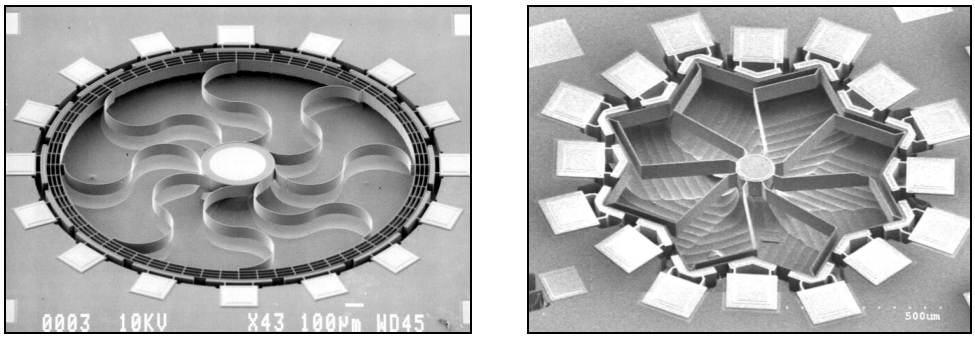

Figure 11: Multiple shell ring gyroscope (left) and resonating star gyroscope (right).

2.3.6. Bulk-acoustic Wave (BAW) Disk Yaw-rate Gyroscopes

A solid-disk made from single-crystal-silicon (SCS) with center-supported structure can operate in a similar way as shell-type gyroscopes [6, 9, 49]. The axis-symmetric disk has eigen-modes with near-zero initial frequency split depending on the orientation of the substrate silicon wafer. For (100) substrate, the anisotropy of in-plane

direction makes N=3 secondary elliptical in-plane resonance modes have mode-matched behavior, while (111) substrate can operate at N=2 primary elliptical in-plane modes to be used to transfer Coriolis-force.

The high-frequency operation of the device reduces the Brownian noise level several orders lower compared to low-frequency gyroscopes, and also acoustic interference caused by audile frequency and environmental vibration are effectively rejected in the mechanical domain. In addition, large capacitance created by sub-micron air gap and large capacitive surface area causes efficient signal transduction. Furthermore, the silicon with bulk-acoustic modes exhibit high-Q behavior enabling large sensitivity without the need for increasing the size of proof-mass.

Figure 12 shows the SEM picture of BAW disk gyroscope made from (100) substrate and its modes of operation. Twelve electrodes with sub-micron capacitive air gaps are employed around the disk to drive, sense, and tune N=3 elliptical modes.

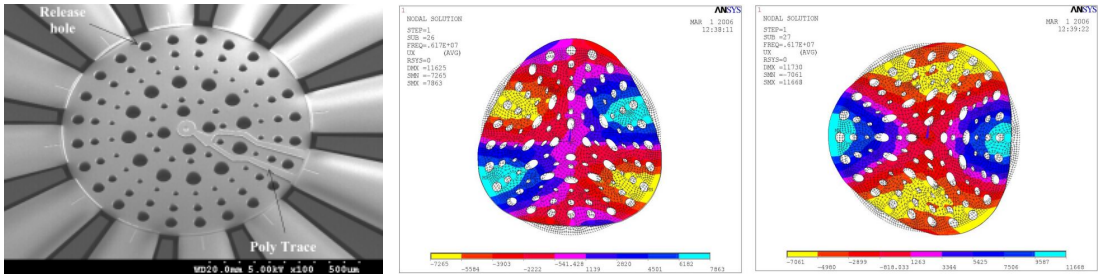

Figure 12: SEM picture of BAW disk gyroscope (left) and resonance modes (right).

2.3.7. Annulus Gyroscopes

Although BAW disk gyroscopes can configure high-performance Z-axis gyroscope with low mechanical noise, the device cannot sense input-rotation rate from lateral axes due to the in-plane modes of operation.

For lateral-axes sensing, drive and sensing resonance modes should exist in perpendicular direction with respect to the axis of rotation. Figure 13 shows the comparison between the yaw gyroscopes and lateral-axes gyroscopes [1, 8]. Yaw gyroscopes employ drive resonant mode existing in-plane of the substrate, and the applied input rotation transfers Coriolis force to sense mode vibrating on the same plane. Since both resonance modes exists in-plane, frequency mode-matching can easily be achieved using its degenerate behavior, if axis-symmetric proof-mass is employed. On the other hand, lateral-axes gyroscopes have a drive resonant mode on in-plane and sense mode to out-of-plane direction or vice versa. The non-degenerate property of the resonance modes places difficulties in achieving mode-matched behavior in the presence of imperfection of the device dimension.

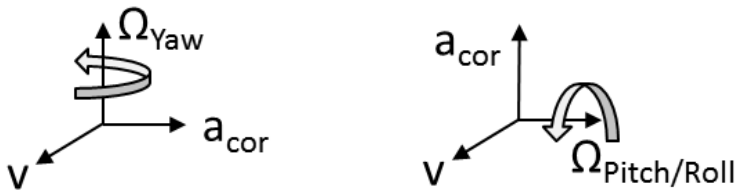

Figure 13: Orthogonal resonance modes and direction of input rotation rate comparison between yaw gyroscope and pitch-and-roll gyroscope.

The annulus gyroscope is developed to sense the rotation rate from x- and y-axes [1, 8, 22, 23, 50, 51]. The device has an annulus mass with capacitive electrodes (Figure 14 (left)) and employs three resonance modes matched at an identical frequency (Figure 14 (right)). The large frequency tunability using electrostatic spring softening effect enables stable yield under process variation and imperfection of the device after fabrication. In addition, the device inherits the benefit of high-frequency BAW disk

gyroscopes due to its operating frequency and high-Q behavior. In addition, the fabrication platform can yield BAW disk gyroscopes to realize tri-axial configuration of the device. Further specifics will be discussed in this dissertation.

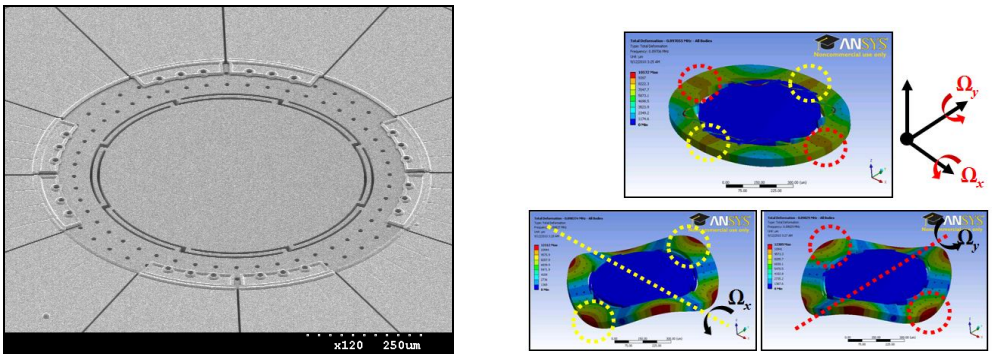

Figure 14: SEM picture of annulus gyroscope (left) and resonant mode-shapes (right).

2.4. Gyroscope Performance Parameters

Several critical factors determine the grades and classes of the MEMS gyroscopes as shown in Table 1 [2]. Sensitivity, cross-axis sensitivity, scale-factor accuracy, full-scale range (FSR), angle-random-walk (ARW), Allan-variance (AVAR) bias stability, bandwidth, and shock tolerance are the typical aspects of importance when the gyroscope devices are categorized based on the performance.

Table 1: Gyroscope performance classifications.

Parameter	Rate	Tactical	Inertial
Scale-factor accuracy, %	0.1-1	0.01-0.1	< 0.001
Full-scale range (˚/sec)	50-1,000	> 500	> 400
Angle-random-walk, ˚/√h	> 0.5	0.5-0.05	< 0.001
Allan-variance bias stability, ˚/h	10-1,000	0.1-10	< 0.01
Bandwidth, Hz	> 70	-100	~100
Maximum shock in 1msec, g's	10^3	10^3-10^4	10^3

2.4.1. Sensitivity, Cross-axis Sensitivity, and Scale-factor Accuracy

Sensitivity represents strength of the output signal from a gyroscope in response to the applied rotation-rate measured at room-temperature (25°C) [52, 53]. Because of the expected linear response in the output signal with respect to the applied rotation-rate, the sensitivity is frequently referred to as "scale-factor (SF)". As capacitive gyroscopes have output signals due to changes in voltage, the unit is denoted as mV/deg/sec, typically. In a gyroscope system with digital output signal, sensitivity is frequently denoted as a change in input rotation-rate that corresponds to one least significant bit (LSB) change in output (dps/LSB).

Cross-axis sensitivity means unwanted output signals induced by wrong axes of rotation. For example, when a gyroscope has a tri-axial rotation-sensing capability, and the input rotation-rate is applied from the pitch, the output signals observed from roll- and yaw sensing terminals are defined as the cross-axis sensitivity. The unit for cross-axis sensitivity is often denoted as % with respect to the sensitivity. For tri-axial gyroscopes, cross-axis sensitivity is specified for S_{XZ}, S_{XY}, S_{YX}, S_{YZ}, S_{ZX}, and S_{ZY}. Typical amount of cross-axis sensitivity in contemporary tri-axial gyroscopes in consumer electronics is in 1-2% range.

Both sensitivity and cross-axis sensitivity are supposed to change linearly in response to the applied rotation-rate to the system. When the difference between the output signal and the expected linear value is calculated by least-square method, the calculated value is called as "scale-factor accuracy".

2.4.2. Full-scale Range

Full-scale range (FSR) of a gyroscope determines the maximum input rotation-rate that guarantees linear response in the output signal from a gyroscope system. Therefore, FSR represents the highest rotation-rate that the sensor can operate at and expressed in degree-per-second (dps).

2.4.3. Allan-variance (AVAR) Bias Stability

When gyroscopes are under operation without an applied rotation-rate, the reference level of the output signal is expected not to deviate from its base level. The AVAR bias stability defines the deviation of the reference voltage over time. The typical unit for AVAR bias instability is denoted by deg/hr (dph) or deg/sec (dps), and the measurement is done at a fixed temperature and vibration condition without input rotation rate.

The plotted AVAR bias stability has five regions of slopes which are determined by dominant noise sources that present at the given sampling condition (Figure 15) [19]. Quantization noise represents the random variation in the digitized output signal due to sampling and quantizing a continuous signal with a finite word length conversion, and denoted as “degree”. The next region is angle random walk (ARW) and denotes the total white noise accumulated in the system, and expressed in dps/√Hz. Since ARW is defined by the total noise in the system, it can be directly related to the resolution of the sensor system (2). Bias instability is expressed in degree-per-hour (dph) or dps and denotes long-term stability of the bias level over long period of time. Rate random walk is generated by drift error cause by angular acceleration and denoted by °/√Hz.

$$Total\ Noise\ Level\left(^{\circ}/hr/\sqrt{Hz}\right)=ARW\left(^{\circ}/hr\right)\times 60 \quad \textbf{(2)}$$

The importance of high AVAR bias stability resides in the following reasons: (1) in a gyroscope application for vehicle or pedestrian navigations, the reference output level is set as the true north of the orientation of the system. Considering the relatively slower motion of the object equipped with the gyroscope system compared to the earth's rotation-rate, the AVAR bias stability that is lower than 0.1deg/hour is required for navigation purposes [20, 43, 44], and (2) if the SF of a gyroscope is obtained, the scale-factor accuracy is significantly dependent on the variation in the reference AVAR bias stability level because the change in the reference level generates linearity errors.

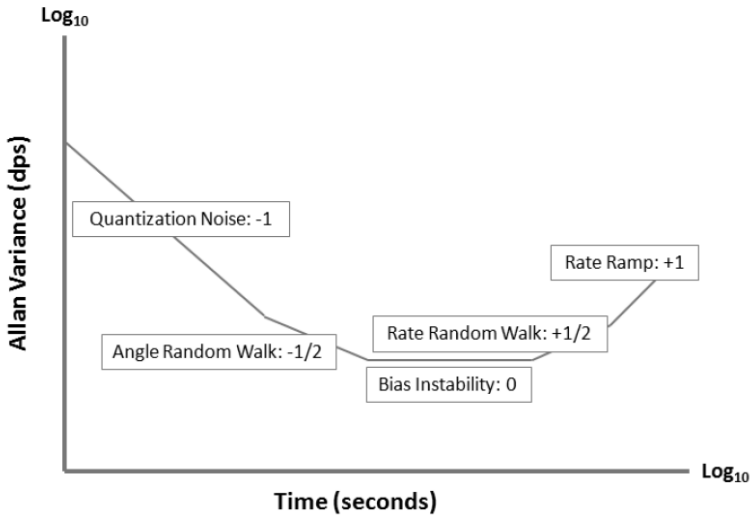

Figure 15: Five-different fittings of AVAR bias stability [54].

2.4.4. Resolution

Resolution is the minimum detectable signal out of the noise level in the system, and expressed by equivalent input rotation rate per square root of the sensor bandwidth (dps/√Hz). Because of inevitable interferences, such as external vibrations, noise from

electronics and the gyroscope's random collision with air molecules in the surrounding medium, a gyroscope system exhibits a certain quantity of noise level, and the system cannot resolve the input rotation rate below the noise level. Individual components that affect the noise performance of the gyroscopes are shown in (3)-(5). The overall noise existing in the output signal is interpreted as "total-noise-equivalent rotation-rate (TNEΩ)" as shown in (3), and the TNEΩ consists of two uncorrelated noise sources in general: mechanical-noise-equivalent rotation-rate (MNEΩ) as shown in (4), and electrical-noise-equivalent rotation-rate (ENEΩ) as shown in (5).

$$TNE\Omega = \sqrt{MNE\Omega^2 + ENE\Omega^2}. \quad \textbf{(3)}$$

$$MNE\,\Omega \propto \frac{1}{q_{drive}} \sqrt{\frac{4 \cdot k_B \cdot T}{\omega_0 \cdot M \cdot Q_{Mode-matched}}}. \quad \textbf{(4)}$$

$$ENE\Omega \propto \frac{d_0}{V_P \cdot C_0 \cdot Q_{Mode-matched} \cdot q_{drive}} \times i_{noise}. \quad \textbf{(5)}$$

where q_{drive}, ω_0, M, $Q_{Mode\text{-}matched}$, d_0, V_P, C_0, and i_{noise} are driving amplitude, mode-matched resonance frequency, effective mass, mode-matched Q-factor, rest capacitive gap size, DC polarization voltage, rest sensing capacitance, and input-referred noise in the interface circuit, respectively.

As mentioned earlier, the ARW denotes TNEΩ in the gyroscope system. The trend of overall noise performance of the MEMS gyroscopes is plotted in Figure 16. For bulk micromachined gyroscopes, the trend reveals 10 times improvement every two years [2].

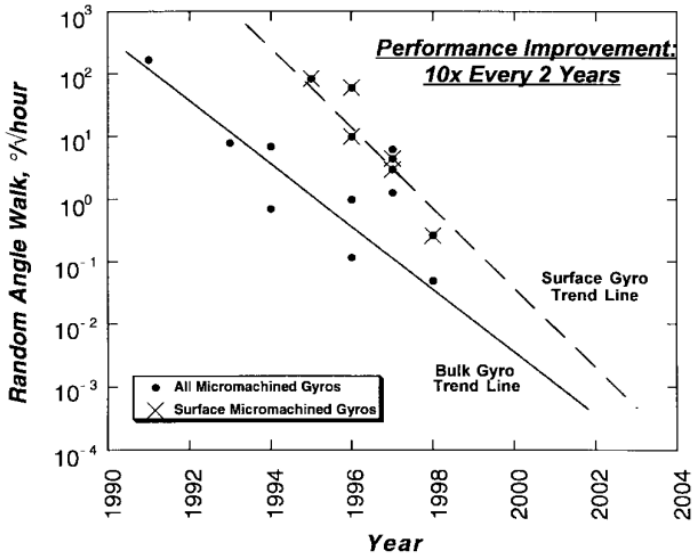

Figure 16: Trend of ARW of MEMS gyroscopes.

2.4.5. Bandwidth

As MEMS gyroscopes operate at their resonant modes, a finite bandwidth in the frequency response exists because of mechanical Q-factors of the device. Since the bandwidth is a channel in the frequency response that transfers vibrating energy from a drive mode to a sense mode in the mode-matched gyroscopes, the amount of bandwidth represents how fast a gyroscope can respond to the applied rotation-rate (6). Typically, 3dB bandwidth is in use to characterize the bandwidth of MEMS gyroscopes.

$$\tau = \frac{1}{BW} = \frac{Q}{f}. \qquad \textbf{(6)}$$

2.4.6. Shock Tolerance

Shock tolerance is the maximum quantity of an impact or change in the acceleration that guarantees the device's operation without failure. Most of state-of-the-

art gyroscopes are designed to survive after shock over 10^3g in 1mili-second, and the shock tolerance represents the robustness of the gyroscope system.

2.5. MEMS Gyroscopes in the Commercial Market

The successful commercialization of MEMS gyroscopes was triggered by expanding market demands in automotive applications for anti-skid stabilization and roll-over detection of a vehicle. Because of the expanding market in consumer electronics, various types of gyroscopes with multi-axis sensing capability have been developed.

The first commercialized yaw MEMS gyroscope was introduced in 2002 by ADI [55, 56]. The surface micromachined gyroscope offered noise level of 0.1dps/√Hz and full scale range of 300dps with fully-integrated interface circuitry. BAE Systems and Sumitoro Precision Products are producing ring-type gyroscope with a noise level of 0.1dps/√Hz in 20 Hz-bandwidth packaged in 10 x 10 mm^2 size. The first pitch-and-roll gyroscope was developed in 2007 by InvenSense [57]. It employed two resonant masses sustained by flexures oscillated to out-of-plane direction with 90 deg angular spatial offset. The dual proof-mass system exhibited high rejection in cross-axis sensitivity of the system with the identical performance to x- and y-axis input rotation-rates. Recently, the rapid dissemination of mobile gadgets such as smart phones and digital cameras accelerated the development of tri-axial MEMS gyroscopes. The state-of-the-art commercial MEMS gyroscopes are listed in Table 2 with a brief summary of production year, noise density, scale factor, FSR, power consumption, and package size.

Table 2: Summary on commercial tri-axial gyroscopes.

Manufact.	STM	InvenSense	Bosch	Murata	MAXIM	Epson	ADI
Model	L3GD20H	MPU 6050	BMG160	CMR3000	21000	AP-6110LR	ADIS16488
Production Year	2013	2012	2012	2011	2013	2011	2012
Noise density (dps/√Hz)	0.011	0.05	0.014	0.2	0.009	0.004	0.0066
Sensitivity (LSB/dps)	14.3 – 114	16.4 – 131	16.4 – 262.4	1.33	15-960 digit/dps	3.0 mV/dps	32.7e5
FSR (dps)	250 - 2000	250 - 2000	125 - 2000	2000	31.25 – 2000	300	450
Current Consumption (mA)	5	3.9	5	5	5.4	6.8	254
Packaging Dimension (mm^3)	3x3x1	4x4x0.9	3x3x0.95	4.1x3.1x0.83	3x3x0.91	10x8x3.8	47x44x14

CHAPTER 3

HIGH-FREQUENCY YAW GYROSCOPE

3.1. Introduction

Low-frequency flexural-mode MEMS gyroscopes have been widely investigated over the past two decades. The low frequency gyroscopes rely on increases in the mass and vibration amplitude of the sensing element to reduce the noise level and improve Allan-variance (AVAR) bias stability, which can be attained by sacrificing the unit die size and operating the device with high voltages [14, 19, 20, 42]. However, design and operation of the MEMS gyroscopes at high frequency regimes can significantly reduce the Brownian noise without increasing the size of device and operating voltages. In addition, large bandwidth over 100Hz is realized with high Q-factors due to the high operating frequencies.

High-frequency, high-Q, and bulk-acoustic-wave (BAW) disk gyroscope is shown in Figure 17. Owing to the in-plane modes of operation and vibration sensing mechanism, the disk gyroscope can sense the rotation rate applied to the perpendicular direction of the disk plane with negligible cross-axis sensitivity [1, 6, 9]. By mode-matching drive and sense resonant modes at an identical frequency, the output signal at sense channel is amplified by Q-factor in the mechanical domain (Figure 18). Since the Q-factors of high-frequency disk gyroscope typically exist in 1,000 – 100,000 range, the device retains drastically higher sensitivity than mode-split device which has Q-amplification of "1". In addition, the high-Q and high-frequency operation retains large mechanical bandwidth that allows fast response without settling time with a given rotation-rate.

The excitation of solid-state bulk acoustic disk resonator should involve large electrostatic force to maintain the resonance through capacitive coupling. The large electrostatic force is obtained by sub-micron capacitive gaps shaped through high-aspect-ratio combined polysilicon and silicon (HARPSS^{TM}) process. A 600µm-diameter disk fabricated in a 40µm-thick silicon-on-insulator (SOI) substrate with 200nm capacitive gap is shown in Figure 17 (right) as an example. The capping substrate is grinded down to show the resonating disk structure and vertical feedthroughs inside the packaged die.

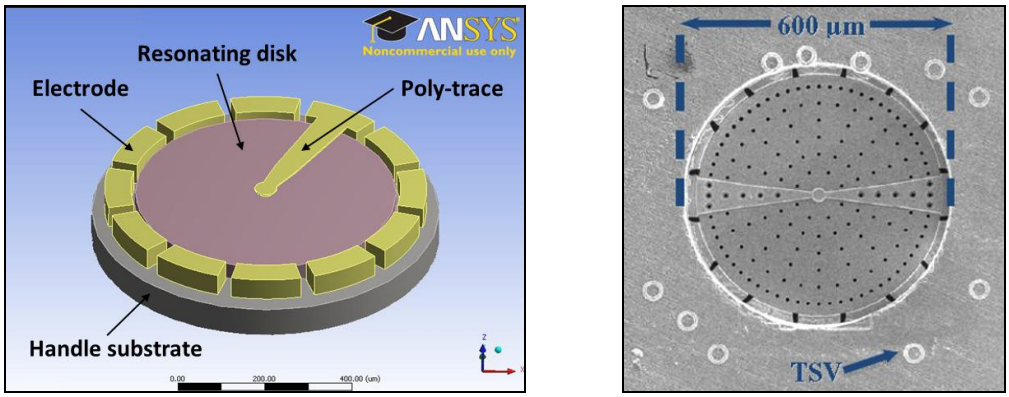

Figure 17: Schematic view of a BAW gyroscope (left) and a SEM view of a wafer-level-packaged BAW gyroscope fabricated using a HARPSS^{TM} process and through-silicon-via (TSV) technologies (presented with courtesy of Qualtré, Inc.) (right).

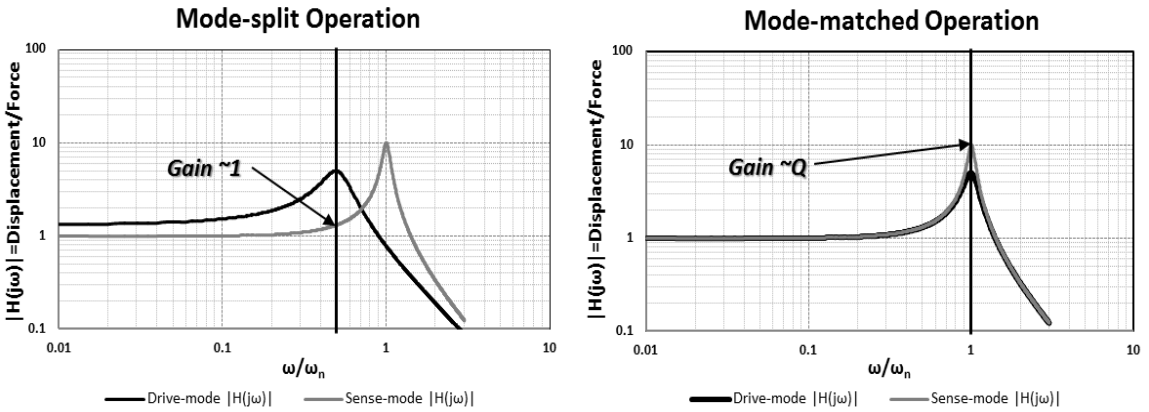

Figure 18: Transfer function of second-order system. Mode-matching of the drive- and sense-modes shows Q-times signal amplification in mechanical domain.

3.2. Design of High-frequency Yaw Gyroscopes

Resonant gyroscopes employ two resonance modes which can be decomposed into two governing second order equations as shown below [58]:

$$M_1 \cdot \frac{d^2}{dt^2} q_1 + D_1 \cdot \frac{d}{dt} q_1 + K_1 \cdot q_1 - M_1 \cdot \Omega^2 \cdot q_1 - q_2 \cdot \lambda \cdot \frac{d}{dt}\Omega - 2M_2 \cdot \lambda \cdot \Omega \cdot \frac{d}{dt} q_2 = F_1. \quad \textbf{(7)}$$

$$M_2 \cdot \frac{d^2}{dt^2} q_2 + D_2 \cdot \frac{d}{dt} q_2 + K_2 \cdot q_2 - M_2 \cdot \Omega^2 \cdot q_2 - q_1 \cdot \lambda \cdot \frac{d}{dt}\Omega - 2M_1 \cdot \lambda \cdot \Omega \cdot \frac{d}{dt} q_1 = F_2. \quad \textbf{(8)}$$

$M_{1,2}$, $D_{1,2}$, $K_{1,2}$, $q_{1,2}$, Ω, λ, and $F_{1,2}$ are effective mass, damping factor, effective spring constant, vibrating amplitude, applied input rotation rate, Coriolis coupling coefficient, and excitation force to each mode.

$M_{1,2} \cdot \Omega^2 \cdot q_{1,2}$ denotes angular acceleration induced force which is mechanically rejected because of the large stiffness of the structure operating in high frequency regime. Since the operating frequency of the gyroscope is several orders higher than expected angular accelerations, $q_{1,2} \cdot \lambda \cdot \frac{d}{dt}\Omega$, can be ignored as well. Considering deformation of sense-mode is relatively smaller compared to drive mode, $-2M_2 \cdot \lambda \cdot \Omega \cdot \frac{d}{dt} q_2$ is also neglected. Since excitation force is applied only to F_1, the force applied to second mode (F_2) does not exist in the system. In addition, since effective mass, loss mechanism, and spring constant in the degenerative modes are identical, i.e. $M_1 = M_2$, $D_1 = D_2$, and $K_1 = K_2$, (7) and (8) are simplified to:

$$M \cdot \frac{d^2}{dt^2} q_1 + D \cdot \frac{d}{dt} q_1 + K \cdot q_1 = F_1. \quad \textbf{(9)}$$

$$M \cdot \frac{d^2}{dt^2} q_2 + D \cdot \frac{d}{dt} q_2 + K \cdot q_2 = 2 \cdot M \cdot \lambda \cdot \Omega \cdot \frac{d}{dt} q_1. \quad \textbf{(10)}$$

Since the scope of yaw gyroscope in this thesis focuses on the in-plane device fabricated on a (100) substrates, N=3 in-plane modes are discussed in this dissertation for small frequency split and high performances.

The ANSYS harmonics simulation results that illustrate the operating frequency and radial deformation are shown in Figure 19. Because of the anisotropic elasticity of (100) silicon, the radial deformation from drive- and sense-modes do not follow exact cos(3θ) and sin(3θ) function. At the anti-nodes of each resonance mode, the radial deformation has 20% variation in each mode.

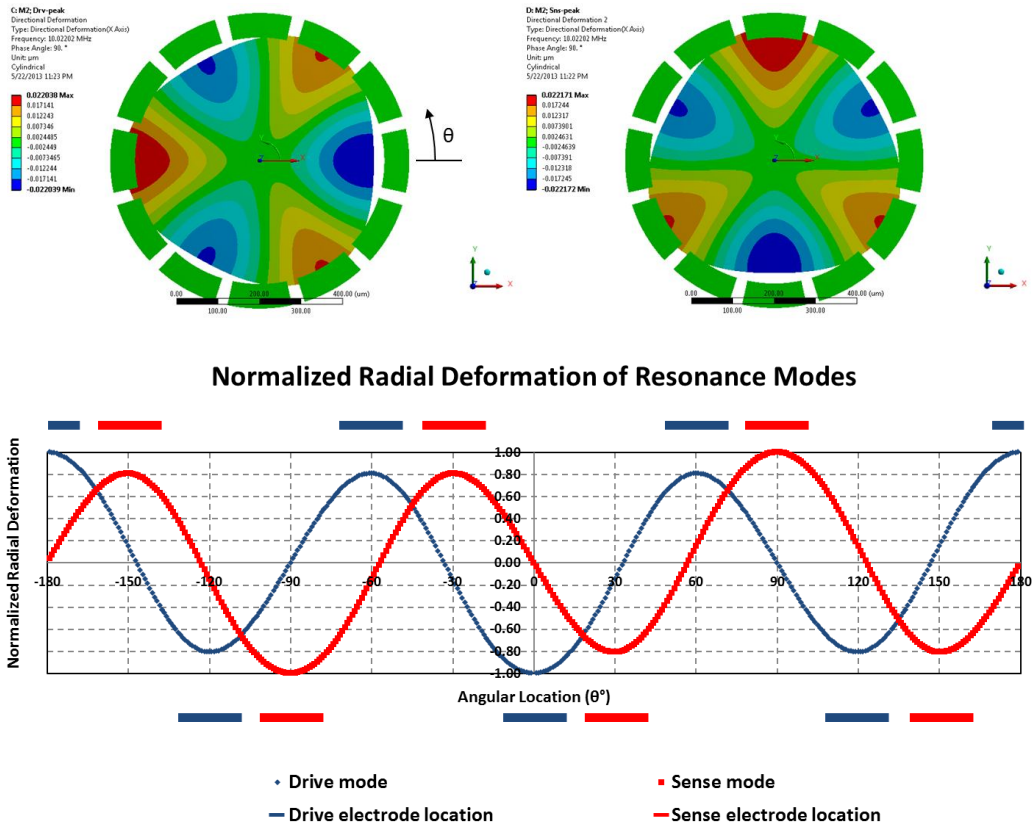

Figure 19: Resonant mode shapes (top) and radial deformation (bottom) of N=3 yaw gyroscope.

However, because of the relatively smaller angle compared to the whole circumferential angle of the disk, the drive- and sense-modes at electrodes location can be approximated as cos(3θ) and sin(3θ) wave as shown in Figure 20.

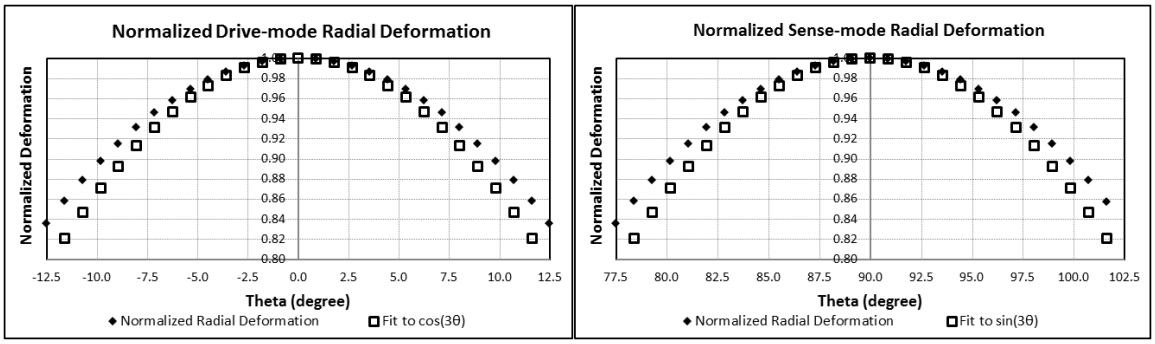

Figure 20: Radial deformations at drive electrode (left) and sense electrode (right) are presented. ANSYS and sinusoidal fit demonstrate discrepancy due to the anisotropic behavior of substrate.

3.2.1. Capacitance Change at Drive- and Sense-modes

Because of the axis-symmetric circular shape of the disk, the radial deformation of the drive- and sense-modes follows elliptical deformation that is obtained by fitting the mode-shapes by sinusoidal function with three periods in the circumference. Once the drive mode is cos(3θ) function, sense-mode is modeled by sin(3θ) which has 90˚ spatial offset against the drive-mode.

Capacitance change at the resonance is obtained as follows:

$$C_D = \int \frac{\varepsilon_0}{d_{01} + \Delta d} \cdot dA = \int_{-\frac{\Delta\theta_n}{2}}^{+\frac{\Delta\theta_n}{2}} \frac{\varepsilon_0 \cdot h}{d_{01} + \Delta d} \cdot R \cdot d\theta = \frac{\varepsilon_0 \cdot h \cdot R}{d_{01}} \cdot \int_{-\frac{\Delta\theta_n}{2}}^{+\frac{\Delta\theta_n}{2}} \frac{1}{1 + \frac{\Delta d}{d_0}} d\theta. \quad \textbf{(11)}$$

where ε_0, d_{01} and Δd are permittivity of free space, rest side air gap size, and change in the radial deformation of the resonant mass due to vibration, respectively. h is the height

of mass, R is the radius of the mass, and $\Delta\theta_n$ is spanned angle of the interacting side electrode. Considering vibration amplitude is set as 10% of the nominal capacitive gap size ($\Delta d/d_0 << 1$) and N=3 in-plane modes have radial deformation of $\Delta d = q \cdot cos(3 \cdot \theta)$, (11) can be expanded using Taylor series.

$$C = \frac{\varepsilon_0 \cdot h \cdot R}{d_{01}} \int_{-\frac{\Delta\theta_n}{2}}^{+\frac{\Delta\theta_n}{2}} \left[1 - \frac{\Delta d}{d_{01}} + \left(\frac{\Delta d}{d_{01}} \right)^2 - \cdots \right] d\theta = \frac{\varepsilon_0 \cdot h \cdot R}{d_{01}} \left\{ \int_{-\frac{\Delta\theta_n}{2}}^{+\frac{\Delta\theta_n}{2}} d\theta - \int_{-\frac{\Delta\theta_n}{2}}^{+\frac{\Delta\theta_n}{2}} \frac{q \cdot \cos(3 \cdot \theta)}{d_{01}} d\theta + \int_{-\frac{\Delta\theta_n}{2}}^{+\frac{\Delta\theta_n}{2}} \left[\frac{q \cdot \cos(3 \cdot \theta)}{d_{01}} \right]^2 d\theta - \cdots \right\}$$

$$\cong \left(\frac{\varepsilon_0 \cdot h \cdot R}{d_{01}} \Delta\theta_n \right) - \frac{\varepsilon_0 \cdot h \cdot R}{d_{01}} \cdot \left[\frac{2 \cdot q \cdot \sin\left(\frac{3 \cdot \Delta\theta_n}{2} \right)}{3 \cdot d_{01}} - \left(\frac{q}{d_{01}} \right)^2 \cdot \left(\frac{\Delta\theta_n}{2} + \frac{\sin(3 \cdot \Delta\theta_n)}{6} \right) \right] \quad \textbf{(12)}$$

$$= C_0 + \Delta C.$$

From (12), the initial capacitance at the rest state of drive-mode and the capacitance change by resonance motion of the N=3 in-plane mode are approximated by:

$$C_0 \cong \left(\frac{\varepsilon_0 \cdot h \cdot R}{d_{01}} \cdot \Delta\theta_n \right). \quad \textbf{(13)}$$

$$\Delta C \cong -\frac{\varepsilon_0 \cdot h \cdot R}{d_{01}} \cdot \left[\frac{2 \cdot q \cdot sin\left(\frac{3 \cdot \Delta\theta_n}{2} \right)}{3 \cdot d_{01}} - \left(\frac{q}{d_{01}} \right)^2 \cdot \left(\frac{\Delta\theta_n}{2} + \frac{sin(3 \cdot \Delta\theta_n)}{6} \right) \right]. \quad \textbf{(14)}$$

3.2.2. Effective Mass Estimation

The radial displacement at the location of (r, θ) in the resonating body is defined by well-known equation [59]:

$$M_{eff} = \int m(\theta) \cdot d\theta = \int \rho \cdot h \cdot R^2 \cdot \sum \frac{1}{U_R{}^2} \cdot d\theta. \quad \textbf{(15)}$$

where ρ is density of the resonating material, $\sum \frac{1}{U_R^2}$ is effective mass coefficient. By FEM analysis, $\sum \frac{1}{U_R^2}$ is approximated to be 2.173e3 (dimensionless).

3.2.3. Drive-mode Characteristic Analysis

3.2.3.1. Applied AC Voltage vs. Excitation Force

Figure 21 shows the schematic view of drive-mode and excitation scheme. The disk has a dedicated drive-in and drive-out electrodes to actuate the resonator using electrostatic force and detect the output current. The output current detected from drive-out electrode is fed back to drive-in electrode after gain state in the interface ASIC for the closed-loop drive-mode operation [60-62]. The first step to analyze the disk starts from modeling the drive-mode of the disk gyroscope.

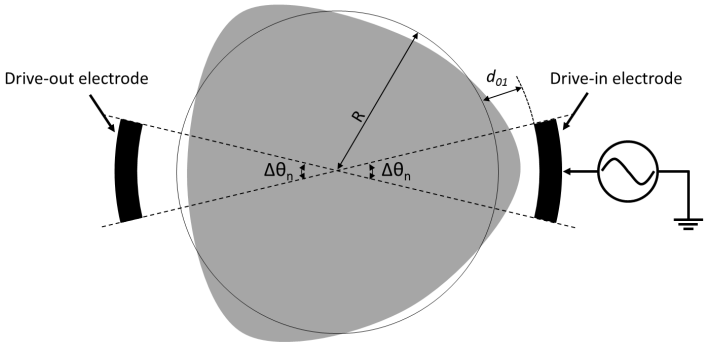

Figure 21: Schematic view of N=3 in-plane drive-mode in disk gyroscope.

From (9), the drive-mode at its resonance is simplified as:

$$D \cdot \frac{d}{dt} q_1 = F_1 \qquad \textbf{(16)}$$

In capacitive actuation, actuation force (F_1) is explained by well-known equations:

$$F_D(r) = \frac{d}{dr}\left[\frac{1}{2}C \cdot V^2\right] = \frac{1}{2}\cdot\left[\left(V_P - V_{Bias}\right) + v_{ac}\right]^2 \cdot \frac{d}{dr}C_D. \tag{17}$$

where V_P is DC polarization voltage applied to the resonant mass, V_{Bias} represents DC voltage that biases drive-in electrode, v_{ac} is the AC excitation signal, and C_D is capacitance between the disk and drive-in electrode. From (12) and (16), (17) becomes

$$\begin{aligned} F_D(r) &= \frac{1}{2}\cdot\left[\left(V_P - V_{Bias}\right) + v_{ac}(t)\right]^2 \cdot \frac{d}{dr}\left[\left(\frac{\varepsilon_0 \cdot h \cdot R}{d_{01}}\Delta\theta_n\right) - \frac{\varepsilon_0 \cdot h \cdot R}{d_{01}}\cdot\left[\frac{2\cdot q \cdot sin\left(\frac{3\cdot\Delta\theta_n}{2}\right)}{3\cdot d_{01}} - \left(\frac{q}{d_{01}}\right)^2 \cdot \left(\frac{\Delta\theta_n}{2} + \frac{sin\left(3\cdot\Delta\theta_n\right)}{6}\right)\right]\right] \\ &\cong \frac{1}{2}\cdot\left(V_P - V_{Bias}\right)^2 \cdot \left(-\frac{\varepsilon_0 \cdot h \cdot R}{{d_{01}}^2}\cdot\frac{2\cdot sin\left(\frac{3\cdot\Delta\theta_n}{2}\right)}{3}\right) + \frac{1}{2}\cdot v_{ac}(t)^2 \cdot \left(-\frac{\varepsilon_0 \cdot h \cdot R}{{d_{01}}^2}\cdot\frac{2\cdot sin\left(\frac{3\cdot\Delta\theta_n}{2}\right)}{3}\right) \\ &\quad - \left(V_P - V_{Bias}\right)\cdot v_{ac}(t)\cdot\left(-\frac{\varepsilon_0 \cdot h \cdot R}{{d_{01}}^2}\cdot\frac{2\cdot sin\left(\frac{3\cdot\Delta\theta_n}{2}\right)}{3}\right). \end{aligned} \tag{18}$$

Ignoring DC-term and small signals, electrostatic force applied from the drive-in electrode is calculated by:

$$F_D(r) = \left(V_P - V_{Bias}\right)\cdot v_{ac}(t)\cdot\left[\frac{2}{3}\cdot\frac{\varepsilon_0 \cdot h \cdot R}{{d_{01}}^2}\cdot\sin\left(\frac{3\cdot\Delta\theta_n}{2}\right)\right]. \tag{19}$$

3.2.3.2. Applied AC Voltage vs. Vibration Amplitude of Drive-mode

Since the radial deformation of the drive mode follows time-varying sinusoidal form, mechanical deformation of drive-mode is assumed to be $q_D = q_1 \cdot \sin(\omega_0 \cdot t)$, the relation between excitation voltage and driving amplitude is obtained as follows:

$$v_{ac}(t) = \left[\frac{{\omega_0}^2 \cdot M_D}{Q_D \cdot (V_P - V_{Bias})}\right] \cdot \left[\frac{3}{2} \cdot \frac{{d_{01}}^2}{\varepsilon_0 \cdot h \cdot R \cdot \sin\left(\frac{3 \cdot \Delta\theta_n}{2}\right)}\right] \cdot q_1 \cdot \cos(\omega_0 \cdot t) \quad \textbf{(20)}$$

From on (20), the AC voltage to excite the disk with vibration amplitude of q_1 is identified. The force-to-displacement relation with 90˚ phase difference is observed.

3.2.3.3. Output Current Induced by Drive-mode Resonance

The radial deformation of N=2 in-plane drive-mode has the same radial deformation in the resonant mass at drive-in/out electrodes. The output current through capacitive air gap is expressed in a general equation.

$$i_{output}(t) = (V_P - V_{Bias}) \cdot \frac{dC_D}{dt} = (V_P - V_{Bias}) \cdot \frac{dC_D}{dq_D} \cdot \frac{dq_D}{dt} \quad \textbf{(21)}$$

By equating (12) and (21), the output current at drive-out electrode is approximated as follows:

$$i_{output}(t) = (V_P - V_{Bias}) \cdot \left[\frac{2}{3} \cdot \frac{\varepsilon_0 \cdot h \cdot R}{{d_{01}}^2} \cdot \sin\left(\frac{3 \cdot \Delta\theta_n}{2}\right)\right] \cdot [(\omega_0 \cdot q_1) \cdot \cos(\omega_0 \cdot t)] \quad \textbf{(22)}$$

As shown above, the output current is in-phase with excitation voltage while 90˚-off from mechanical resonance of the drive-mode.

3.2.3.4. Motional Impedance of Drive-mode

The mechanical vibration created by AC excitation voltage induces output current at the drive-out electrode. The voltage-to-current ratio describes impedance in the resonating system [59, 63]. The motional impedance (R_M) is calculated by taking ratio between (20) and (22).

$$R_M = \left| \frac{v_{ac,in}(t)}{i_{output}(t)} \right| = \frac{\omega_0 \cdot M_D}{Q_D} \cdot \frac{{d_{01}}^4}{\left[\frac{2}{3} \cdot (V_P - V_{Bias}) \cdot \varepsilon_0 \cdot h \cdot R \cdot \sin\left(\frac{3 \cdot \Delta\theta_n}{2} \right) \right]^2}. \quad \textbf{(23)}$$

3.2.4. Sense-mode Characteristic

3.2.4.1. General Equation in Motion of Sense-mode

The sense-mode equation in the in-plane gyroscope is approximated in (10). It can be re-written in time domain as follows:

$$q_2(j\omega_n) = \frac{2 \cdot \lambda \cdot \Omega_Z \cdot \omega_0 \cdot q_1 \cdot \cos(\omega_0 \cdot t - \phi)}{\left({\omega_n}^2 - {\omega_0}^2 \right) + j \cdot \left(\frac{\omega_n \cdot \omega_0}{Q} \right)}. \quad \textbf{(24)}$$

where ω_n denotes sense-mode frequency.

The amplitude and phase response at Coriolis-force induced sense-mode vibration amplitude can be decomposed as follows:

$$\left|q_2(j\omega_n)\right| = \frac{2\cdot\lambda\cdot\Omega_Z\cdot\omega_0\cdot q_1}{\sqrt{\left(\omega_n{}^2-\omega_0{}^2\right)^2+\left(\frac{\omega_n\cdot\omega_0}{Q_S}\right)^2}}. \tag{25}$$

$$\angle q_2(j\omega_n) = \tan^{-1}\left[\frac{\left(\frac{\omega_n\cdot\omega_0}{Q_S}\right)}{\omega_n{}^2-\omega_0{}^2}\right]. \tag{26}$$

As a result, (24) can be re-written from (25) and (26).

$$q_2 = \frac{2\cdot\lambda\cdot\Omega_Z\cdot\omega_0\cdot q_1}{\sqrt{\left(\omega_n{}^2-\omega_0{}^2\right)^2+\left(\frac{\omega_n\cdot\omega_0}{Q_S}\right)^2}}\cdot\cos\left(\omega_n-\tan^{-1}\left[\frac{\left(\frac{\omega_n\cdot\omega_0}{Q_S}\right)}{\omega_n{}^2-\omega_0{}^2}\right]\right). \tag{27}$$

3.2.4.2. Output Current at Sense-mode with Rotation Rate

Once the mechanical deformation of sense-mode with applied-rotation rate is obtained, the output current induced by rotation-rate can be calculated. Similarly to output current at drive-out electrode, Coriolis-force induced sense response can be calculated as follows:

$$\begin{aligned} i_{output}(t) &= \left(V_P - V_{Bias}\right)\cdot\frac{dC_S}{dt} = \left(V_P - V_{Bias}\right)\cdot\frac{dC_S}{dq_1}\cdot\frac{dq_1}{dt} \\ &= \left(V_P - V_{Bias}\right)\cdot\frac{\varepsilon_0\cdot h\cdot R}{d_{01}{}^2}\cdot\left[\frac{2}{3}\cdot\sin\left(\frac{3\cdot\Delta\theta_n}{2}\right)\right]\cdot\frac{2\cdot\lambda\cdot\Omega_Z\cdot\omega_0{}^2}{\sqrt{\left(\omega_n{}^2-\omega_0{}^2\right)^2+\left(\frac{\omega_n\cdot\omega_0}{Q_S}\right)^2}}\cdot q_1\cdot\cos(\omega_0\cdot t) \end{aligned} \tag{28}$$

3.2.4.3. Full-scale Range

Capacitive excitation and detection scheme in a resonant device demonstrate linear response between input to output signals until the vibration amplitude reaches 10% of its nominal gap size. Therefore, the resonant gyroscopes exhibit the linear Coriolis-force induced output signal until the sense-mode amplitude becomes 10% of the nominal capacitive gap size. By substituting $|q_2(j\omega)|$ to $0.1\times d_0$ in (25), the full-scale range is obtained.

$$\Omega_Z\big|_{Max} = \frac{d_{02}}{20} \cdot \frac{\sqrt{\left(\omega_n{}^2 - \omega_0{}^2\right)^2 + \left(\frac{\omega_n \cdot \omega_0}{Q_S}\right)^2}}{\lambda \cdot \omega_0 \cdot q_1}. \tag{29}$$

3.2.4.4. Brownian Noise Analysis

The Brownian motion of resonant gyroscope caused by random collision with surrounding air molecules draws the fundamental limit in the noise performance of the gyroscope system [64]. By equating the Coriolis-force induced deformation with Brownian amplitude described in (30), the mechanical noise equivalent rotation-rate (MNEΩ) is calculated (31).

$$\left|q_{2,Brownian}\right| = \sqrt{\frac{4 \cdot k_B \cdot T \cdot Q_S}{M_S \cdot \omega_n{}^3}}. \tag{30}$$

$$MNE\Omega = \Omega_Z\big|_{min} = \frac{1}{2 \cdot \lambda \cdot q_1} \cdot \sqrt{\frac{4 \cdot k_B \cdot T \cdot Q_S}{M_S \cdot \omega_n}} \cdot \left(\frac{\omega_n}{\omega_0}\right) \cdot \sqrt{\left(1 - \frac{\omega_0{}^2}{\omega_n{}^2}\right)^2 + \left(\frac{\omega_0}{Q_S \cdot \omega_n}\right)^2}. \tag{31}$$

3.2.4.5. Dynamic Range

Dynamic range (DR) of resonant gyroscope is obtained by taking the ratio between FSR to MNEΩ [60].

$$DR = 20 \cdot log\left(\frac{\Omega_Z|_{Max}}{\Omega_Z|_{min}}\right) = 20 \cdot log\left(\frac{d_{02}}{10}\sqrt{\frac{M_S \cdot \omega_n}{4 \cdot k_B \cdot T \cdot Q_S}}\right). \quad \textbf{(32)}$$

Because FSR ($\Omega_Z|_{Max}$) and MNEΩ ($\Omega_Z|_{min}$) are affected by the same amount with respect to Δf (=ω_n-ω_0), DR becomes irrelevant to Δf.

3.2.4.6. Drive- and Sense-modes Tuning Behavior

To ensure the mode-matched operation under the process deviations and non-idealities in the substrate material, the resonant modes must retain sufficient electrostatic frequency tunability to compensate frequency split (Δf). A dedicated set of electrodes are assigned to tune the N=3 in-plane modes as shown in Figure 22. The spanned angle (Δθ) of the tuning electrodes is defined the same as drive-in/out and sense-out electrodes for the symmetry of the device.

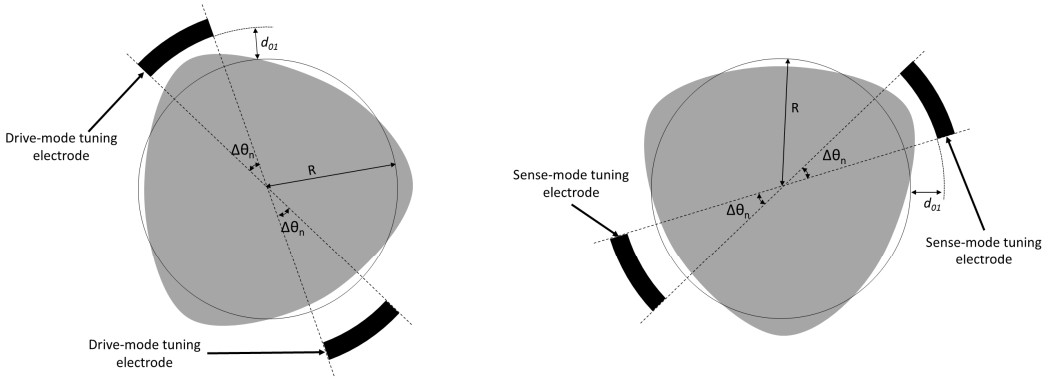

Figure 22: Tuning electrodes of N=3 in-plane drive- and sense-modes.

The resonant frequency is defined by general equation as follows [8, 9, 12, 59]:

$$\omega_{Tuned} = \sqrt{\frac{K_{Total}}{M_{eff}}} = \sqrt{\frac{K_{Mechanical} + K_{Electrical}}{M_{eff}}}. \quad \textbf{(33)}$$

where K_{Total}, $K_{Mechanical}$, and $K_{Electrical}$ are total spring constant, mechanical spring constant, and electrical spring constant, respectively. $K_{Mechanical}$ is fixed value at the resonance mode if the resonant frequency and effective mass are defined. However, $K_{Electrical}$ is determined by voltage applied through the capacitive gap and the capacitance. $K_{Mechanical}$ and $K_{Electrical}$ can be re-written as follows:

$$K_{Mechanical} = \omega_0^{\,2} \cdot M_D. \quad \textbf{(34)}$$

$$K_{Electrical} = -\frac{d}{dr} F_D$$

$$= -N_T \cdot \left(V_P - V_{Tuning}\right)^2 \cdot \left(\frac{N_T \cdot \varepsilon_0 \cdot h \cdot R}{d_{01}^{\,3}}\right) \cdot \left(\frac{\Delta\theta_n}{2} + \frac{\sin\left(\frac{3 \cdot \Delta\theta_n}{2}\right)}{12}\right). \quad \textbf{(35)}$$

where N_T is the number of tuning electrodes to the resonance mode for electrostatic tuning. As shown in (35), $K_{Electrical}$ is negative value regardless of the polarity of applied DC tuning voltage. Therefore, we can only down-shift the frequency from the natural mechanical resonance frequency of the mode. The tuned resonance frequency with applied DC tuning voltage is expressed by:

$$\omega_{Tuned}{}^2 = \frac{K_{Mechanical} + K_{Electrical}}{M_D} = \omega_0{}^2 + \frac{K_{Electrical}}{M_D}$$
$$= \omega_0{}^2 - \frac{1}{M_D} \cdot \left(V_P - V_{Tuning}\right)^2 \cdot \frac{N_T \cdot \varepsilon_0 \cdot h \cdot R}{d_{01}{}^3} \cdot \left(\frac{\Delta\theta_n}{2} + \frac{\sin\left(\frac{3 \cdot \Delta\theta_n}{2}\right)}{12} \right). \quad \textbf{(36)}$$

Therefore, electrostatically tuned resonance frequency becomes

$$f_{Tuned} = f_0 \cdot \sqrt{1 - \frac{1}{K_{Mechanical}} \cdot \left(V_P - V_{Tuning}\right)^2 \cdot \frac{N_T \cdot \varepsilon_0 \cdot h \cdot R}{d_{01}{}^3} \cdot \left(\frac{\Delta\theta_n}{2} + \frac{\sin\left(\frac{3 \cdot \Delta\theta_n}{2}\right)}{12} \right)}. \quad \textbf{(37)}$$

3.3. Spoke Gyroscope Design

MEMS gyroscopes [1, 2] are increasingly used in applications that require a wide full-scale range and a large bandwidth, such as gaming controllers and smart user interfaces. Their popularity has grown significantly because of the low cost, small size, robustness, and low power consumption, which had been hardly achievable with conventional mechanical and optical gyroscopes. Resonant gyroscopes, which operate at mode-matched conditions [6, 8, 12, 19], use two resonance modes of a structure that are mode-matched at an identical frequency to amplify the Coriolis force-induced vibration by the mechanical Q-factor of the sense mode. However, because of imperfections in the fabrication process, the native drive and sense resonance modes of these devices may exhibit a frequency separation. Therefore, DC potentials are applied in the calibration step to adjust the electrical stiffness of the drive and sense resonance modes to make the pass-bands overlap. In this work, a spoke gyroscope design is introduced to increase the resonator bandwidth such that it is larger than the worst-case frequency separation that is

caused by fabrication errors. A wide band-pass-filter response is hence created for the gyroscope to allow the bandwidth and full-scale range of the sensor to be increased. Similar to the perforated high-frequency BAW disk gyroscopes [6, 9, 60], the spoke gyroscope operates in the MHz range.

The spoke gyroscope operates at 3.12MHz in a near mode-matched condition (without tuning), and the gyroscope has -1dB and -3dB bandwidth of 1.5kHz and 3kHz, respectively, operating in air. The device has a linear full-scale range in excess of 30,000˚/sec with a sensitivity of 15.0μV/˚/sec/electrode using a 10V DC polarization voltage. The wide bandwidth and the large full-scale range of this device are beneficial for applications that require a rapid-motion sensing.

Figure 23 shows a schematic view of the center-supported capacitive silicon spoke gyroscope. Because of the anisotropic nature of (100) single-crystal-silicon (SCS) substrates, the device is designed to operate at its degenerate secondary elliptical modes, in which the drive and sense modes are spatially 30º apart [9]. The spoke gyroscope uses a geometry that replaces a concentric ring section of a disk with a network of spokes and beams. At resonance, the outer region that retains the continuous disk-like shape undergoes a bulk-acoustic mode of vibration while the region with spokes exhibits a flexural mode (Figure 24, left). Energy losses associated with the flexural mode of vibration (e.g. thermoelastic damping) serve to reduce the overall quality (Q) factor of the gyroscope. As a result, the relatively low Q (1,000-2,000) of the spoke gyroscope at the high resonance frequency creates a large bandwidth and a fast response time without needing a vacuum. Additionally, the -3dB bandwidth of the resonance mode is larger than the frequency split caused by fabrication errors between the two degenerate modes.

Inner and outer spokes are arranged every 30˚ and 15˚ to minimize an excessive frequency separation between the drive and sense modes [9]. In addition, 10μm-sized release holes are included to facilitate the structural release process. The release holes are equally-spaced and oriented in the same way as the spokes.

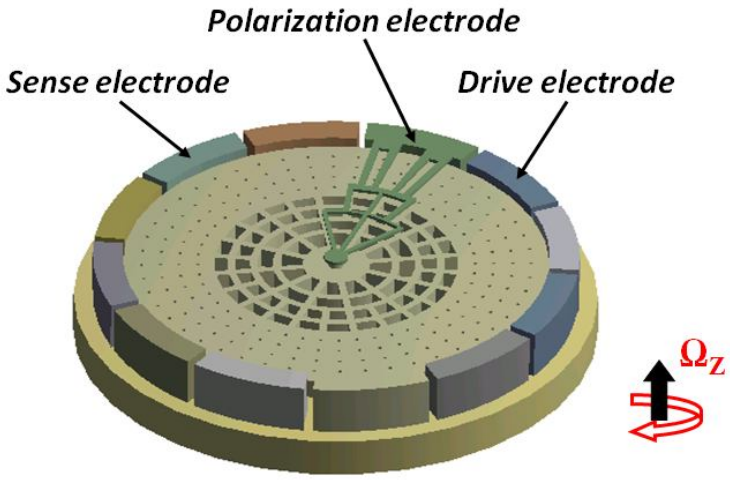

Figure 23: Schematic diagram of a capacitive spoke gyroscope.

ANSYS electromechanical harmonic simulations are executed to approximate the sensitivity and the full-scale range of the gyroscope as shown in Figure 24. First, the worst-case frequency separation of 2kHz is intentionally created between the two secondary elliptical modes by adjusting the electrical stiffness in the simulation environment to separate the drive- and sense-modes. Afterward, the drive mode is excited to the vibration amplitude of 10nm, while a DC polarization voltage of 10V is applied to the resonating body of the gyroscope. A Q-factor of 1,000 is assumed for the drive and sense modes. Simulated rotation-rates are applied, and the Coriolis force-induced output current, which is detected at a single sense electrode, is plotted in Figure 24 (right). The device exhibits a very linear full-scale range in excess of 30,000˚/sec with a sensitivity of

2.73pA/˚/sec/electrode. The overall rate sensitivity of the device can be increased by a factor of six through differential sensing and connecting the in-phase sense electrodes together.

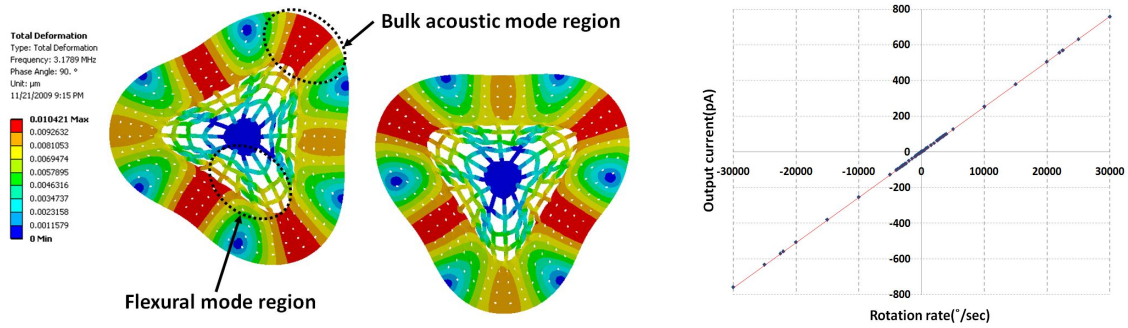

Figure 24: ANSYS harmonic simulations of a spoke gyroscope showing a secondary-elliptical drive mode at 3.1815MHz and a sense mode at 3.1795MHz with ±10nm deformation (left). ANSYS simulation results that show the sensitivity and full-scale range (right).

3.4. Fabrication of High-frequency Yaw Gyroscopes

The capacitive BAW spoke gyroscopes are fabricated on 60µm-thick silicon-on-insulator (SOI) substrates using the HARPSS™ process [5, 6] . The basic outline of the process is shown in Figure 25. The fabrication starts from patterning an oxide mask created by thermal oxidation (Figure 25 (a,b)). Deep trenches are etched through the device layer of the SOI wafer to define the spoke structure and release holes, and a 200nm oxidation is done to create a capacitive gap between the vibrating mass and electrodes (Figure 25 (c,d)). The trenches are refilled with low-pressure chemical-vapor-deposition (LPCVD) polysilicon after the boron doping, and a 200nm-thick sacrificial oxide (SACOX) is patterned from the top surface (Figure 25 (e,f)). The second LPCVD polysilicon is deposited, doped, annealed, and patterned to define the electrode pads. The

final step of the fabrication is a timed release in hydrofluoric acid (HF), leaving a central buried oxide support layer underneath the spoke structure (Figure 25 (g,h)).

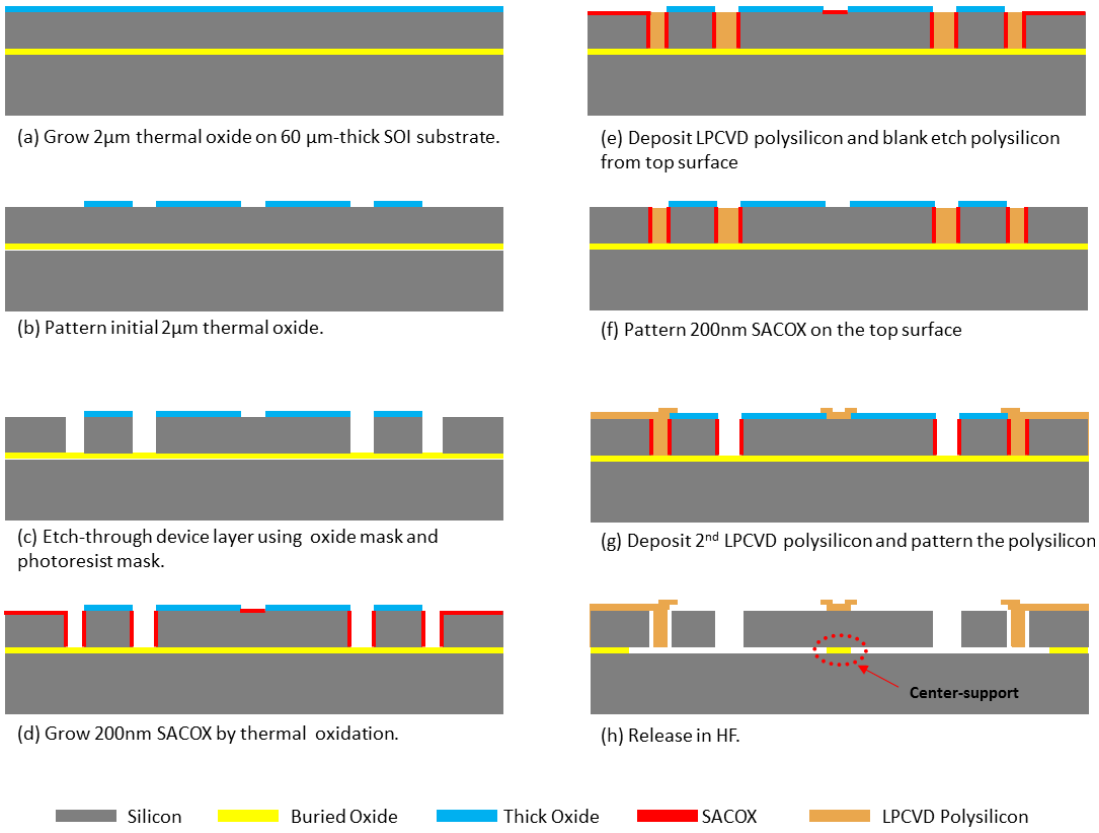

Figure 25: Fabrication process flow of SCS BAW spoke gyroscopes.

SEM images of the fabricated devices are shown in Figure 26. The overall shape of a fabricated spoke gyroscope (Figure 26, left), a zoom-in SEM picture of the central region in the gyroscope with the polysilicon trace (Figure 26, top-right), and a batch-fabricated spoke gyroscope die (Figure 26, bottom-right) are shown.

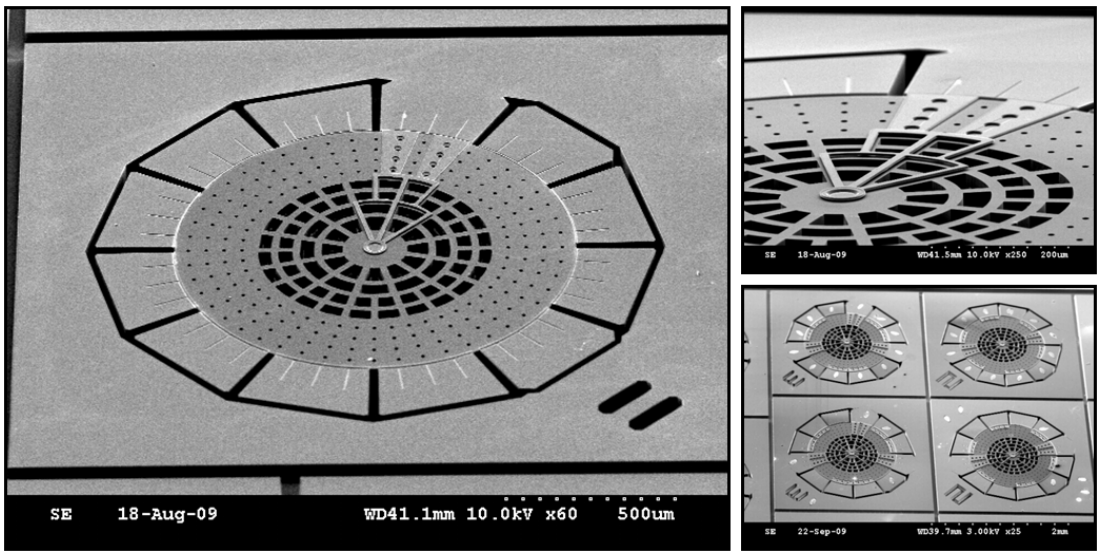

Figure 26: Fabricated spoke gyroscopes.

3.5. Characterization of Yaw Gyroscopes

The overall measurement setup is described in Figure 27. The spoke gyroscope is affixed to a printed circuit board (PCB) and driven in an open-loop condition using an Agilent N4395A network analyzer. The output sense electrode is connected to a TI OPA657, which is a discrete trans-impedance amplifier at the front-end, with a feedback resistance of 33kΩ. Additional voltage amplifiers are added after the trans-impedance stage to provide supplementary gain to compensate for the insertion loss of the device as well as prevent any loading from the measurement equipment that would affect the output sense signal. A circuit diagram is drawn in Figure 27 (left), and Ideal Aerosmith 1291BR rate table used for the rate-applied measurement is shown in Figure 27 (right).

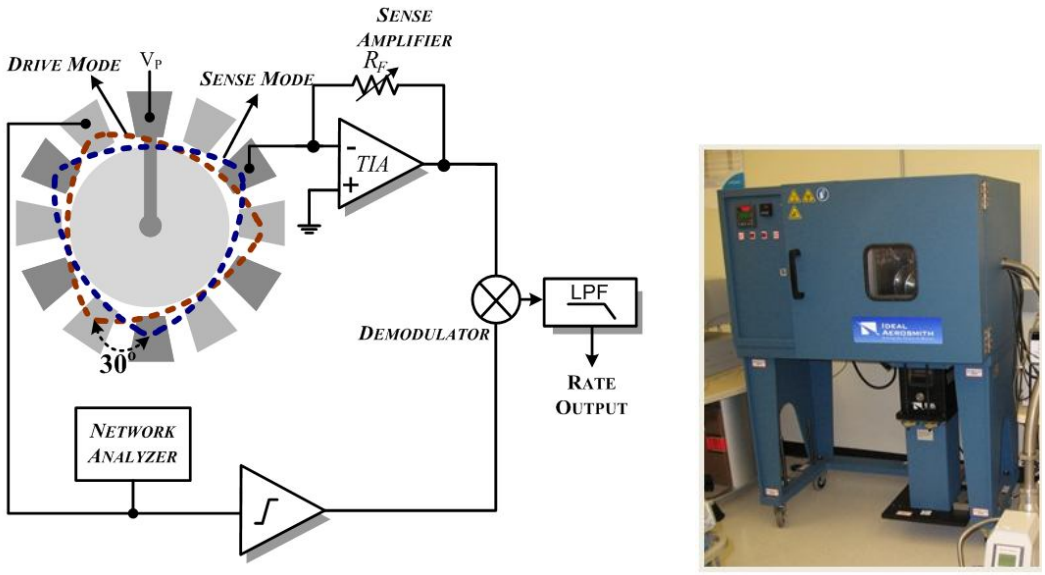

Figure 27: Interface circuit diagram on PCB (left) and rotation table (right).

The frequency responses of several devices are tested in air, and the responses show the expected wide bandpass response of the gyroscopes as shown in Figure 28. The measured frequency response of a prototype device is shown in Figure 28 (left), and the response exhibits a large -3dB bandwidth of 2.87kHz at 3.12MHz in air. All the electrodes around the disk are tied to V_P with the exception of drive and sense electrodes, and no electrostatic tuning is performed on this device. The -1dB bandwidth of the gyroscope is measured on the network analyzer to be over 1.5kHz, and this wide bandwidth suggests the rate sensitivity of the device can remain the same across a large operational bandwidth of at least 1kHz. The zero-rate output (ZRO) or the quadrature signal of the measured device is shown in Figure 28 (middle). Following the ZRO measurement, different rotation signals are applied to the spoke gyroscope using the Ideal Aerosmith rotation table. In the rate-applied measurement, the amplitude-modulated sense current is amplified and demodulated using the input drive signal, and an Analog Devices AD835 four-quadrant mixer is employed to extract the Coriolis signal. The

measured rate sensitivity of the spoke gyroscope is shown in Figure 28 (right). The linear scale-factor of this sensor is measured to be ~15.0μV/˚/sec. Although a large full-scale range of ~30,000˚/sec is simulated, the measurement is capped at 500˚/sec because the rate table is unable to support rotation-rates in excess of this value.

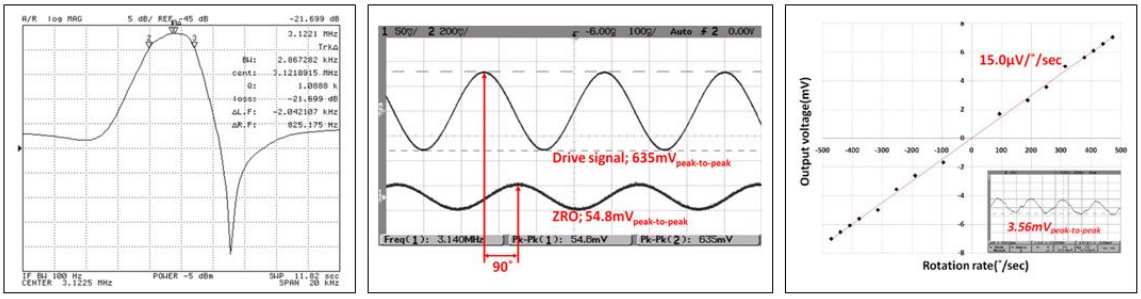

Figure 28: Measured frequency response (left), ZRO (middle), and sensitivity (right) of a spoke gyroscope in air.

Preliminary temperature sensitivity measurements are performed on an unpackaged device over a range of -20˚C to 70˚C as shown in Figure 29. The bandwidth and bandpass response of the gyroscope remain relatively constant over this temperature range, although some distortion can be seen in the pass band at lower temperatures. The gyroscope shows a frequency-response dependency of ~ -27ppm/˚C.

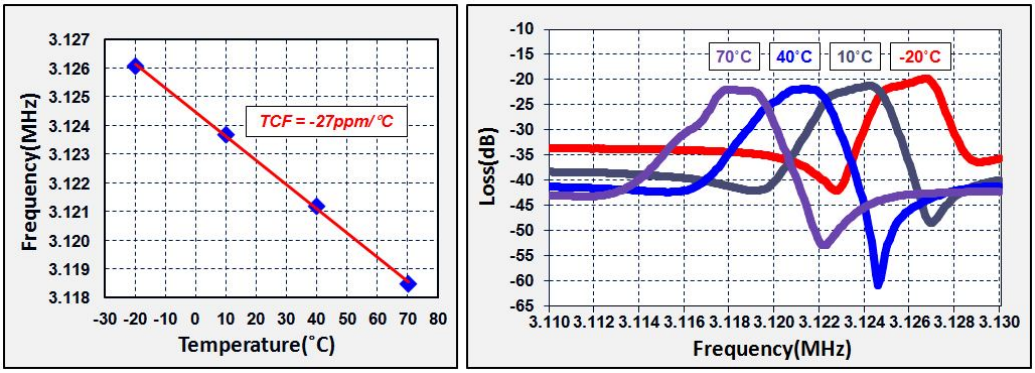

Figure 29: Measured temperature coefficient of frequency in air (left) and frequency response of device at each marker from -20˚C- 70˚C.

The design specifications and measurement results of the spoke gyroscope are summarized in Table 3. Although the Q and rate sensitivity of the measured spoke gyroscope are lower than the perforated-disk gyroscopes [9], the spoke gyroscope offers larger bandwidth and a wider full-scale range than solid-disk BAW gyroscopes while operating in air at a low DC polarization voltage of 10V. Furthermore, electrostatic tuning of the gyroscope is completely eliminated. Although the measured device operates under a mode-coupled condition, simulations show that the sensitivity of the spoke gyroscope remains relatively constant for a peak separation of up to 2kHz. The sensitivity can be improved by reducing the capacitive gap size and increasing the device thickness to augment the capacitive area, as well as increasing the drive amplitude. In addition to these changes, the input-referred noise of the interface electronics can be reduced by interfacing the device with an application-specific integrated circuit (ASIC).

Table 3: Performance summary for the spoke gyroscope.

Device Parameter	Value	Device Parameter	Value
Operation frequency	3.12MHz (Measured) 3.18MHz (ANSYS)	Bandwidth	2.867kHz (-3dB) 1.5kHz (-1dB)
Device thickness	60μm	Rate sensitivity	15.0μV/˚/sec (Measured)
Capacitive gap	200nm	Full-scale range	30,000˚/sec (ANSYS)
Polarization voltage	10V		

3.6. Discussion on the Performance Enhancement of High-frequency Yaw-rate Gyroscopes

The noise performance of gyroscopes has been limiting factor of the MEMS gyroscopes' applications to be expanded to the high-end inertial sensor markets, such as

automobiles and indoor passenger navigations [1, 43, 52, 65, 66]. The noise performance of rate gyroscopes can be improved by three methods in BAW gyroscopes: scaling, Q-factor enhancements, and optimizations in physical dimensions. Since the Coriolis force-induced deformation is directly proportional to the effective mass of the resonating proof mass as shown in (1), the sensitivity and MNEΩ are improved proportionally by scaling the physical dimension of the resonant mass. The second approach is to enhance mechanical Q-factors by the mechanical design of sensors. As reported in [12, 14] and shown in (3)-(5), the Q-factor is directly converted to the reduced loss in a gyroscope system, and the high Q-factor lowers TNEΩ level. Lastly, the optimization of gap sizes in capacitive transduction area is discussed. The optimal capacitive gap size is the function of aforementioned physical dimension and Q-factors. The detailed design strategy is discussed in this section.

3.6.1. Variable Map for Noise Analysis

The preparation for the optimized disk design starts from identifying the relations among the parameters that defines noise. Once wafer orientation is set, elasticity and physical dimension of the material defines the modes of operation and operating frequency. Then Q-factors, applied DC voltages, and interface electronics define the remaining performance parameters (Figure 30).

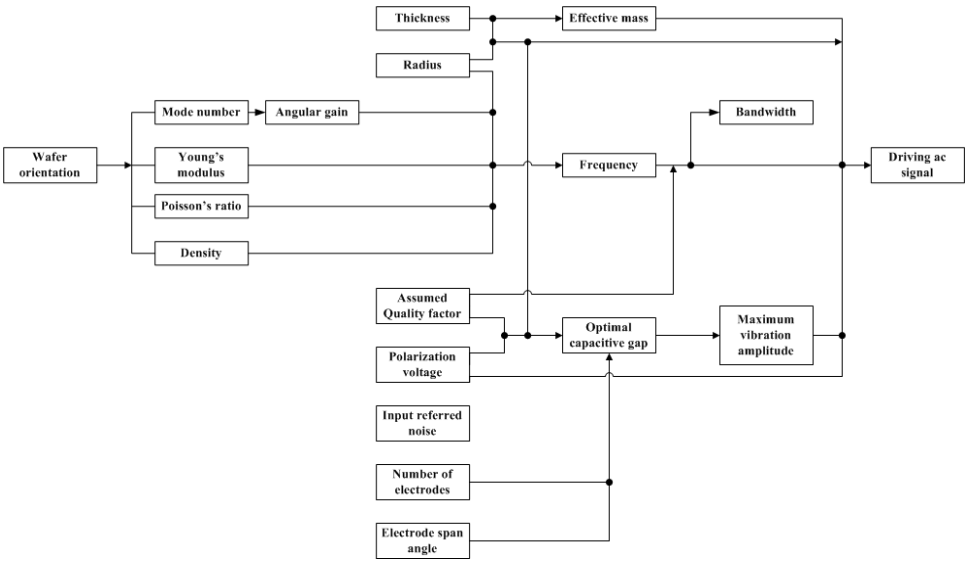

Figure 30: Variables map for the noise analysis of silicon BAW gyroscopes.

3.6.2. Scaling of Solid-disk Gyroscopes

Physical dimensions of BAW gyroscopes determine effective mass and the capacitive transduction area. Therefore, the dimensions, such as radius (R) and thickness (h) of a disk, are directly converted to the reduced noise level as shown in (38) and (39), and the parameters are listed in Table 4.

$$MNE\Omega = (3.47683e-8)\times\left(\frac{1}{d_0\cdot\sqrt{R\cdot h\cdot Q}}\right)\left[\deg/hour/\sqrt{Hz}\right] \quad \textbf{(38)}$$

$$ENE\Omega = \frac{(3.70771e17)\times d_0\cdot i_{noise}}{N\cdot V_p\cdot R\cdot h\cdot Q}\quad \left[\deg/\ hour\ /\sqrt{Hz}\right] \quad \textbf{(39)}$$

Table 4: Variables for the noise analysis.

No.	Variable	Definition	No.	Variable	Definition
1	d_0	Capacitive gap size	5	N	Number of sense electrodes
2	R	Disk radius	6	V_P	Polarization voltage
3	h	Disk thickness	7	Q	Quality factor
4	i_{noise}	Input-referred noise			

3.6.3. Q-factor enhancement

A Q-factor, which is the measure of the total loss existing in a resonating body, is the most critical parameter for the performance improvement of gyroscopes because both MNEΩ and ENEΩ decrease without an increase in dimensions. As shown in (40), the overall Q-factor can be decomposed into four dominant loss terms: Q_{Air}, $Q_{Support}$, $Q_{Surface}$, and Q_{TED}. Since Q_{Air} is a loss generated by a gyroscopes' random collision with the surrounding medium, Q_{Air} can be minimized by packaging or testing the device in a high vacuum environment [42, 67]. The second term, $Q_{Support}$, is the acoustic energy loss through the supporting structure. In the axis-symmetric center-supported disk resonators operating in a 1-10MHz range, the center is defined as a motionless part in the resonating body, and thus support loss becomes trivial [67, 68] . $Q_{Surface}$ is also negligible loss, in general, because of the large surface-to-volume ratio of the disk gyroscopes. The fourth term, the thermoelastic damping (TED), is related to the expansion and compression of the resonating body and the loss caused by irreversible heat dissipation [69-71]. In this section, the contribution of release holes is proven to cause the dominant TED-related loss, and the results are discussed by Comsol multi-physics simulation results.

$$Q_{Overall} = \left[\frac{1}{Q_{Air}} + \frac{1}{Q_{Support}} + \frac{1}{Q_{Surface}} + \frac{1}{Q_{TED}} + \frac{1}{Q_{Other}} \right]^{-1}. \quad \textbf{(40)}$$

As shown in Figure 31, two types of geometries are used to verify TED of disk-shaped gyroscopes at secondary elliptic (N=3) modes: non-perforated gyroscopes (Figure 31, left) and perforated gyroscopes (Figure 31, right).

The first step of simulation works is to verify the effect of the location of release holes on the Q_{TED} as shown in Figure 32. The simulations are executed by introducing four or eight release holes with 20µm-sized diameter inside a 1.2mm disk, and the radial location of the release holes is moved from 50µm to 550µm. The results prove that the location and number of release holes affect the Q_{TED}.

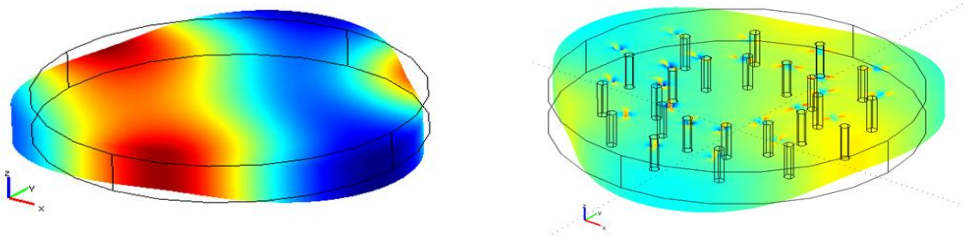

Figure 31: Example mode shapes of N=3 modes of a non-perforated solid-disk (left) and a perforated-disk gyroscope (right).

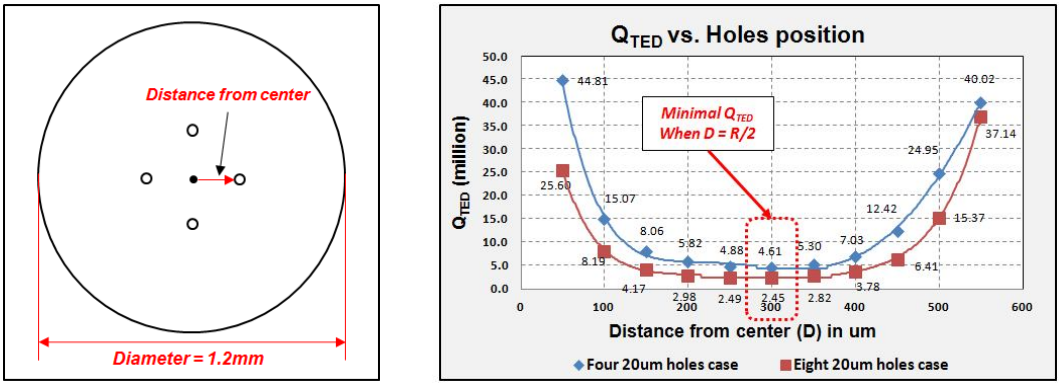

Figure 32: Q_{TED} and frequency of a perforated disk.

Then, the number of release holes is increased in proportional to the disk radius to verify the relationship between scaling of the disk and Q_{TED}. Two cases of the simulations are done as follows: (1) increasing the disk radius without perforations, and (2) increasing the disk radius by introducing the number of perforations that is increased in proportional to the enlarged radius of the disk. The scaling of the solid disk increased

Q_{TED} linearly, and the perforated-disk case proves that Q_{TED} stays below 350,000 because the increased number of perforations compensates the benefit from scaling of the disk (Figure 33).

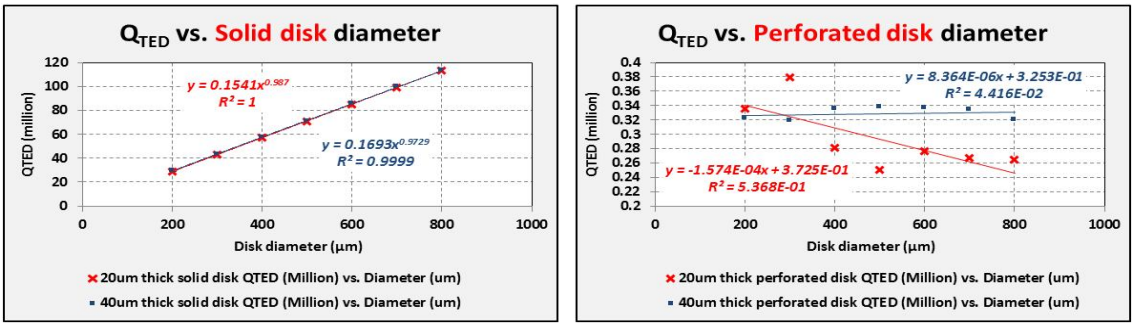

Figure 33: Q_{TED} of non-perforated disk gyroscopes (left) and Q_{TED} comparison with perforated disks (right).

Table 5: Q_{TED} differences between perforated and non-perforated disk gyroscopes.

Diameter (40µm thick)	Solid-disk Q_{TED}	Perforated-disk Q_{TED} (extrapolated)	Comparison
600µm	85 million	336 k	250x
2000µm	275 million	342 k	804x
4000µm	540 million	359 k	1504x
6000µm	802 million	375 k	2138x

3.6.4. Optimization of Capacitive Gap Sizes

The overall noise behavior is shown in Figure 34. Once mechanical and electrical noise sources are plotted with respect to the capacitive gap sizes, an ENEΩ-dominant region and a MNEΩ-dominant region are found to exist in the total-noise-equivalent floor. Therefore, the optimal gap size with given physical parameters, $d_{0\_optimal}$, is verified to exist.

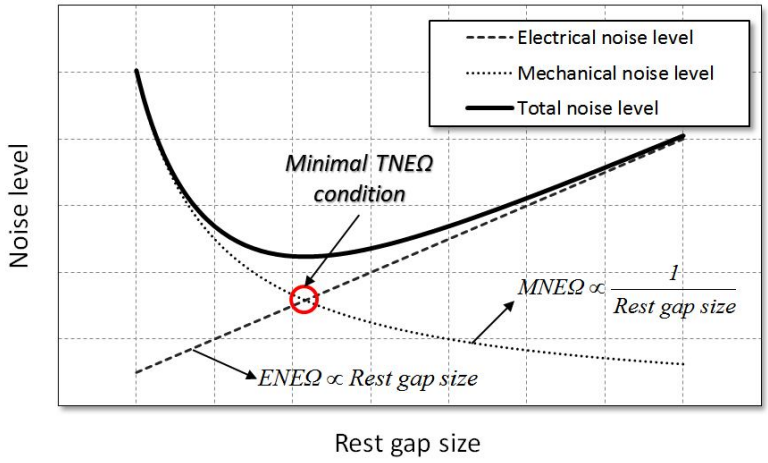

Figure 34: Noise trends with respect to the capacitive gap sizes.

$$Optimal\ d_0 = \sqrt{(3.12575e-27)\times\frac{N\cdot V_p\cdot\theta_{Span}\cdot\sqrt{R\cdot h\cdot Q}}{i_{noise}}}\ . \qquad \textbf{(41)}$$

For the optimal capacitive gap size ($d_{0\_optimal}$) analysis, all variables that determine noise level are drawn by a chart to show the relationship among the parameters as shown in Figure 30, and the $d_{0\_optimal}$ is calculated as shown in (41).

3.6.5. Process Flow of High-performance Disk Gyroscopes

As discussed earlier, Q_{TED} is heavily improved when perforations inside resonant mass are eliminated. Therefore, the fabrication processes that retain self-aligned center support without perforations should be developed.

Figure 35 shows HARPSS^{TM} process using HF release from backside of the substrate. The process flow employs the release holes patterned on the backside of handle layer in the SOI substrate. On the other hand, Figure 36 illustrates the conventional HARPSS^{TM} process flow fabricated on a customized SOI substrate with prepatterned buried oxide layer. The processes can establish the self-aligned supporting layer at the

bottom of resonating disks without perforations that can result in minimized losses in the devices.

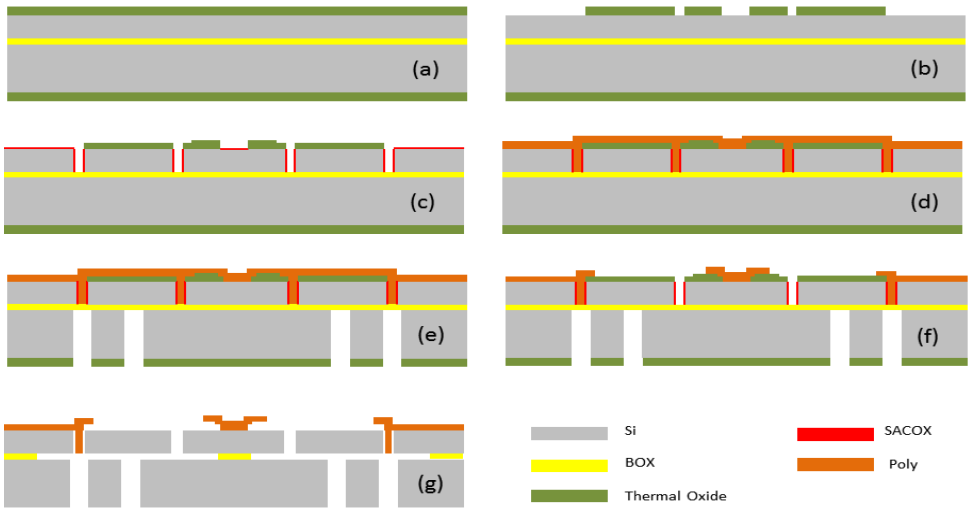

Figure 35: HARPSS^{TM} process with backside release.

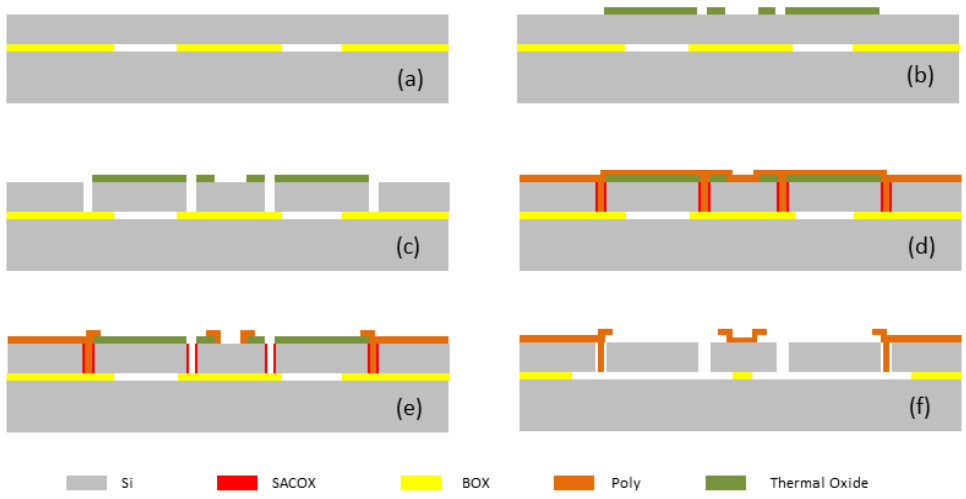

Figure 36: HARPSS^{TM} process fabricated in customized SOI substrate.

The fabricated device using the process flow described in Figure 35 is shown in Figure 37. The 100µm-thick, 4mm-diameter disk has self-aligned release holes around the center of the disk to define supporting structure, and measured Q-factor at N=2 mode

is shown as 244k. The corresponding mechanical noise level is supposed to be 0.1deg/hr/√Hz once operates as a gyroscope.

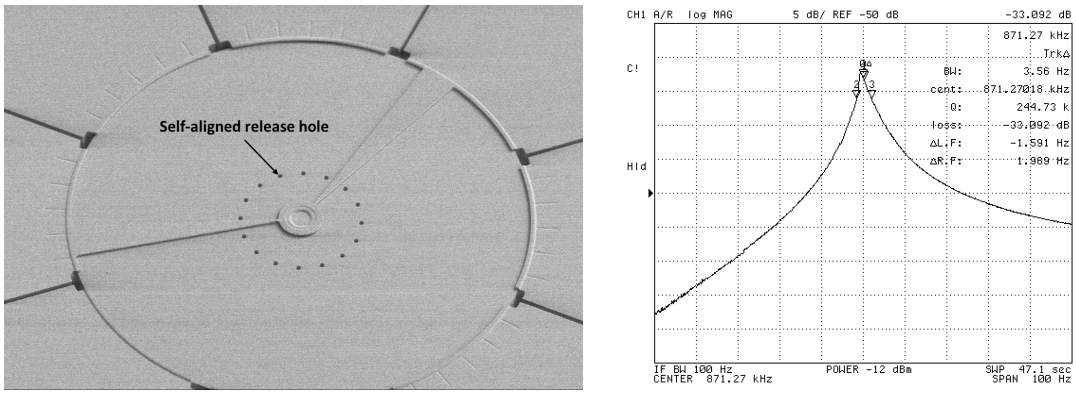

Figure 37: Fabricated 4mm-diameter pseudo-solid disk and measured Q-factor at N=2 in-plane resonance mode.

CHAPTER 4

HIGH-FREQUENCY PITCH/ROLL GYROSCOPE

4.1. Motivation

MEMS gyroscopes have gained remarkable attentions for myriads of three-dimensional motion recognition applications in handheld devices [1, 2]. For example, digital cameras are equipped with gyroscopes with low noise and steady bias stability for image stabilization, gaming consoles retain tri-axial gyroscopes with wide full-scale range for rapid motion sensing, and 3-D pointing devices in remote controllers possess inertial sensors for high resolution motion tracking.

Beyond the performance of contemporary MEMS gyroscopes, the emerging markets require demanding specifications with low noise and inert bias stability for indoor passenger navigation without guidance from GPS signal, e.g. dead reckoning, and harsh military applications [1] in a compact form factor. Several approaches have been introduced in attempts to realize robust, small form factor MEMS gyroscopes with multi-axes sensing capabilities.

The fundamental approaches to create tri-axial configuration of MEMS gyroscopes have been performed in two domains in general; assembling three identical single-axis yaw-rate gyroscopes in a three-dimensional orthogonal configuration [1, 3, 43] and batch-processing tri-axial gyroscopes in a planar substrate [1, 7, 8].

The first approach can achieve high performance tri-axial gyroscope with identical performances. However, the three dimensional gyroscopes assembly necessarily introduces a finite amount of initial angular offset error ($\Delta\vartheta$) caused by its relatively

inaccurate assembly process that is challenging to control precisely in micro-scale devices. Complicated calibration procedure is required, therefore, to cancel out the cross-axis sensitivity component produced by $\Delta\vartheta$, which in turn increases manufacturing costs inadequate for high-volume production. In addition, considering the thickness restriction of $\leq$ 1mm for the most of electrical components in general mobile devices, the increase in thickness of 3-D assembly disables various applications.

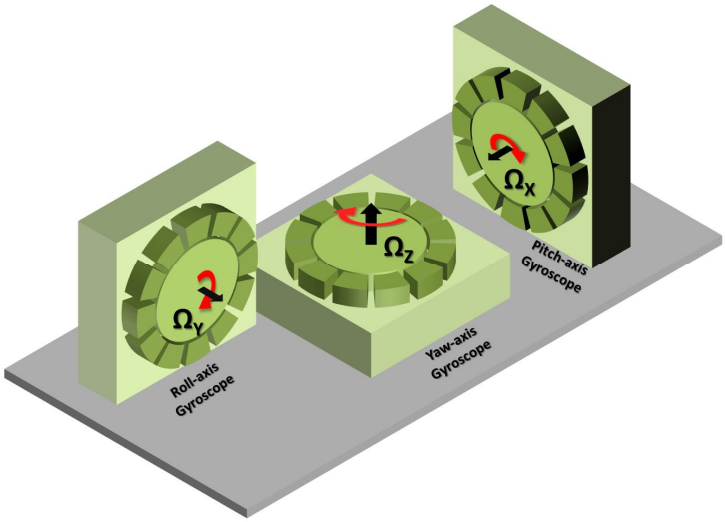

Figure 38: Tri-axial gyroscope assembly using three identical yaw devices.

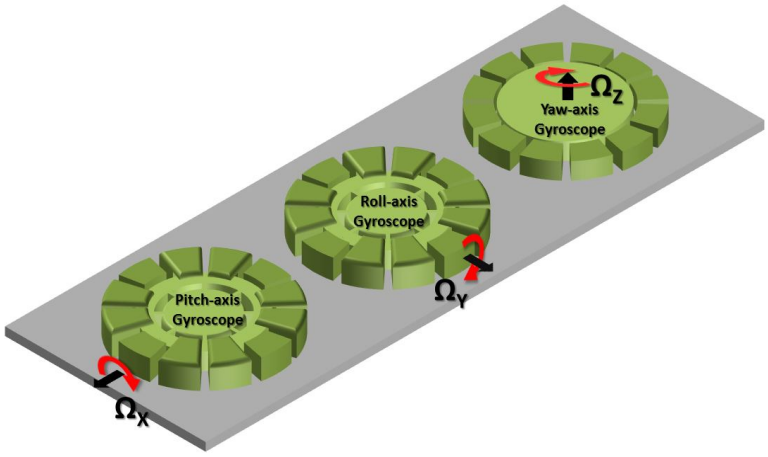

Figure 39: Tri-axial gyroscope co-fabricated in a planar substrate.

In this section, high frequency, high-Q, mode-matched pitch- and roll planar gyroscopes are presented. The high frequency of operation and high quality factor of the device reduce Brownian noise floor to several orders of magnitude less than its low frequency counterparts allowing the device to maintain a high resolution whereas increasing its operational bandwidth over ~50 Hz. In addition, high frequency operation benefits immunity to environmental vibration noise and shock tolerances [6, 8, 9, 49]. At the same time, mode-matching between two non-degenerate modes, i.e. in-plane drive-mode and out-of-plane sense-modes, is enabled to address process non-idealities via electrical tuning/detuning methods. Furthermore, since the identical pitch/roll devices are co-fabricated next to each other on the same substrate, the amount of $\Delta\vartheta$ is the same to the integrated devices hence reduces difficulty in post-fabrication calibration procedure.

Furthermore, the revised HARPSS^{TM} process [5, 8] is developed to yield

- broadened and enhanced the device frequency tunability,
- minimized cross-mode tuning behavior,
- improved signal isolation between in-plane drive and out-of-plane sense modes,
- reduced the magnitude of the quadrature signal component fed through the sense electrodes,
- and inertial measurement unit (IMU) integration in a single chip.

4.2. Operating Principle of Annulus Planar Gyroscope

Figure 40 shows mode-shapes employed in the dual-axes gyroscope. The annulus resonant mass is excited into primary elliptical in-plane resonance mode which has anti-nodes aligned to x- and y-axis [8, 22-24, 50, 51]. The applied rotation rates from lateral axis cause energy transfer from in-plane drive-mode to out-of-plane direction coupled by

Coriolis force. The deflection to out-of-plane mode is proportional to the input rotation rate and detected by top electrodes placed on top of the annulus mass with sub-micron capacitive air gaps.

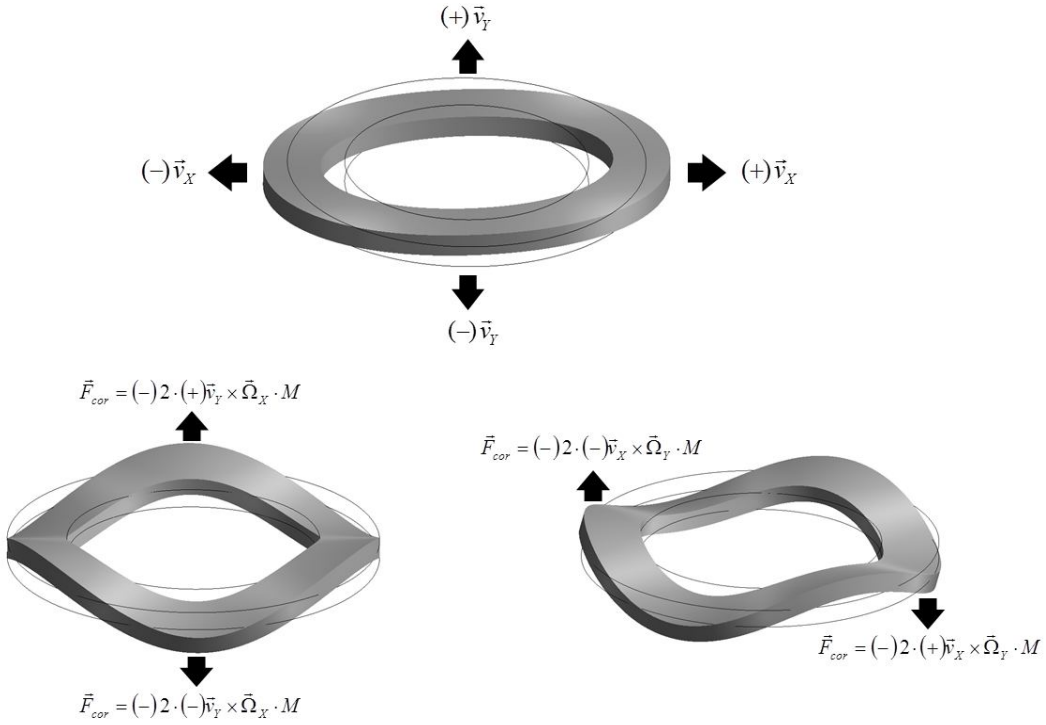

Figure 40: Primary elliptical in-plane drive-mode (top), secondary elliptical out-of-plane sense modes (bottom).

The employed secondary elliptical out-of-plane sense modes are supposed to exhibit identical frequency because of the degenerate property of eigen-frequencies on (100) substrate. In addition, the pair of sense-modes has anti-nodes aligned to nodal location with respect to each other (Figure 41). Therefore, the sense-mode responding to x-axis rotation does not affect the y-axis sensing mode, vice versa.

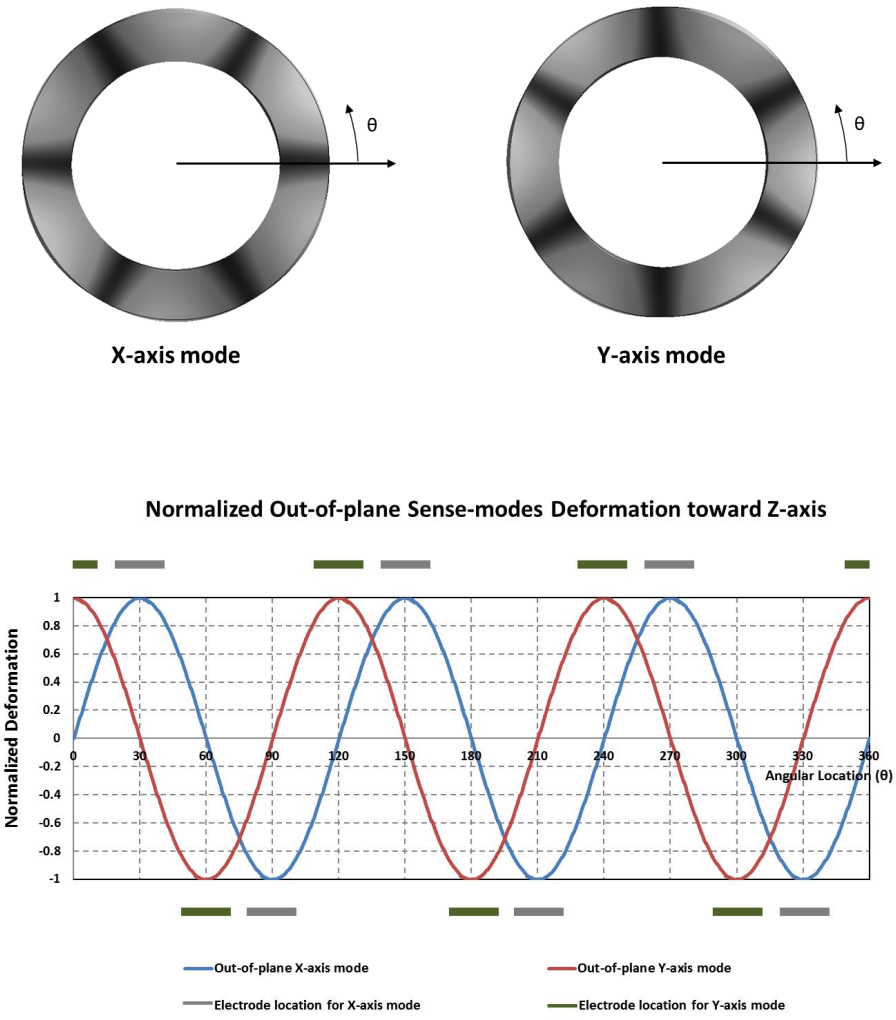

Figure 41: Directional deformation toward Z-axis of out-of-plane sense-modes.

4.3. Design of Annulus Gyroscope

The behavior of resonant annulus gyroscopes can be expressed by the simplified second-order equations.

$$M_D \cdot \frac{d^2}{dt^2} q_D + D_D \cdot \frac{d}{dt} q_D + K_D \cdot q_D = F_D. \tag{42}$$

$$M_S \cdot \frac{d^2}{dt^2} q_S + D_S \cdot \frac{d}{dt} q_S + K_S \cdot q_S = 2M_D \cdot \lambda' \cdot \Omega \cdot \frac{d}{dt} q_D. \tag{43}$$

where $M_{D,S}$, $q_{D,S}$, $D_{D,S}$, $K_{D,S}$, λ', and Ω are effective mass, vibration amplitude, damping factor, effective spring constant, Coriolis-coupling coefficient, and input rotation rate. Due to the orthogonal behavior of M=3 out-of-plane sense-modes, this section will discuss one of the M=3 modes as the out-of-plane sense-mode ($\cos(3\theta)$-mode), i.e. y-axis mode, and N=2 in-plane drive-mode ($\cos(2\theta)$-mode).

The analysis procedure will start from investigation of N=2 in-plane drive-mode. The excitation force and required AC voltage will be inspected followed by motional resistance and tuning behavior. M=3 out-of-plane sense mode is studied to identify Coriolis-force induced displacement and output current through sensing electrodes. Brownian noise level, full-scale range, dynamic range, and tuning behavior of sense-mode will be discussed accordingly.

4.3.1. Drive-mode Characteristic

4.3.1.1. Capacitance at Drive-electrodes

Prior to detailed derivation procedure, capacitance between the resonant mass and the side electrode at N=2 drive resonance mode should be analyzed. The N=2 drive-mode, and the interacting drive-in/out electrodes can be simplified as shown in Figure 42.

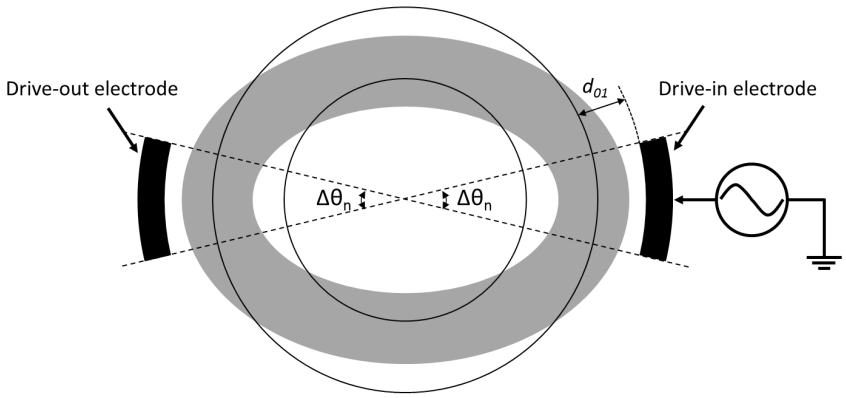

Figure 42: Schematic view of N=2 in-plane drive-mode in annulus gyroscope.

The drive-in/out electrodes retains the same rest gap sizes (d_{01}) and spanned angle ($\Delta\theta_n$) for the symmetric signal transductions from N=2 drive resonance mode. The capacitance of the drive-mode at its resonance is modeled as follows:

$$C_D = \int \frac{\varepsilon_0}{d_{01} + \Delta d} \cdot dA = \int_{\theta - \frac{\Delta\theta_n}{2}}^{\theta + \frac{\Delta\theta_n}{2}} \frac{\varepsilon_0 \cdot h}{d_{01} + \Delta d} \cdot R \cdot d\theta = \frac{\varepsilon_0 \cdot h \cdot R}{d_{01}} \int_{\theta - \frac{\Delta\theta_n}{2}}^{\theta + \frac{\Delta\theta_n}{2}} \frac{1}{1 + \frac{\Delta d}{d_0}} d\theta. \quad \textbf{(44)}$$

where ε_0, d_{01} and Δd are permittivity of free space, rest side air gap size, and change in the capacitive gap size due to vibration of the mass, respectively. h is the height of mass, R is the outer-radius of the mass, θ is offset angle between center of electrode and anti-node of N=2 drive-mode, and $\Delta\theta_n$ is spanned angle of the interacting side electrode. Since (100) substrate provides N=2 in-plane modes aligned to <100> and <110> orientation on the wafer with negligible angular offset, θ is ignored. Considering vibration amplitude is set as 10% of the nominal capacitive gap size ($\Delta d / d_0 << 1$), (44) can be expanded using Taylor series as follows:

$$C_D = \frac{\varepsilon_0 \cdot h \cdot R}{d_{01}} \int_{-\frac{\Delta\theta_n}{2}}^{+\frac{\Delta\theta_n}{2}} \left[1 - \frac{\Delta d}{d_{01}} + \left(\frac{\Delta d}{d_{01}} \right)^2 - \cdots \right] d\theta. \tag{45}$$

Since the N=2 in-plane drive-mode has radial deformation that can be expressed as $\Delta d = q_1 \cos(2\theta)$, therefore (45) becomes:

$$\begin{aligned} C_D &= \frac{\varepsilon_0 \cdot h \cdot R}{d_{01}} \left\{ \int_{-\frac{\Delta\theta_n}{2}}^{+\frac{\Delta\theta_n}{2}} d\theta - \int_{-\frac{\Delta\theta_n}{2}}^{+\frac{\Delta\theta_n}{2}} \frac{q_1 \cos(2\theta)}{d_{01}} d\theta + \int_{-\frac{\Delta\theta_n}{2}}^{+\frac{\Delta\theta_n}{2}} \left[\frac{q_1 \cos(2\theta)}{d_{01}} \right]^2 d\theta - \cdots \right\} \\ &\cong \frac{\varepsilon_0 \cdot h \cdot R}{d_{01}} \left[\Delta\theta_n - \frac{q_1 \sin(\Delta\theta_n)}{d_{01}} + \left(\frac{q_1}{d_{01}} \right)^2 \cdot \left(\frac{\Delta\theta_n}{2} + \frac{\sin(2\Delta\theta_n)}{4} \right) \right] \\ &\cong \left(\frac{\varepsilon_0 \cdot h \cdot R}{d_{01}} \Delta\theta_n \right) - \frac{\varepsilon_0 \cdot h \cdot R}{{d_{01}}^2} \cdot \left[q_1 \cdot \sin(\Delta\theta_n) - \left(\frac{q_1}{d_{01}} \right)^2 \cdot \left(\frac{\Delta\theta_n}{2} + \frac{\sin(2\Delta\theta_n)}{4} \right) \right] \\ &= C_{D0} + \Delta C_D. \end{aligned} \tag{46}$$

From (46), the initial capacitance at the rest state of drive-mode and the capacitance change by resonance motion of N=2 in-plane drive-mode is approximated by:

$$C_{D0} \cong \left(\frac{\varepsilon_0 \cdot h \cdot R}{d_{01}} \cdot \Delta\theta_n \right). \tag{47}$$

$$\Delta C_D \cong -\frac{\varepsilon_0 \cdot h \cdot R}{{d_{01}}^2} \cdot \left[q_1 \cdot \sin(\Delta\theta_n) - \left(\frac{q_1}{d_{01}} \right)^2 \cdot \left(\frac{\Delta\theta_n}{2} + \frac{\sin(2\Delta\theta_n)}{4} \right) \right]. \tag{48}$$

4.3.1.2. Applied AC Voltage vs. Excitation Force

To properly approximate the required excitation force to generate the driving amplitude to 10% of nominal capacitive gap size, the applied AC voltage should be identified. From (42), the drive-mode at its resonance is simplified as:

$$D_D \cdot \frac{d}{dt} q_D = F_D \tag{49}$$

In capacitive actuation, excitation force (F_D) is explained by the well-known equation:

$$F_D(r) = \frac{d}{dr}\left[\frac{1}{2} C \cdot V^2\right] = \frac{1}{2} \cdot V^2 \cdot \frac{d}{dr} C_D. \tag{50}$$

where V is voltage signal applied to the electrode, and C is capacitance between the side electrode and the resonant mass. The V has DC and AC component and expressed as follows:

$$V^2 = \left[\left(V_P - V_{Bias}\right) + v_{ac}\right]^2. \tag{51}$$

where V_P is DC polarization voltage applied to the resonant mass, V_{Bias} represents DC voltage that biases drive-in electrode, and v_{ac} is the ac excitation signal. From (46) and (51), (50) becomes

$$\begin{aligned} F_D(r) &= \frac{1}{2} \cdot \left[\left(V_P - V_{Bias}\right) + v_{ac}(t)\right]^2 \cdot \frac{d}{dr}\left[\begin{array}{l} \left(\frac{\varepsilon_0 \cdot h \cdot R}{d_{01}} \Delta\theta_n\right) \\ -\frac{\varepsilon_0 \cdot h \cdot R}{{d_{01}}^2} \cdot \left[q_1 \cdot \sin\left(\Delta\theta_n\right) - \left(\frac{q_1}{d_{01}}\right)^2 \cdot \left(\frac{\Delta\theta_n}{2} + \frac{\sin\left(2\Delta\theta_n\right)}{4}\right)\right] \end{array}\right] \\ &\cong \frac{1}{2} \cdot \left(V_P - V_{Bias}\right)^2 \cdot \left(-\frac{\varepsilon_0 \cdot h \cdot R}{{d_{01}}^2} \cdot \sin\left(\Delta\theta_n\right)\right) + \frac{1}{2} \cdot v_{ac}(t)^2 \cdot \left(-\frac{\varepsilon_0 \cdot h \cdot R}{{d_{01}}^2} \cdot \sin\left(\Delta\theta_n\right)\right) \\ &\quad - \left(V_P - V_{Bias}\right) \cdot v_{ac}(t) \cdot \left(-\frac{\varepsilon_0 \cdot h \cdot R}{{d_{01}}^2} \cdot \sin\left(\Delta\theta_n\right)\right). \end{aligned} \tag{52}$$

DC-term should be ignored because electrostatic force generated by DC voltage is not the function of radial deformation. Assuming small AC signal ($v_{ac}(t) << 1$) is applied,

$v_{ac}(t)^2$-term can be ignored. Therefore, electrostatic force applied from the drive-in electrode is calculated by:

$$F_D(r) = -(V_P - V_{Bias}) \cdot v_{ac}(t) \cdot \frac{\varepsilon_0 \cdot h \cdot R}{{d_{01}}^2} \cdot \sin(\Delta\theta_n). \quad \textbf{(53)}$$

4.3.1.3. Applied AC Voltage vs. Vibration Amplitude of Drive-mode

Since the radial deformation of the drive mode follows time-varying sinusoidal form, $q_D = q_1 \cdot \sin(\omega_0 \cdot t)$, (49) and (53) give the relationship between excitation voltage and driving amplitude.

$$v_{ac}(t) = \left[\frac{{\omega_0}^2 \cdot M_D}{Q_D \cdot (V_P - V_{Bias})}\right] \cdot \left[\frac{{d_{01}}^2}{\varepsilon_0 \cdot h \cdot R \cdot \sin(\Delta\theta_n)}\right] \cdot q_1 \cdot \cos(\omega_0 \cdot t). \quad \textbf{(54)}$$

Based on (54), there is 90˚ phase difference between applied AC voltage and the mechanical vibration amplitude of the drive resonance mode.

4.3.1.4. Output Current Induced by Drive-mode Resonance

The radial deformation of N=2 in-plane drive-mode has the same radial deformation in the resonant mass at drive-in and out electrodes. The output current through capacitive air gap is expressed in a general equation.

$$i_{output}(t) = (V_P - V_{Bias}) \cdot \frac{dC_D}{dt}. \quad \textbf{(55)}$$

By equating (46) and (55), the output current at drive-out electrode is approximated as follows:

$$\begin{aligned} i_{output}(t) &= (V_P - V_{Bias}) \cdot \frac{dC_D}{dt} = (V_P - V_{Bias}) \cdot \frac{dC_D}{dq_D} \cdot \frac{dq_D}{dt} \\ &= (V_P - V_{Bias}) \cdot \left[\frac{\varepsilon_0 \cdot h \cdot R}{{d_{01}}^2} \cdot \sin(\Delta\theta_n) \right] \cdot (\omega_0 \cdot q_1) \cdot \sin(\omega_0 \cdot t). \end{aligned} \quad \textbf{(56)}$$

Interestingly, the phase of output current at drive-out electrode is in-phase with mechanical vibration whereas the current has 90°-off phase from input excitation voltage.

4.3.1.5. Motional Impedance of Drive-mode

The applied AC voltage excitation signal induces mechanical resonance in the mass, and the resonance of the mass generates output current at drive-out electrode. As a result, the resonant system exhibits mechanical impedance caused by the resonance of the mass. The motional impedance is obtained by taking ratio between the drive-in voltage and output current as shown follows:

$$R_M = \left| \frac{v_{ac,in}(t)}{i_{output}(t)} \right| = \frac{\omega_0 \cdot M_D}{Q_D} \cdot \frac{{d_{01}}^4}{[\varepsilon_0 \cdot h \cdot R \cdot (V_P - V_{Bias}) \cdot \sin(\Delta\theta_n)]^2}. \quad \textbf{(57)}$$

4.3.1.6. Drive-mode Tuning Behavior

Since the annulus gyroscope employ non-degenerate modes between drive and sense-modes, process variations in the thickness and lateral dimension shift the frequencies from the designed values. To ensure the mode-matched operation under the process deviations, the resonant modes must retain sufficient electrostatic frequency

tunability to compensate frequency split (Δf). A dedicated set of electrodes are assigned to tune the N=2 in-plane drive-mode as shown in Figure 43. The spanned angle (Δθ) of the drive-mode tuning electrodes is defined the same as drive-in/out electrodes for the symmetry of annulus mass and side electrodes.

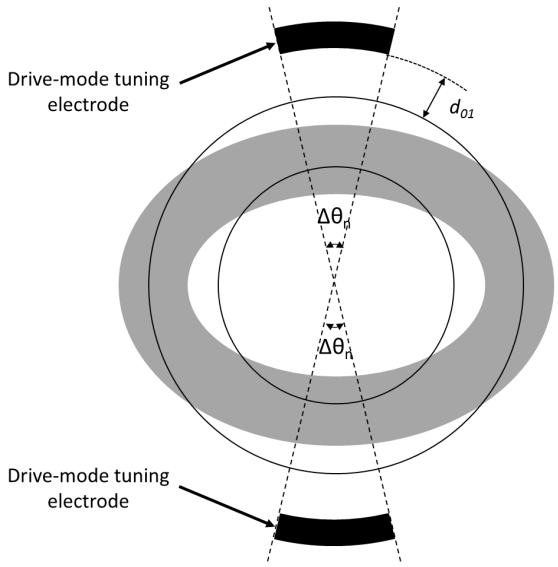

Figure 43: Tuning electrodes of N=2 in-plane drive-mode.

The resonant frequency is defined by general equation as follows:

$$\omega_{Tuned} = \sqrt{\frac{K_{Total}}{M_{eff}}} = \sqrt{\frac{K_{Mechanical} + K_{Electrical}}{M_{eff}}}. \quad \textbf{(58)}$$

where K_{Total}, $K_{Mechanical}$, and $K_{Electrical}$ are total spring constant, mechanical spring constant, and electrical spring constant, respectively. M_{eff} is the effective mass of resonance mode. $K_{Mechanical}$ is fixed value at the resonance mode if the resonant frequency and effective mass is defined. However, $K_{Electrical}$ is defined by voltage across the capacitive gap and the capacitance. $K_{Mechanical}$ and $K_{Electrical}$ can be re-written as follows:

$$K_{Mechanical} = \omega_0^{\,2} \cdot M_D. \tag{59}$$

$$\begin{aligned} K_{Electrical} &= -\frac{d}{dr} F_D \\ &= -N_{TD} \cdot \frac{\left(V_P - V_{Tuning}\right)^2}{2} \cdot \frac{d^2}{dr^2} \left\{ \frac{\varepsilon_0 \cdot h \cdot R}{d_{01}} \cdot \left[\Delta\theta_n - \frac{q_1 \sin\left(\Delta\theta_n\right)}{d_{01}} + \left(\frac{q_1}{d_{01}}\right)^2 \cdot \left(\frac{\Delta\theta_n}{2} + \frac{\sin\left(2\Delta\theta_n\right)}{4}\right) \right] \right\} \\ &= -N_{TD} \cdot \left(V_P - V_{Tuning}\right)^2 \cdot \left(\frac{\varepsilon_0 \cdot h \cdot R}{d_{01}^{\,2}}\right) \cdot \left(\frac{\Delta\theta_n}{2} + \frac{\sin\left(2\Delta\theta_n\right)}{4}\right). \end{aligned} \tag{60}$$

where N_{TD} is the number of drive-mode tuning electrodes.

The tuned resonance frequency with applied DC in-plane mode tuning voltage is expressed by:

$$\begin{aligned} \omega_{Tuned}^{\,2} &= \frac{K_{Mechanical} + K_{Electrical}}{M_D} = \omega_0^{\,2} + \frac{K_{Electrical}}{M_D} \\ &= \omega_0^{\,2} - \frac{1}{M_D} \cdot \left(V_P - V_{Tuning}\right)^2 \cdot \frac{N_{TD} \cdot \varepsilon_0 \cdot h \cdot R}{d_{01}^{\,3}} \cdot \left(\frac{\Delta\theta_n}{2} + \frac{\sin\left(2 \cdot \Delta\theta_n\right)}{4}\right). \end{aligned} \tag{61}$$

Therefore, electrostatically tuned resonance frequency becomes

$$f_{Tuned} = f_0 \cdot \sqrt{1 - \frac{1}{K_{Mechanical}} \cdot \left(V_P - V_{Tuning}\right)^2 \cdot \frac{N_{TD} \cdot \varepsilon_0 \cdot h \cdot R}{d_{01}^{\,3}} \cdot \left(\frac{\Delta\theta_n}{2} + \frac{\sin\left(2 \cdot \Delta\theta_n\right)}{4}\right)}. \tag{62}$$

4.3.2. Sense-mode Characteristic

4.3.2.1. General Equation in Motion of Sense-mode

Lagrange's equation that explains a resonant system is introduced as below [21, 50, 72]:

$$\frac{d}{dt}\left(\frac{\partial L}{\partial \dot{q}_j}\right)-\frac{\partial L}{\partial q_j}+\frac{\partial D}{\partial \dot{q}_j}=0. \tag{63}$$

which simplifies (43) into:

$$\frac{d^2}{dt^2}q_2+2\cdot\xi_n\cdot\omega_n\cdot\frac{d}{dt}q_2+\omega_n{}^2\cdot q_2=2\cdot\lambda'\cdot\Omega_Y\cdot\frac{d}{dt}q_D. \tag{64}$$

where q_2 is sense-mode vibration mode induced by Coriolis force, ξ_n is damping factor in the sense-mode, ω_n is natural frequency of sense-mode, λ' is Coriolis-coupling coefficient, Ω_Y is rotation rate applied from y-axis, and q_D is vibration function of drive mode which is described as $q_D=q_1\cdot\sin(\omega_0\cdot t)$ earlier. By equating (64) with $\xi_n=\frac{1}{2\cdot Q_S}$, following sense-mode amplitude is obtained.

$$q_2(j\omega_n)=\frac{2\cdot\lambda'\cdot\Omega_Y\cdot\omega_0\cdot q_1\cdot\cos(\omega_0\cdot t-\phi)}{\left(\omega_n{}^2-\omega_0{}^2\right)+j\cdot\left(\frac{\omega_n\cdot\omega_0}{Q}\right)}. \tag{65}$$

The amplitude and phase response at Coriolis-force induced sense-mode vibration amplitude can be decomposed as follows:

$$|q_2(j\omega_n)|=\frac{2\cdot\lambda'\cdot\Omega_Y\cdot\omega_0\cdot q_1}{\sqrt{\left(\omega_n{}^2-\omega_0{}^2\right)^2+\left(\frac{\omega_n\cdot\omega_0}{Q_S}\right)^2}}. \tag{66}$$

and

$$\angle q_2(j\omega_n) = \tan^{-1}\left[\frac{\left(\frac{\omega_n \cdot \omega_0}{Q_S}\right)}{\omega_n{}^2 - \omega_0{}^2}\right]. \tag{67}$$

As a result, (64) can be re-written from (65) and (66).

$$q_2 = \frac{2 \cdot \lambda' \cdot \Omega_Y \cdot \omega_0 \cdot q_1}{\sqrt{\left(\omega_n{}^2 - \omega_0{}^2\right)^2 + \left(\frac{\omega_n \cdot \omega_0}{Q_S}\right)^2}} \cdot \cos\left(\omega_n - \tan^{-1}\left[\frac{\left(\frac{\omega_n \cdot \omega_0}{Q_S}\right)}{\omega_n{}^2 - \omega_0{}^2}\right]\right). \tag{68}$$

As shown in Figure 44, Coriolis-force induced sense-mode deflection becomes maximum when $\omega_n = \omega_0$, and the amplitude is proportional to Q-factor. Phase response of sense-mode shows phase is 90°-off from drive-mode motion at the maximum sensitivity regardless of Q-factor. In addition, under mode-split condition ($\omega_n \neq \omega_0$), phase relation between drive- and sense-modes becomes 0° to 90° range.

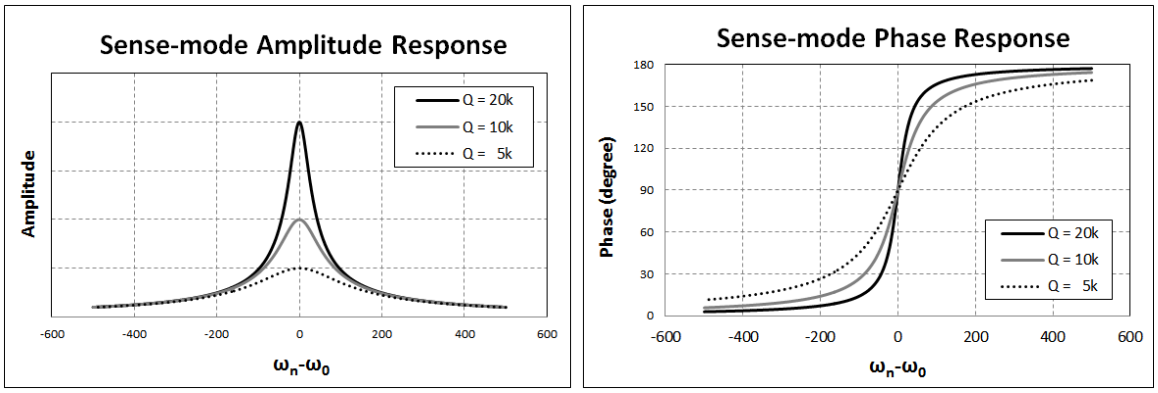

Figure 44: Sense-mode amplitude (left) and phase (right) response with respect to frequency split and Q-factors.

4.3.2.2. Full-scale Range of Annulus Gyroscope

Capacitive gyroscopes demonstrate linear response until the Coriolis-force induced deformation reaches 10% of the nominal sensing air gap size. Therefore, by equating (66) with Coriolis-force induced deformation equals to $0.1\times d_{02}$, the maximum rotation rate (Ω_Y) is calculated.

$$\Omega_Y\big|_{Max} = \frac{d_{02}}{20}\cdot\frac{\sqrt{\left(\omega_n{}^2-\omega_0{}^2\right)^2+\left(\frac{\omega_n\cdot\omega_0}{Q_S}\right)^2}}{\lambda'\cdot\omega_0\cdot q_1}. \qquad \textbf{(69)}$$

Figure 45 shows the full-scale range (FSR) with respect to frequency split ($=f_n-f_0$) and Q-factor. At mode-matched condition, $f_n - f_0 = 0$ Hz, energy transfer from drive-mode to sense-mode occurs with maximum efficiency resulting in Coriolis-force induced sense-mode amplitude larger than mode-split conditions ($f_n - f_0 \neq 0$ Hz) as shown in Figure 44 (left). Therefore, sense-mode amplitude reaches 10% of the nominal gap size with the lower input rotation rate compared to mode-split cases. The higher Q-factor affects FSR in a similar way. The efficient energy transfer with high-Q creates sense-mode amplitude higher than low-Q cases, and thus narrows FSR. In the design aspect, it is critical to adjust capacitive air gap size, Q-factor, operating frequency, and drive-mode vibration amplitude to achieve the targeted amount of FSR.

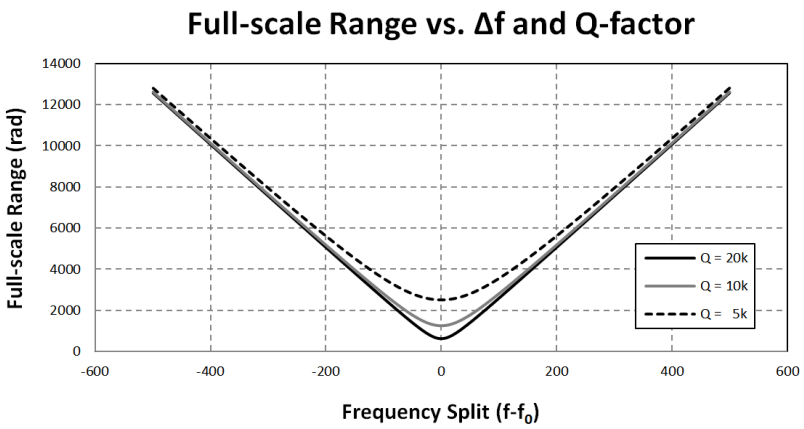

Figure 45: Full-scale range of annulus gyroscope. Operating frequency is assumed to be 1 MHz with sensing capacitive air gap size at 300nm to illustrate the exemplary response.

4.3.2.3. Brownian Noise Analysis

The Brownian motion of resonant gyroscope caused by random collision with surrounding air molecules draws the fundamental limit in the noise performance of the gyroscope system. The vibration amplitude caused by Brownian motion is defined as:

$$\left|q_{2,Brownian}\right| = \sqrt{\frac{4 \cdot k_B \cdot T \cdot Q_S}{M_S \cdot \omega_n^{\,3}}}. \tag{70}$$

The mechanical noise equivalent rotation-rate (MNEΩ) is obtained by equating (66) and (70).

$$MNE\Omega = \Omega_Y\big|_{\min} = \frac{1}{2 \cdot \lambda' \cdot q_1} \cdot \sqrt{\frac{4 \cdot k_B \cdot T \cdot Q_S}{M_S \cdot \omega_n}} \cdot \left(\frac{\omega_n}{\omega_0}\right) \cdot \sqrt{\left(1 - \frac{\omega_0^{\,2}}{\omega_n^{\,2}}\right)^2 + \left(\frac{\omega_0}{Q_S \cdot \omega_n}\right)^2}. \tag{71}$$

4.3.2.4. Dynamic Range of Annulus Gyroscope

The dynamic range (DR) of a gyroscope system is defined by the ratio between minimum detectable input rotation-rate to the maximum rotation-rate that the gyroscope can respond with linear output signal. By taking the FSR to MNEΩ ratio, DR is calculated as below:

$$DR = 20 \cdot \log\left(\frac{\Omega_Y\big|_{Max}}{\Omega_Y\big|_{\min}} \right) = 20 \cdot \log\left(\frac{d_{02}}{10} \sqrt{\frac{M_S \cdot \omega_n}{4 \cdot k_B \cdot T \cdot Q_S}} \right). \quad \textbf{(72)}$$

Since both FSR and MNEΩ are increased by the same amount when Δf ($=\omega_n - \omega_0$) exists, the effect from split of two resonance modes is cancelled out. In addition, DR is proportional to the log-scale of sense-mode frequency (ω_n), which suggests the advantage of high frequency operation.

4.3.2.5. Capacitance Variance at Sense-out Electrode

The Coriolis-force induced sense-mode exists toward out-of-plane direction. The resonant mode-shape of M=3 out-of-plane mode exists in an annulus object and the sensing-mechanism occurs with the interaction to the sensing plate placed on top of annulus with narrow gap (d_{02}) as shown in Figure 46.

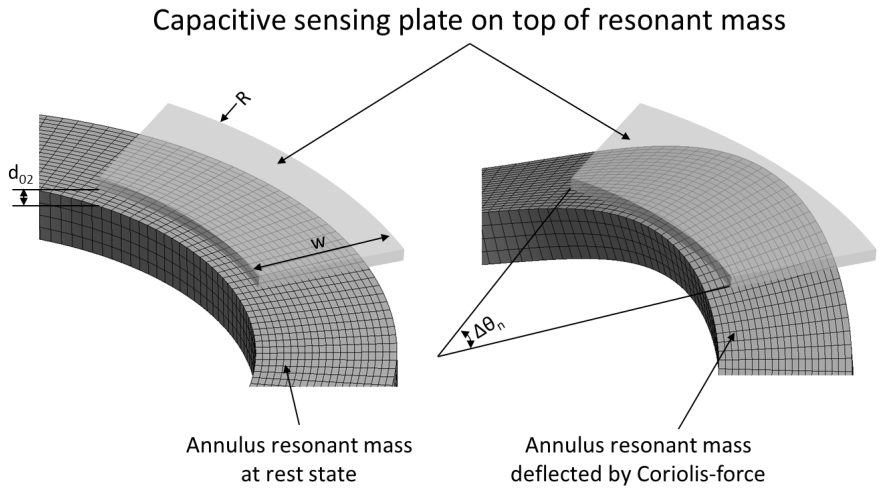

Figure 46: Annulus mass and top sensing electrode at static case (left) and resonance (right).

Unlike the N=2 in-plane drive-mode, the capacitive signal transduction of M=3 out-of-plane sense-mode undergoes two-dimensional deformation that is the function of radial and angular location of the sense-mode that can described as below:

$$q_S(r,\theta) = f(r)\cdot g(\theta). \tag{73}$$

where q_S is sense-mode deflection towards out-of-plane direction at the radial (r) and angular (θ) location of the annulus object. The equation (73) may be expressed by (74) assuming the radial deformation is proportional to r, and angular deformation is proportional to cos(3θ).

$$q_S(r,\theta) = \frac{q_2}{R - C_{anchor}}\cdot(r - C_{anchor})\cdot\cos(3\cdot\theta) = \Delta d_S. \tag{74}$$

where C_{anchor} is radius of central anchor, r is radial location of the out-of-plane sense-mode, and θ is the angular location of the sense-mode as shown in Figure 47.

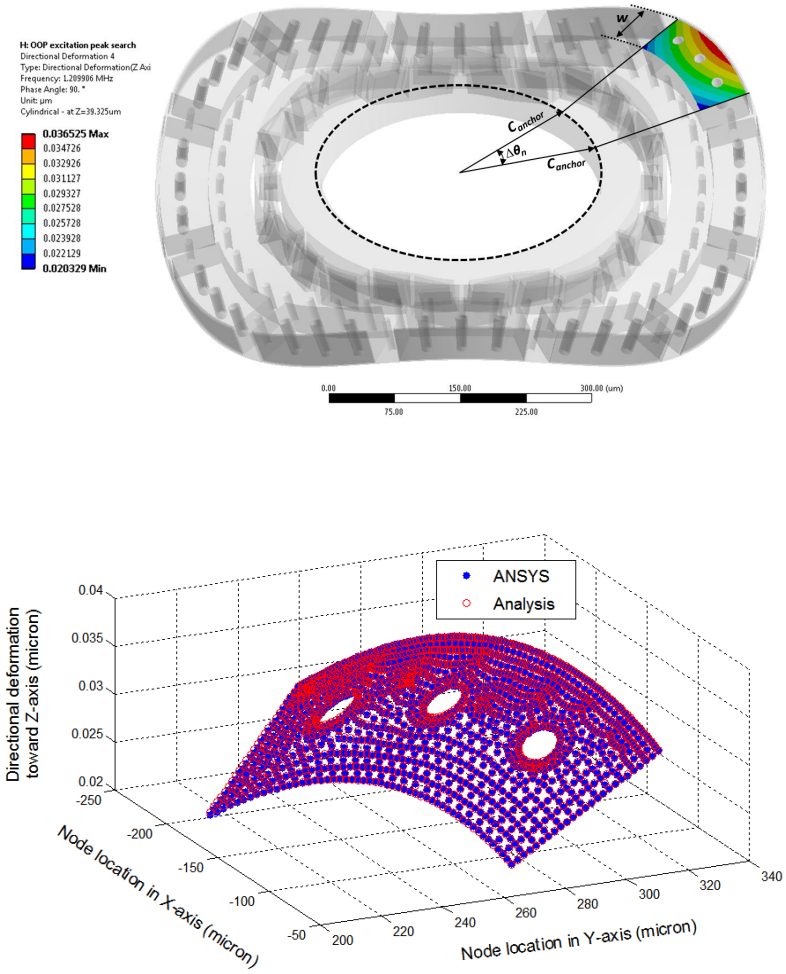

Figure 47: ANSYS simulation of cos(3θ) directional deformation (top). Analysis demonstrates excellent agreement with ANSYS model.

To approximate capacitance change of the out-of-plane sense-mode in a cylindrical coordinate, sense-mode capacitance is approximated by:

$$C_S(r,\theta) = \int_{\theta-\frac{\Delta\theta_n}{2}}^{\theta+\frac{\Delta\theta_n}{2}} \left(\int_{R-w}^{R} \frac{\varepsilon_0}{d_{02}+\Delta d_S} \cdot r \cdot dr \right) d\theta. \tag{75}$$

$$\Delta d_S = q_S = \frac{q_2}{R - C_{anchor}} \cdot (r - C_{anchor}) \cdot \cos(3 \cdot \theta). \tag{76}$$

Once the deformation toward out-of-plane direction is obtained, the capacitance between top sensing plate and annulus mass can be calculated.

$$C_S = \int_{\theta+\frac{\Delta\theta_n}{2}}^{\theta+\frac{\Delta\theta_n}{2}} \int_{R-w}^{R} \frac{\varepsilon_0}{d_{02}+\Delta d_S} \cdot r \cdot dr \cdot d\theta = \frac{\varepsilon_0}{d_{02}} \cdot \int_{\theta-\frac{\Delta\theta_n}{2}}^{\theta+\frac{\Delta\theta_n}{2}} \int_{R-w}^{R} \frac{1}{1+\frac{\Delta d_S}{d_{02}}} \cdot r \cdot dr \cdot d\theta \quad \textbf{(77)}$$

$$= \frac{\varepsilon_0}{d_{02}} \cdot \int_{\theta-\frac{\Delta\theta_n}{2}}^{\theta+\frac{\Delta\theta_n}{2}} \int_{R-w}^{R} \left[1 - \frac{C_S(r,\theta)}{d_{02}} + \left(\frac{C_S(r,\theta)}{d_{02}} \right)^2 - \cdots \right] \cdot r \cdot dr \cdot d\theta.$$

Assuming out-of-plane sense-mode doesn't have misalignment from cos(3θ) mode, i.e. φ=0˚ at cos(3θ-φ), C_S becomes

$$C_S = \frac{\varepsilon_0}{d_{02}} \cdot (A_1 + A_2 + A_3) \quad \textbf{(78)}$$

where

$$A_1 = \frac{\Delta\theta_n}{2} \cdot \left[R^2 - (R-w)^2 \right] \quad \textbf{(79)}$$

$$A_2 = -\frac{1}{9} \cdot \cos(3\cdot\theta) \cdot \sin\frac{3\cdot\Delta\theta_n}{2} \cdot \left[\frac{q_2}{d_{02}\cdot(R-C_{anchor})} \right] \cdot \left\{ \begin{matrix} 2\cdot\left[R^3-(R-w)^3\right] \\ -3\cdot C_{anchor}\cdot\left[R^2-(R-w)^2\right] \end{matrix} \right\}$$

$$A_3 = \frac{1}{12} \cdot \left[\begin{matrix} \frac{\Delta\theta_n}{2} \\ +\frac{1}{6}\cos(6\cdot\theta)\cdot\sin\left(\frac{3\cdot\Delta\theta_n}{2}\right) \end{matrix} \right] \cdot \left[\frac{q_2}{d_{02}\cdot(R-C_{anchor})} \right]^2 \cdot \left\{ \begin{matrix} 3\cdot\left[R^4-(R-w)^4\right] \\ -8\cdot C_{anchor}\cdot\left[R^3-(R-w)^3\right]+6\cdot {C_{anchor}}^2\cdot\left[R^2-(R-w)^2\right] \end{matrix} \right\}$$

4.3.2.6. Coriolis-force Induced Output Current

Therefore, Coriolis-force induced output current is expressed as follows:

$$
\begin{aligned}
i_{output}(t) &= (V_P - V_{Bias}) \cdot \frac{dC_S}{dt} = (V_P - V_{Bias}) \cdot \frac{dC_S}{dq_S} \cdot \frac{dq_S}{dt} \\
&\cong \frac{\varepsilon_0}{d_{02}} \cdot (V_P - V_{Bias}) \cdot \frac{d}{dq_2} \left\langle -\frac{1}{9} \cdot \cos\theta \cdot \sin\frac{3 \cdot \Delta\theta_n}{2} \cdot \left[\frac{q_2}{d_{02} \cdot (R - C_{anchor})} \right] \right\rangle \cdot \frac{d}{dt}[q_2 \cdot \sin(\omega_n \cdot t)] \\
&\quad \cdot \left\{ \begin{matrix} 2 \cdot \left[R^3 - (R-w)^3 \right] \\ -3 \cdot C_{anchor} \cdot \left[R^2 - (R-w)^2 \right] \end{matrix} \right\} \\
&= -\frac{1}{9} \cdot \frac{\varepsilon_0}{d_{02}} \cdot (V_P - V_{Bias}) \cdot \cos\theta \cdot \sin\frac{3 \cdot \Delta\theta_n}{2} \cdot \left[\frac{1}{d_{02} \cdot (R - C_{anchor})} \right] \cdot \left\{ \begin{matrix} 2 \cdot \left[R^3 - (R-w)^3 \right] \\ -3 \cdot C_{anchor} \cdot \left[R^2 - (R-w)^2 \right] \end{matrix} \right\} \\
&\quad \cdot \frac{2 \cdot \lambda' \cdot \Omega_Y \cdot \omega_0}{\sqrt{\left(\omega_n{}^2 - \omega_0{}^2 \right)^2 + \left(\frac{\omega_n \cdot \omega_0}{Q_S} \right)^2}} \cdot q_1 \cdot \cos(\omega_0 \cdot t).
\end{aligned}
\tag{80}
$$

As shown in (80), it is obvious that when θ = 0°, anti-node of M=3 out-of-plane sense-mode is aligned with top electrode then output current becomes maximum. On the other hands, at the nodes of the sense modes where the θ = 90° condition exists, output current becomes zero which means the mode-aligned annulus gyroscope will not exhibit cross-axis sensitivity.

4.3.2.7. Sense-mode Tuning Behavior

To address process variation and enforce manufacturing yield in case sense-mode frequency is higher than drive-mode frequency, sense-mode tuning method is introduced along with drive-mode tuning. The sense-mode tuning electrodes are placed on top of anti-nodes of out-of-plane cos(3θ) mode, as shown in Figure 48.

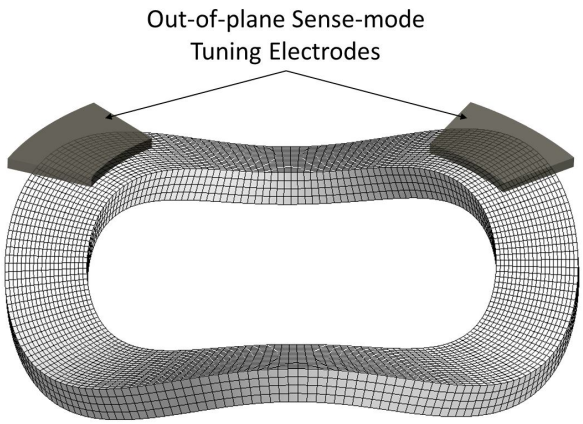

Figure 48: Exemplary location of sense-mode tuning electrodes.

Similarly to (59), electrical spring constant can be obtained as follows:

$$K_{Electrical} = -\frac{d}{dr}F_D = -\frac{\left(V_P - V_{Tuning}\right)^2}{2}\cdot\frac{d^2}{dq_2{}^2}\left\{\begin{array}{l}\dfrac{\varepsilon_0}{d_{02}}\cdot\dfrac{1}{12}\cdot\left[\begin{array}{l}\dfrac{\Delta\theta_n}{2}\\ +\dfrac{1}{6}\cos(6\cdot\theta)\cdot\sin\left(\dfrac{3\cdot\Delta\theta_n}{2}\right)\end{array}\right]\\ \cdot\left[\dfrac{q_2}{d_{02}\cdot\left(R-C_{anchor}\right)}\right]^2\cdot\left\{\begin{array}{l}3\cdot\left[R^4-(R-w)^4\right]\\ -8\cdot C_{anchor}\cdot\left[R^3-(R-w)^3\right]\\ +6\cdot C_{anchor}{}^2\cdot\left[R^2-(R-w)^2\right]\end{array}\right\}\end{array}\right\}$$

$$= -\left(V_P - V_{Tuning}\right)^2\cdot\left(\frac{\varepsilon_0}{d_{01}{}^3}\right)\cdot\frac{1}{12}\cdot\left[\begin{array}{l}\dfrac{\Delta\theta_n}{2}\\ +\dfrac{1}{6}\cos(6\cdot\theta)\cdot\sin\left(\dfrac{3\cdot\Delta\theta_n}{2}\right)\end{array}\right]$$

$$\cdot\left[\frac{1}{d_{02}\cdot\left(R-C_{anchor}\right)}\right]^2\cdot\left\{\begin{array}{l}3\cdot\left[R^4-(R-w)^4\right]\\ -8\cdot C_{anchor}\cdot\left[R^3-(R-w)^3\right]+6\cdot C_{anchor}{}^2\cdot w\end{array}\right\} \quad \textbf{(81)}$$

4.3.3. Substrate Orientation Determination.

As discussed drive- and sense-modes mechanics, the remaining work is to define substrate orientation. Currently (100), (110), and (111) orientation of silicon wafers are available, and the determination of the substrate material critically defines the operation and complexity of annulus gyroscopes in terms of quadrature components and mode coupling.

Silicon has anisotropic stiffness depending on the seed orientation and dicing direction as shown in Figure 49 and Figure 50 [73, 74]. Since Young's modulus needs to be periodic every 45° or 30° for the Z-axis gyroscope integration, (110) orientation of the silicon is unable to use. Z-axis gyroscope can operate at N=3 mode using (100) substrate by 90° periodic Young's modulus on in-plane. In addition, N=2 and N=3 modes can be used in (111) substrates because of the isotropic stiffness.

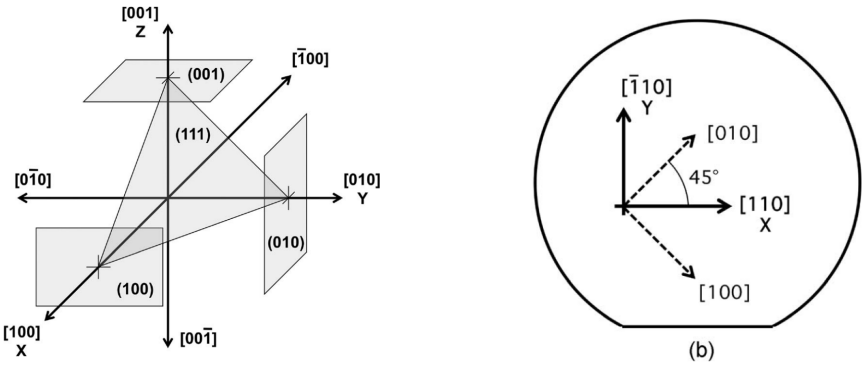

Figure 49: Orientation-dependent anisotropic Young's modulus of silicon.

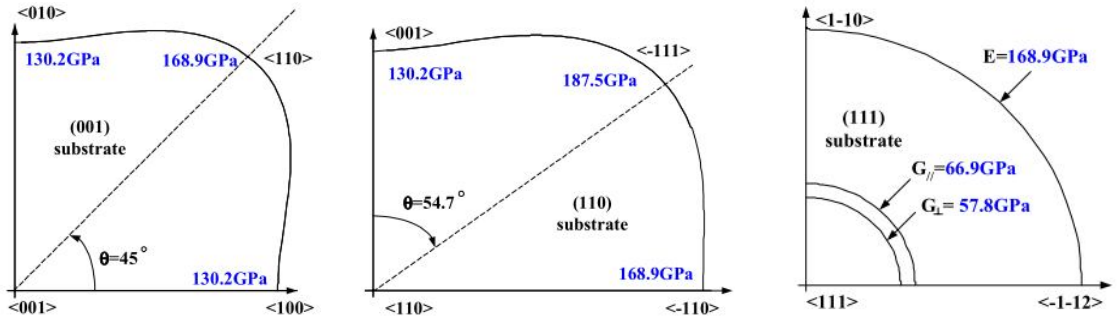

Figure 50: Young's modulus on xy-plane of (100), (110), and (111) Si substrate material, respectively.

However, to integrate annulus gyroscope, (100) orientation is preferable because the N=2 in-plane drive-mode is always aligned to <100> or <110> direction regardless of potential fabrication non-idealities, and M=3 out-of-plane modes still possess near-

isotropic behavior that can be aligned by electrical stiffness applied from sensing electrodes and quadrature electrodes defined on top of annulus mass.

4.4. Dual Pitch-and-Roll Gyroscope

4.4.1. Design and Modeling of Dual-axes Gyroscope

Figure 51 shows the schematic view of the dual-axes annulus gyroscope design. To realize dual-axis rate sensing, the device is designed to utilize an in-plane elliptical drive mode and two orthogonal out-of-plane sense modes (referred to as the x- and y-axis modes, respectively) as shown in Figure 52. The device is actuated from the drive-in side electrode located at <100> direction of substrate, and the in-plane drive output signal is monitored from the drive-out side electrode. For the differential sensing of output signal, four sense electrodes ($\Omega_x^{+,-}$ and $\Omega_y^{+,-}$) are defined on top of anti-nodes of out-of-plane modes. A polarization voltage required to excite the drive mode and sense Coriolis-force induced current output signal is directly applied on top of central pad. In addition, three pairs of tuning electrodes are employed to mode-match three resonance peaks using electrostatic frequency tuning. The dimension of annulus gyroscope is 800µm wide and 40µm thick.

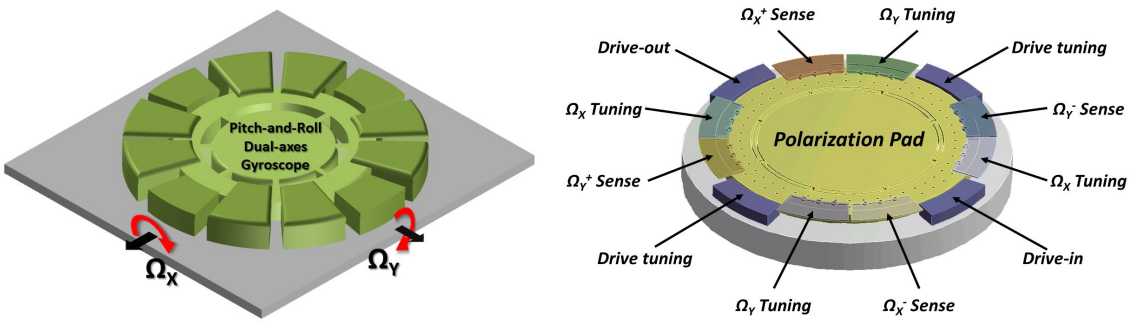

Figure 51: Overview and sensing axes of pitch-and-roll gyroscope (left) and schematic view of dual-axes gyroscope.

An ANSYS simulation of gyroscope operation is illustrated in Figure 52. The in-plane drive mode (Figure 52, top) has anti-nodes aligned with the x- and y-axes. Applied pitch-and-roll rotation causes out-of-plane coupling, generating differential output currents through the capacitive gap change at the top sense electrodes (Figure 52, bottom). Since the degenerative behavior of secondary elliptical out-of-plane sense modes makes anti-nodes of the x-axis mode aligned to nodes of the y-axis mode and vice versa (Figure 52, bottom), cross-axis sensitivity is expected to be inherently small.

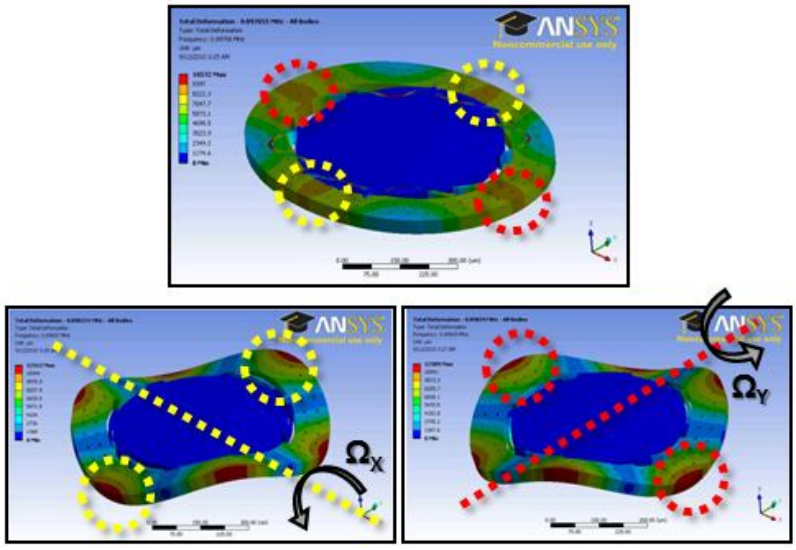

Figure 52: Electrostatically tuned ANSYS simulation model. In-plane drive (top), out-of-plane x-axis sense (bottom-left), and out-of-plane y-axis resonance modes are shown. Electrodes are hidden for the clarity of mode shapes.

The frequencies of the in-plane drive and out-of-plane sense modes are designed to match at a specific device dimension. However, in order to address variations in the thickness of the SOI wafer along with the inevitable process variations caused by fabrication imperfection and its subsequent initial frequency split, out-of-plane and in-plane frequency tuning electrodes are selectively-defined during the fabrication process.

Two drive tuning electrodes located at the anti-nodes of the in-plane drive mode tune the drive mode frequency with minimal effect on the out-of-plane sense mode frequencies. For the out-of-plane sense mode tuning, a total of four Ω_x and Ω_y tuning electrodes are arranged 90˚ apart to exert balanced electrostatic force.

4.4.1.1. Process Variations and Tuning Behavior

To tune each resonance mode with minimal interference from other resonance modes, different capacitive air gaps are designated according to the purpose of each electrode. The top electrodes used for x- and y-axis rate sensing and tuning have narrow vertical gaps of 300nm with respect to the vibrating mass but retain wide lateral gap sizes of ~5µm against the vibrating structure. The side electrodes are dedicated for drive mode tuning and device actuation and use only narrow 200nm lateral gaps (Figure 53). The number, width, spanned angle, and gap size of the tuning electrodes are optimized to achieve ~12kHz tunability to compensate ±0.3µm thickness variation with less than 10V DC voltage. In addition, the selectively-defined electrode configuration of the sense electrodes reduces the in-plane drive mode quadrature component seen at the out-of-plane sensing electronics.

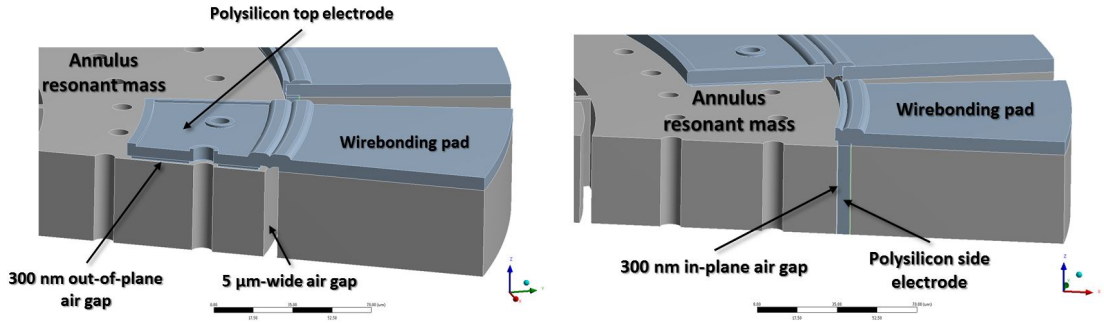

Figure 53: Cross-section of top (left) and side (right) electrodes from simulation model.

In order to predict drive and sense mode frequency shift under process variation, ANSYS simulations are performed using a process-biased model. Simulations of the frequency difference between out-of-plane sense modes and in-plane drive mode reveal +2.15kHz/0.1μm thickness variance and -5.33kHz/0.1μm lateral dimension variance (Figure 54 (left)). Even though substrate thickness variation can be offset by giving lateral bias as shown in the plot, having a large electrostatic tuning is desirable for improving the manufacturing yield. The sense-mode tuning behavior is shown in Figure 54 (right). The employed electrostatic tuning can compensate ±0.3μm of thickness variation of SOI substrate.

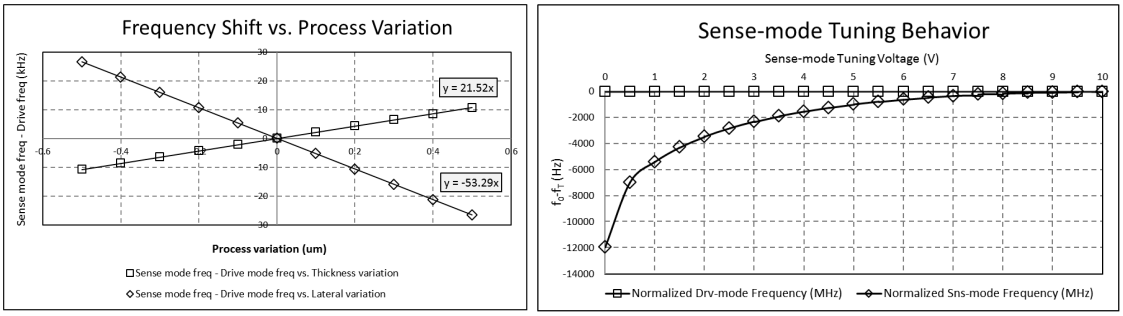

Figure 54: ANSYS Workbench™ simulation of process variation and frequency shift using process-biased model (left) and sense-mode tuning behavior (right).

4.4.1.2. Determination of Operating Frequency, Q-factors, and mechanical bandwidth

Among the numerous factors to be considered at the design stage, the first step of the design work is performed by determining the mode-matched operating frequency. The operating frequency of the device is obtained based on the targeted sensor size. Since the annulus gyroscope employs in- and out-of-plane resonance modes, thickness and lateral dimension of the annulus resonant mass determines the operating frequency. In

this work, the thickness of the substrate is chosen based on the commercially available SOI wafer and its thickness variation in mass-production condition (Figure 55) [75] and the processibility of the substrate utilizing deep reactive ion etching (DRIE) tool available. Lateral dimension of the device, i.e. outer-diameter of the annulus resonant mass, is determined by the desired foot-print of the sensor.

Q-factor of the device determines motional impedance of the system, noise performance, and scale factor. Although all the aforementioned performance parameters indicate boosting up the mechanical Q-factor improves overall system performance, excessive Q-factor will narrow sensor's mechanical bandwidth hence reduce the response time of the resonant sensor. The designed bandwidth is set between 50 to 100 Hz of operational bandwidth to enable rapid motion sensing.

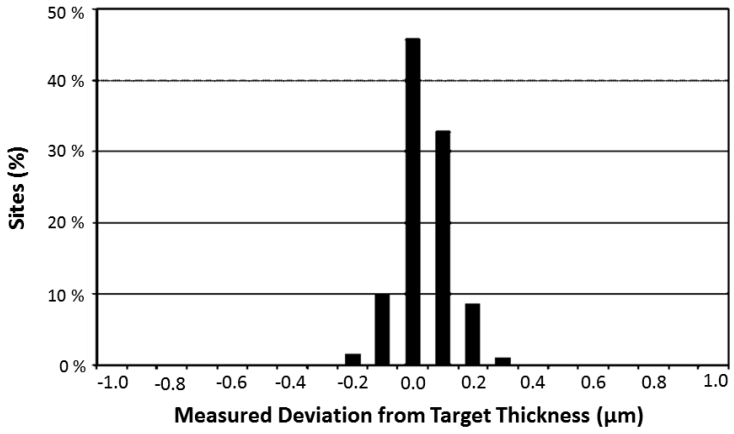

Figure 55: Example of thickness variation from commercially available SOI substrates.

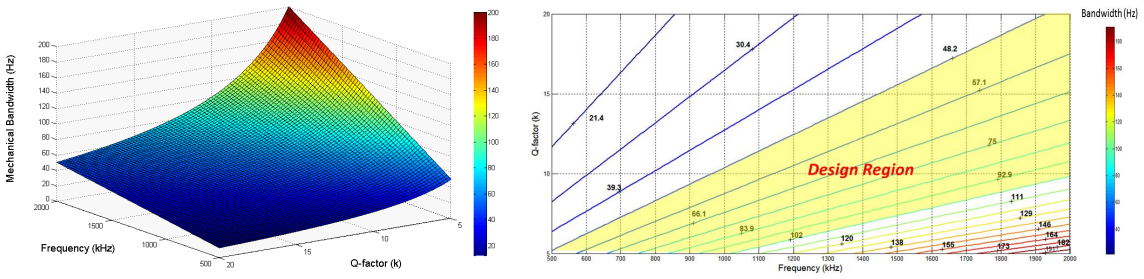

Figure 56: Mechanical bandwidth of the annulus gyroscope with respect to the operating frequency and Q-factor. The curved surface demonstrates the quantity of mechanical bandwidth (left). The contour plot is derived to designate design region (right).

4.4.1.3. Design and Determination of Capacitive Side Air Gap Size

The vibration amplitude of the annulus mass at peak resonance frequency determines two key performance parameters, scale factor and mechanical noise level. The larger vibration amplitude is interpreted as higher linear velocity existing in the drive-mode, and Coriolis-force induced sense-mode deflection is directly proportional to the drive-mode amplitude. Because of the acoustic energy stored in resonant mass makes the system more immune to the random collision from surrounding air molecules, mechanical noise level benefits from the larger driving amplitude as well. However, in capacitive devices, motional impedance is proportional to 4^{th} power of nominal capacitive gap size (d_0), and the tunability is proportional to $1/d_0^3$. Therefore, d_0 cannot be increased for the operation of the device.

Figure 57 shows performance parameters related to the capacitive side air gap. The design region for side air gap size is determined to make motional impedance below 40kΩ for closed-loop operation of the annulus gyroscope at drive mode, mechanical noise level ~0.02 dps/√Hz, and sensitivity higher than 50pm/dps to create 50pA/dps of

current output from one sense electrode. All the plots are generated with Q-factor of 10k and V_P of 10 V DC.

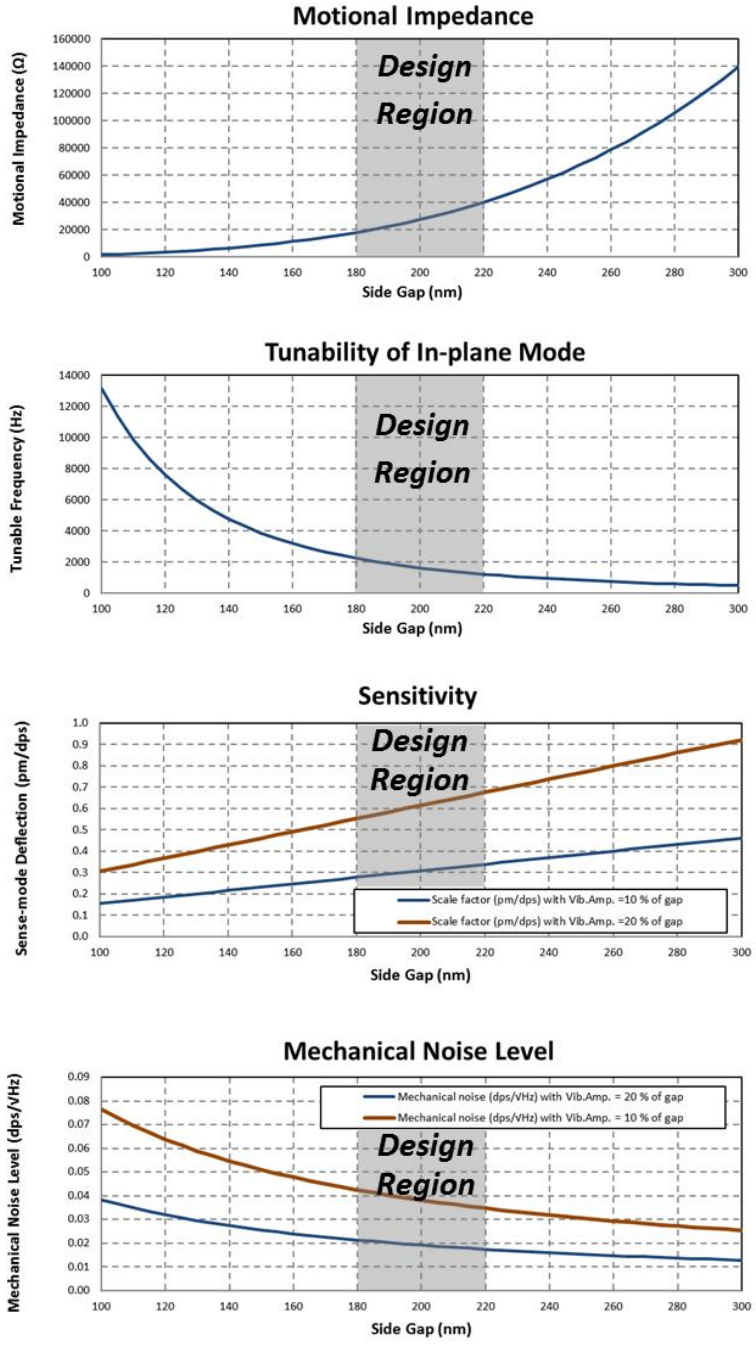

Figure 57: Design region of capacitive side air gap.

4.4.1.4. Design and Determination of Capacitive Top Air Gap Size

Because Coriolis-force induced deflection of the annulus gyroscope exists toward out-of-plane direction, the top electrodes which have an overlapped region above the annulus resonant object are introduced to sense Coriolis output signals. In capacitive resonant devices, the output current is inversely proportional to the square of nominal gap dimension ($d_{0,top}^2$), and the corresponding out-of-plane sense modes exhibit frequency tunabilities proportional to $1/d_{0,top}^3$ which should cover process variation of employed SOI substrate. On the other hand, since the resonant mass is connected to a fixed DC potential at V_P, sensing electrodes are tied to mid-rail of power supply of interface ASIC, and sense-mode tuning electrodes have varying potential between 0 to V_P, an electrostatic force is exerted through the capacitive gap and pulls the resonant mass toward the sensing plates causing pull-in failure of the gyroscope system. The pull-in voltage is proportional to $1/d_{0,top}^{1.5}$. Considering the aforementioned design parameters that determine out-of-plane air gap size, the optimal design point should be defined to operate the annulus gyroscope.

Figure 58 shows the design region and related performance parameters considered at the design stage. The sensor is designed to produce an output current above 50pA/dps/electrode with drive-mode amplitude at 20% of nominal side gap (Figure 58, top). In addition, the frequency tunability (Figure 58, middle) is set to compensate thickness variation of SOI substrate in ±0.3 μm range (Figure 54) that is commercially available in the market. While satisfying desired sensitivity and tunability of the device, the top gap size is determined not to cause pull-in failure during the operation (Figure 58, bottom).

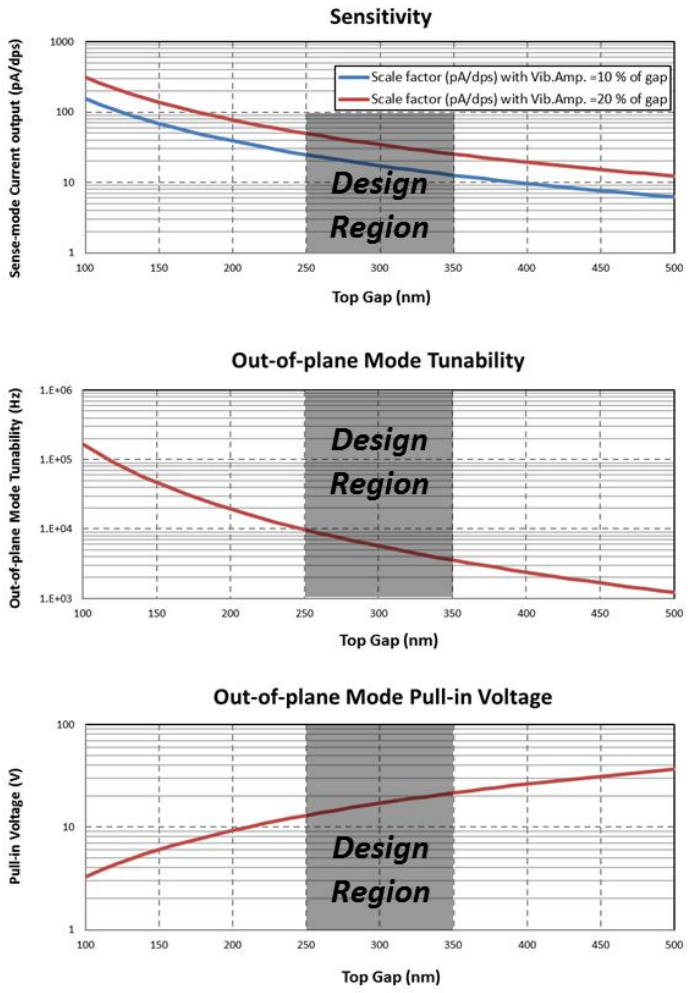

Figure 58: Design region of capacitive top air gap.

4.4.1.5. Mode-matching Condition Simulated by ANSYS Workbench™.

ANSYS Workbench™ simulations are performed to show frequency response from the annulus gyroscope. The drive and sense-modes are electrostatically tuned in the simulation environment using DC tuning voltages, then the harmonics response is graphically plotted to demonstrate the frequency split under mode-matched condition.

As shown in Figure 59, the mode-matching in the simulation is performed to exhibit the equal Δf between drive- and x-modes, and drive- and y-modes. Under the

given condition with same Q-factors in x- and y-modes, the scale-factor from each axis should behave identically.

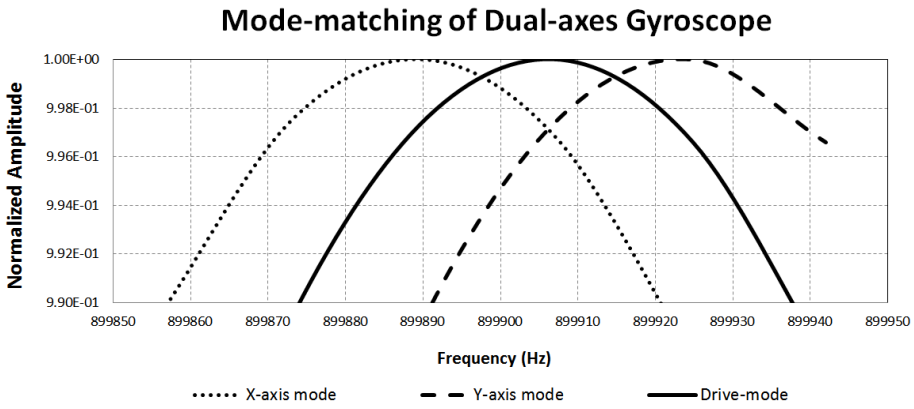

Figure 59: Harmonics response of annulus gyroscope simulated by ANSYS Workbench™.

4.4.1.6. Acceleration Immunity

Given the fact that gyroscope has to resolve applied rotation rate without cross-sensitivity from linear acceleration, the design of the gyroscope to efficiently reject the acceleration-induced output signal is taken into account. The resonance modes that translate and respond to the applied acceleration are designed to be at ~200kHz toward out-of-plane direction and ~450kHz toward in-plane direction. The stiffness of the modes makes the sensor resist against to the linear-acceleration applied to the system. In addition, differential sensing scheme is considered to be used at the sensing electronics.

Figure 60 shows the resonance modes that respond to the linear acceleration. The stiff mechanical structure can effectively reject acceleration-induced response. Differential sensing scheme further reduces the output signals compared to single-ended sensing scheme (Figure 61).

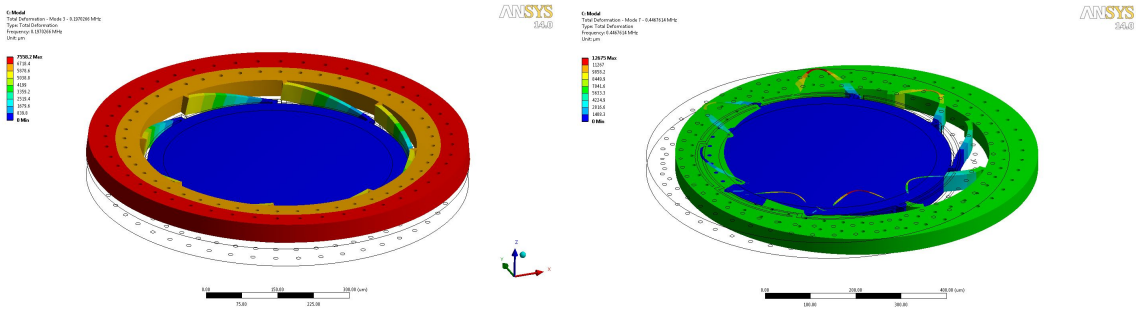

Figure 60: Resonance modes respond to linear acceleration.

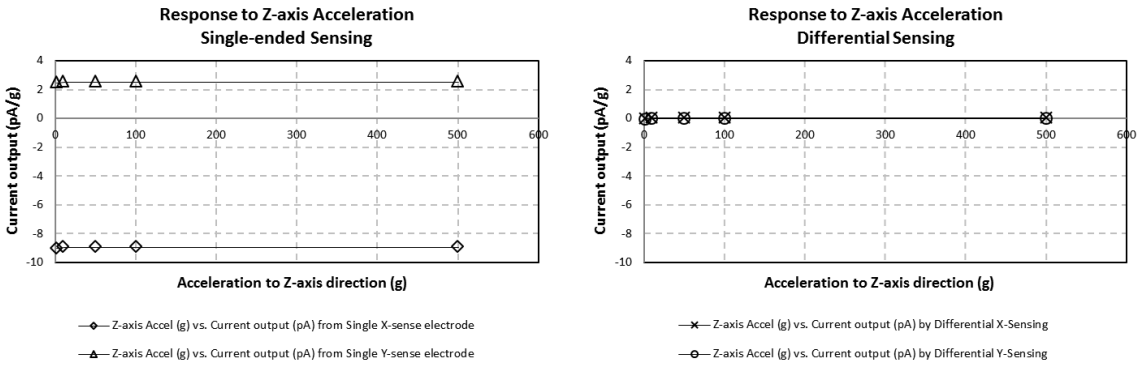

Figure 61: Simulated acceleration sensitivity with single-ended sensing (left) and differential sensing (right) scheme.

4.4.2. Fabrication Process Flow

A modified version of high-aspect-ratio combined polysilicon-and-silicon process (HARPSS^{TM}) is adopted as a fabrication platform named HARPSS^{TM} ver.4. The benefit from the revised version of process flow is its flexibility in creating in- and out-of-plane sub-micron gaps, i.e. the process step that creates out-of-plane gap is independent from the process step that determines in-plane gap size. In addition, the revised process platform inherits the advantages of HARPSS^{TM} process which is represented by achieving the high aspect ratio capacitive air gap over 1:100 without using expensive lithography.

The HARPSS^{TM} ver.4 process flow is outlined in Figure 62. The process starts from creating and patterning initial 41μm-thick thermal oxide layer on a 41μm-thick (100) silicon-on-Insulator substrate (Figure 62 (a)). The device layer is etched through using the thermal oxide mask (Figure 62 (b)), and 200nm LPCVD sacrificial oxide (SACOX) layer is deposited. The 1st polysilicon layer is then deposited after boron doping and etched back from the surface (Figure 62 (c)). The trench-refilled 1st polysilicon is etched out from the area where the top electrodes are supposed to be defined (Figure 62 (e)). 3μm-thick LPCVD oxide is deposited to refill the empty trenches and holes then patterned (Figure 62 (f)). 300nm-thick 2nd LPCVD SACOX is then deposited and patterned to create a vertical capacitive air gap (Figure 62 (g)). The 2nd polysilicon is deposited, boron-doped, annealed and patterned to finalize the structure (Figure 62 (h)). The batch is finished by release in HF with timed control (Figure 62 (i)).

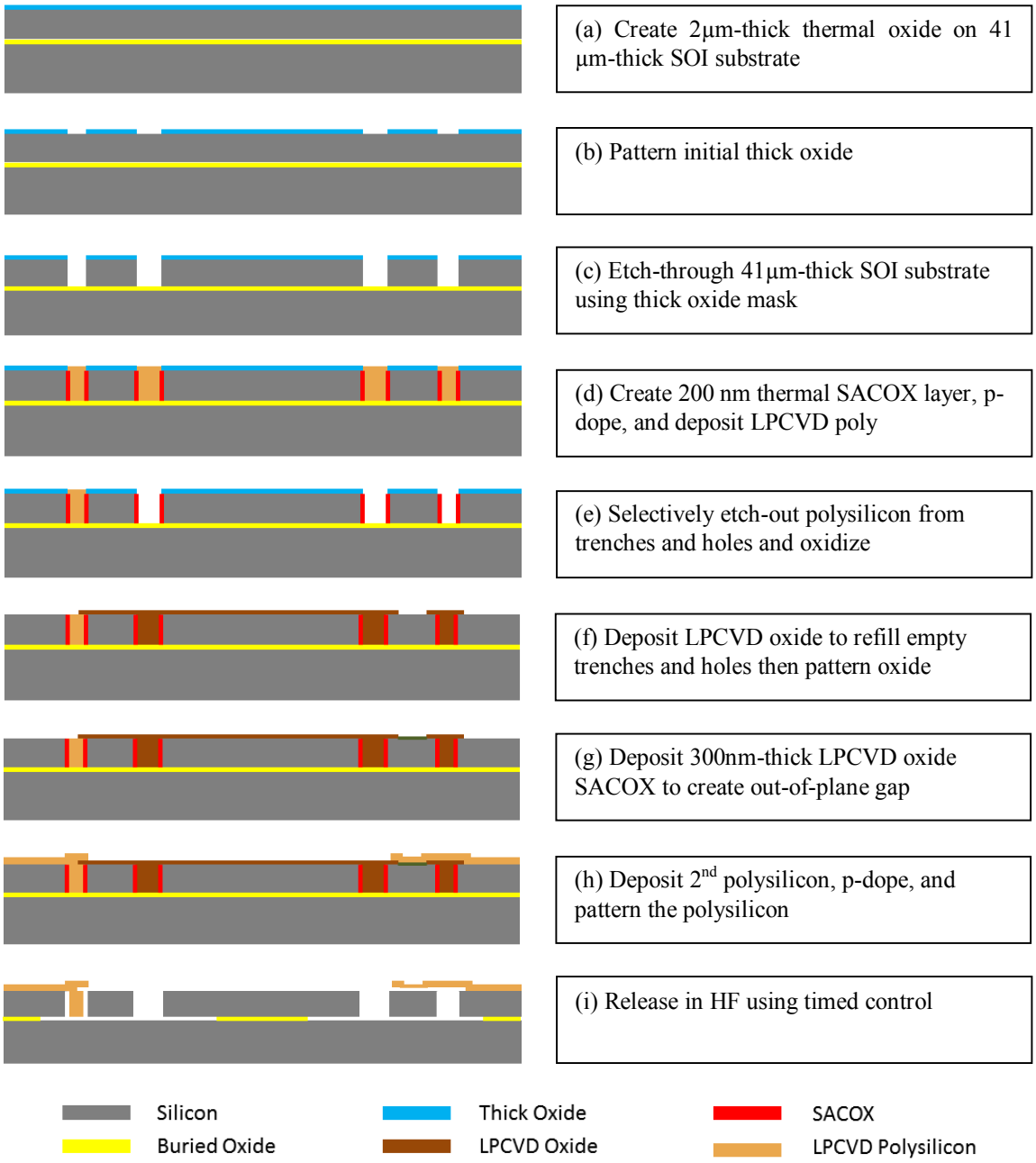

Figure 62: Process flow of HARPSS™ ver.4.

Several SEM pictures are taken to illustrate the critical steps during the fabrication process. Figure 63 shows the process steps pictorialized in Figure 62(d) and (e). The voids in polysilicon can possibly exist after LPCVD polysilicon deposition, but the void is not exposed at the top surface (Figure 63 (left)). Figure 63 (right) shows a

device after Figure 62 (e). Polysilicon which refilled holes and trenches are cleanly etched out from the unwanted area.

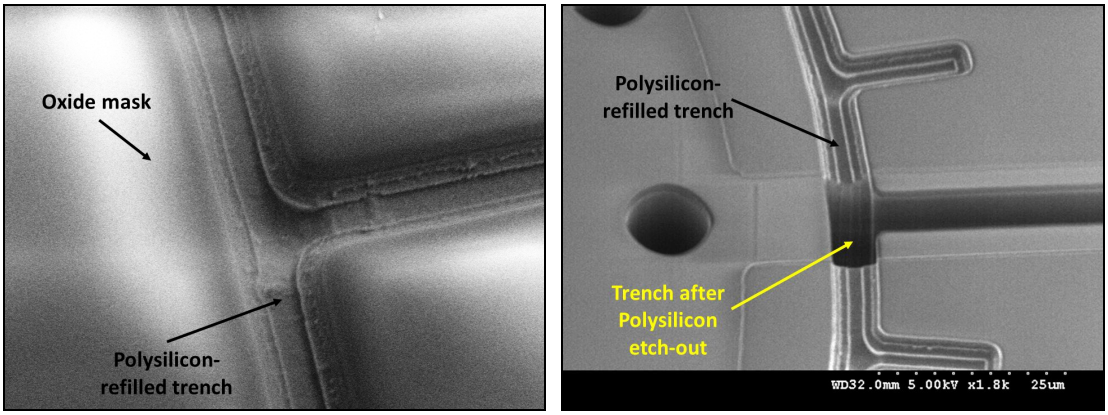

Figure 63: Polysilicon-refilled trench after 1st LPCVD polysilicon etch-back (left) and after 1st LPCVD polysilicon etch-out from trench and holes.

SEM views of the annulus gyroscope are shown in Figure 64. The side electrodes used for drive-mode excitation and tuning have a narrow (200nm) lateral capacitive air gap while top electrodes used for sensing and sense mode tuning bridge over the 5µm wide trench openings and have 300nm vertical transduction gap sizes that can be different from their lateral gaps. The overall device structure is targeted to exhibit wide frequency tunability with low cross-mode tuning, minimal quadrature signal and quadrature component, and efficient Coriolis-force induced signal transduction through sub-micron capacitive air gaps which will be verified in the characterization part.

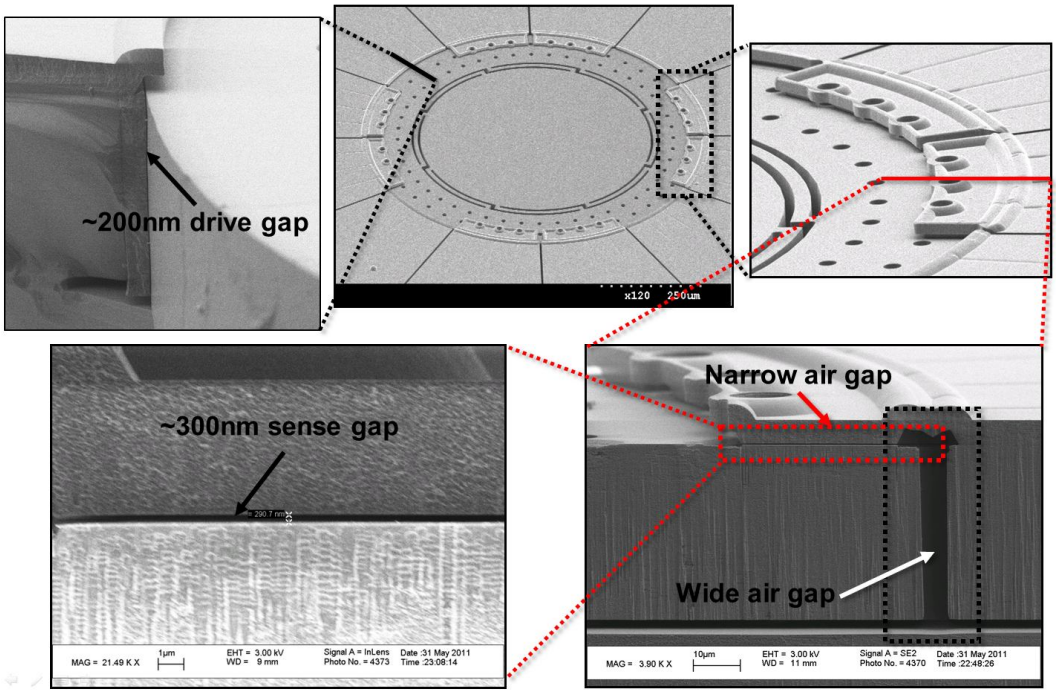

Figure 64: Fabricated annulus gyroscope. Cross-sections of side and top electrodes are shown.

Along with the dual-axes gyroscope explained in this dissertation, the process platform can produce several other types of inertial sensors, yaw gyroscope, tri-axial gyroscope, tri-axial accelerometers, and magnetometers.

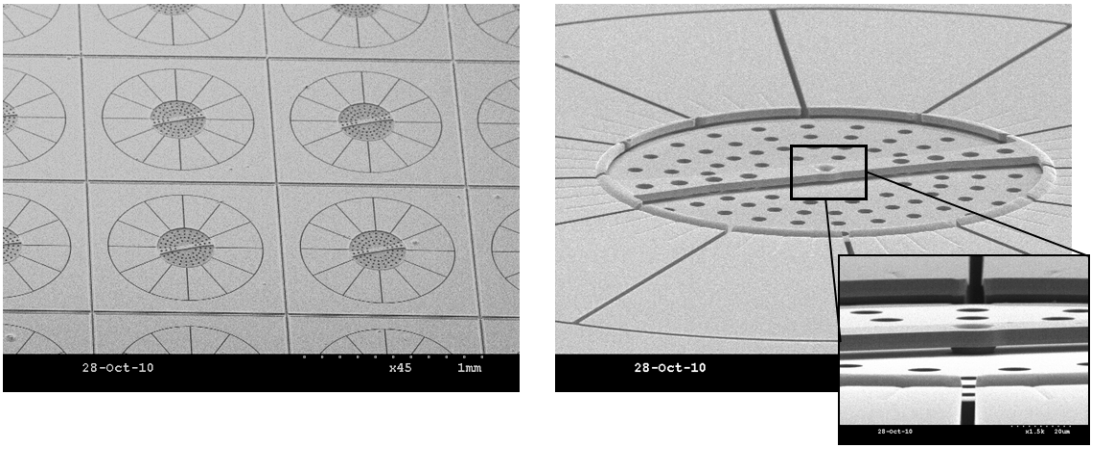

Figure 65: Yaw gyroscopes co-fabricated with pitch-and-roll gyroscopes. Inset shows polysilicon-trace structure which anchors top of resonant disk gyroscope.

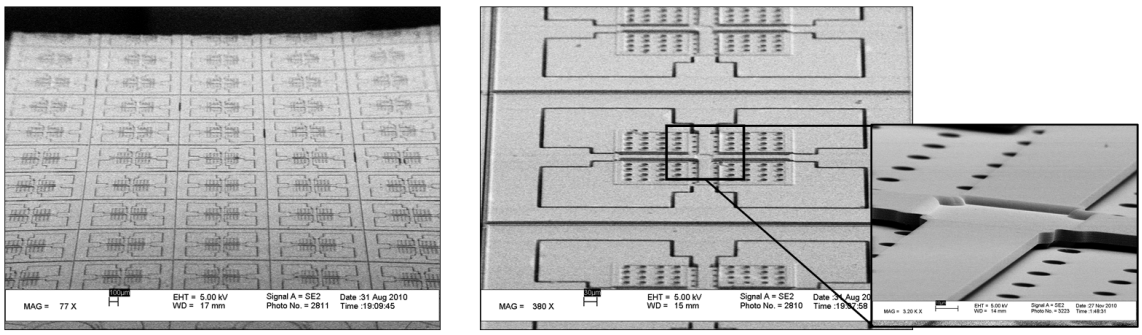

Figure 66: Tri-axial accelerometers co-fabricated with pitch-and-roll gyroscopes. Inset shows polysilicon tether that sustains proof-mass of accelerometer [76].

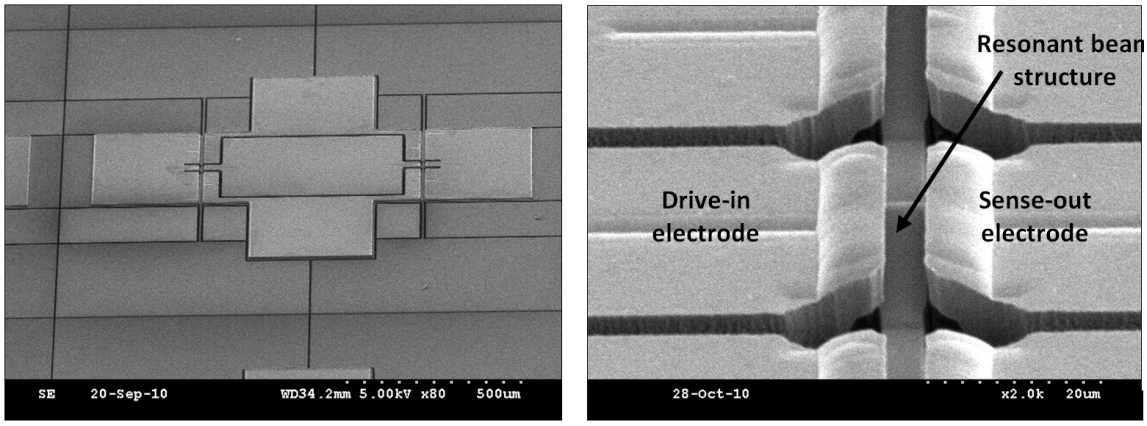

Figure 67: Co-fabricated resonant magnetometer (left). Zoom-in picture of a narrow beam resonant structure between drive-in and sense-out electrodes is shown (right)

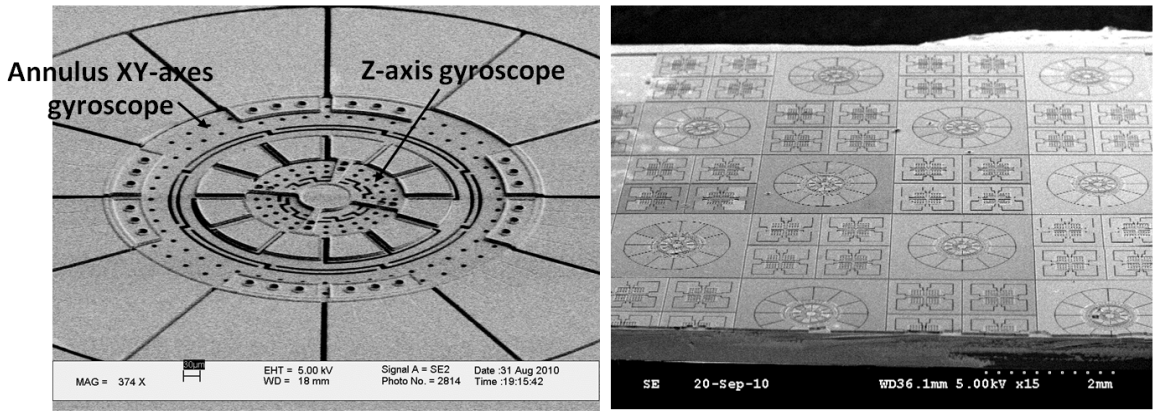

Figure 68: Prototype of a tri-axial gyroscope (left). Yaw gyroscope is plugged into the center of a pitch-and-roll gyroscope. Batch-processed IMU devices (right). Tri-axial gyroscopes and tri-axial accelerometers are co-fabricated via HARPSS^{TM} ver.4 fabrication platform.

4.4.3. Characterization of Dual-axes Gyroscope

4.4.3.1. Frequency Tunability of Dual-axes Gyroscope

Figure 69 shows the measured frequency tunability of drive-mode using applied DC voltages up to 20V. The drive-mode and one of out-of-plane sense-modes frequencies are shifted by 5,825 Hz and 4,273 Hz, respectively, by using two tuning electrodes per each mode. During the tuning procedure, amplitudes of the output signals represented by insertion loss (I.L.) behave unaffected which indicate the resonant mass is maintaining balanced location from the surrounding electrodes, and capacitive gap sizes exert electrostatic force as designed. Both in- and out-of-plane tuning behaviors exhibit large tunability with little cross-mode tuning.

Frequency tuning using DC polarization voltage is measured and plotted in Figure 70. Above 14kHz of drive-mode frequency is down-shifted with respect to the out-of-plane sense modes using V_P up to 28 V DC (Figure 70, left). During the tuning procedure using V_P, the potentials of drive- and sense-modes tuning electrodes are fixed at ground voltage to maximize the effect of electrostatic spring softening at the corresponding resonance modes. The tuned frequency verifies mode-matched operation comparable to ±0.3μm thickness variation of substrate as shown in Figure 54. The mode-matching of three resonance peaks is accomplished at V_P of 14.7 V DC (Figure 70, right).

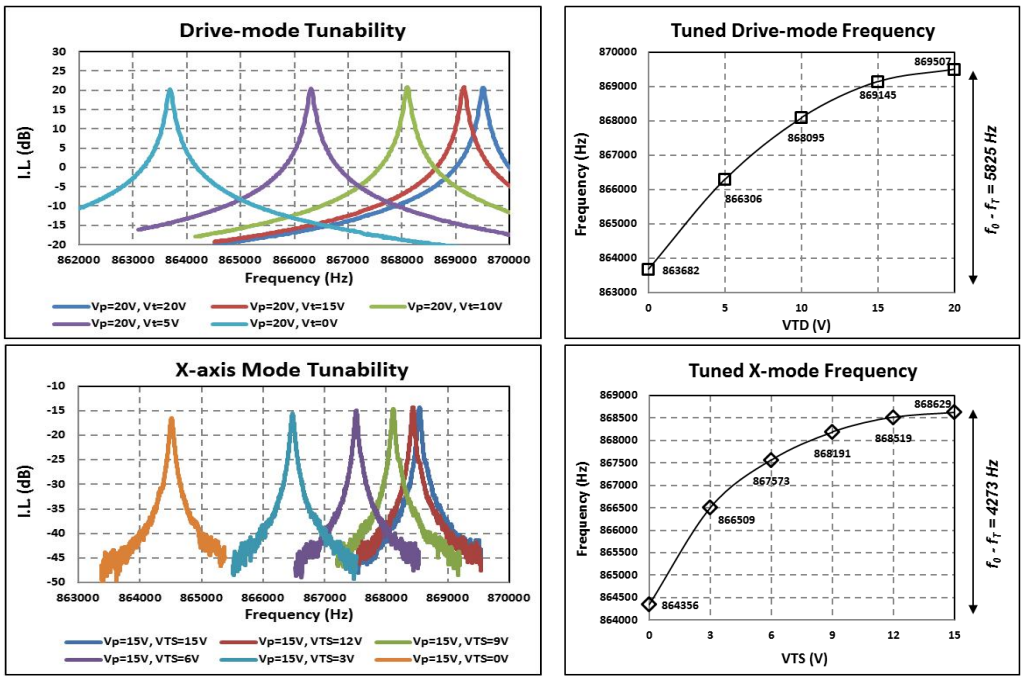

Figure 69: Frequency tuning behavior of dual-axes gyroscope.

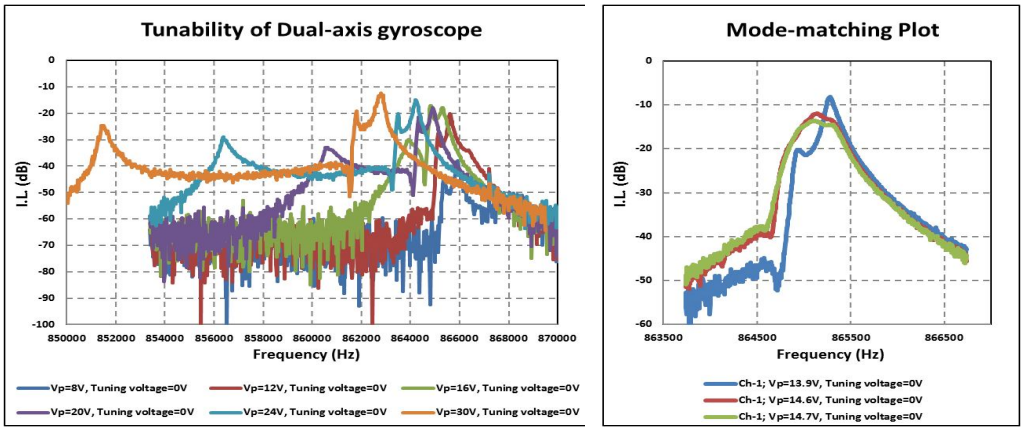

Figure 70: Mode-matching of three resonance modes of dual-axes gyroscope.

4.4.3.2. Frequency Response of Dual-axes Gyroscope

Along with the independent large frequency tunability of resonance modes, the selectively defined gap sizes result in significant signal strength differences between the side and top electrodes with the given in- and out-of-plane motion of the vibrating mass.

Two different cases of device actuation and signal readout are measured and plotted in Figure 71. When signal is driven from Drive-in side electrode, signal observed from Sense top electrode exhibits more than 10dB lower signal than from drive-out side electrode (Figure 71, top). A similar response is shown when the device is actuated from Ω_x^+-sensing top electrode and readout from the side and top electrodes simultaneously (Figure 71, bottom).

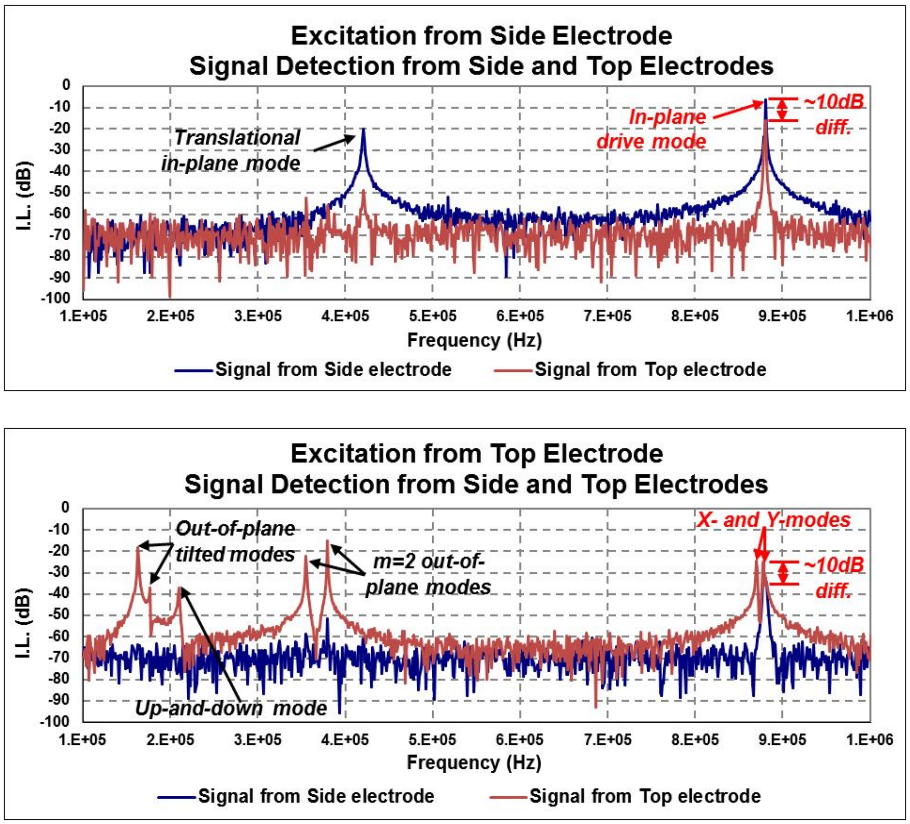

Figure 71: Frequency response from dual-axes gyroscope. Corresponding resonance modes are detected depending on excitation orientations.

The Q-factors for the drive, x- and y-axis modes are measured to be 9.7k, 13k and 10k under split-mode conditions, respectively, in high vacuum (Figure 72). In order to verify high-Q behavior of the device, Q-factors and frequency responses are measured in

vacuum pressure varied from 0.1μBar to 1mBar. The Q-factor changes of 7.2%, 16.5%, and 15.12% for the drive, x-axis mode, and y-axis mode, respectively, are observed (Figure 73).

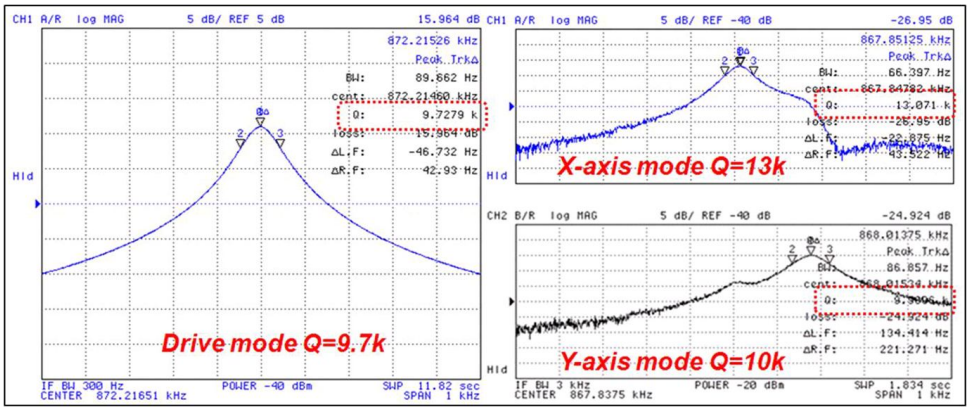

Figure 72: Measured Q-factors for drive, x- and y-modes with split-mode condition.

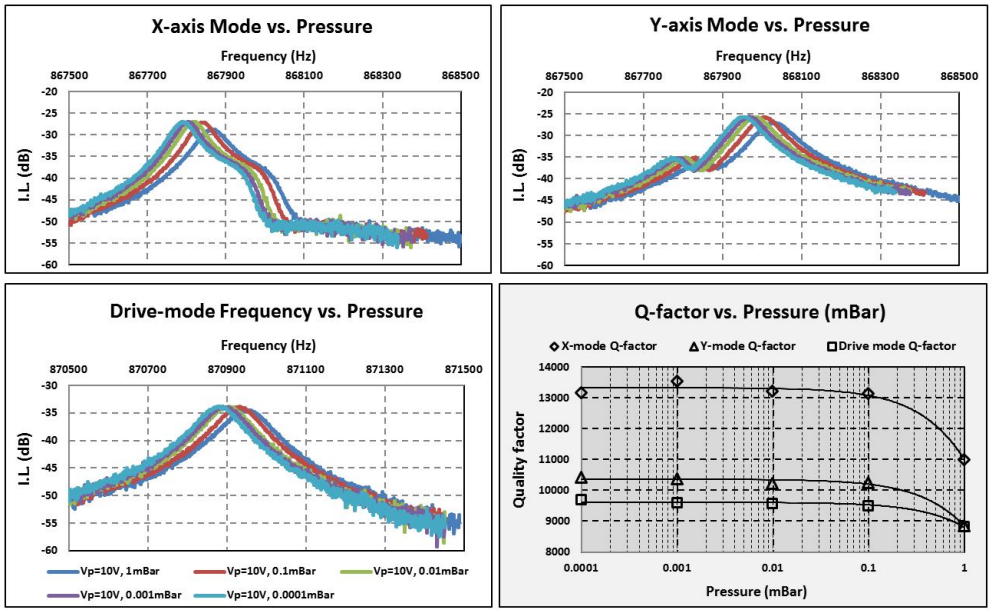

Figure 73: Q-factor vs. vacuum level.

Scale factors for x- and y-axis rotation rate are measured to be 127.4μV/deg/sec/electrode and 213.8μV/deg/sec/electrode with cross-axis sensitivity of

25.2% and 20.1%, respectively (Figure 74). The cross-axis sensitivity can be reduced by employing quadrature cancellation electrodes to align the anti-nodes of sense modes to drive mode or splitting one of sense-modes to prevent Coriolis-response from transferring to the mode-split sense-mode.

Allan variance bias instability (AVAR) measurements report bias drift of 0.18deg/sec and 0.30deg/sec for x- and y-axis mode, respectively (Figure 75).

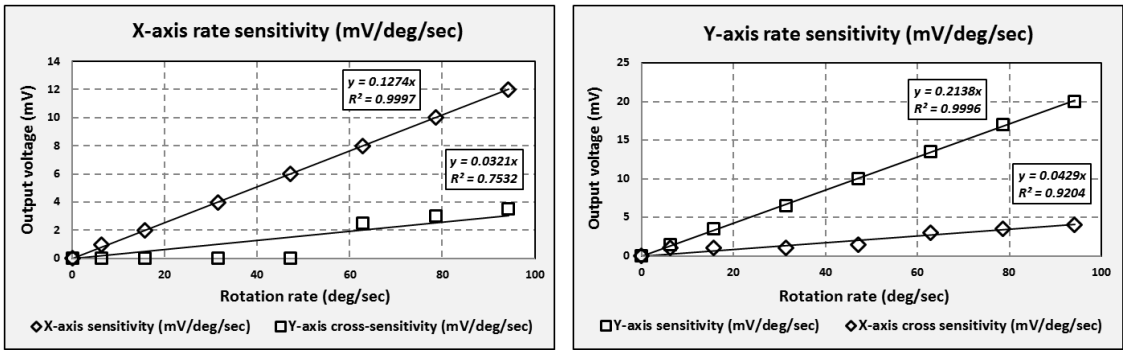

Figure 74: Rate sensitivity of dual-axes gyroscope.

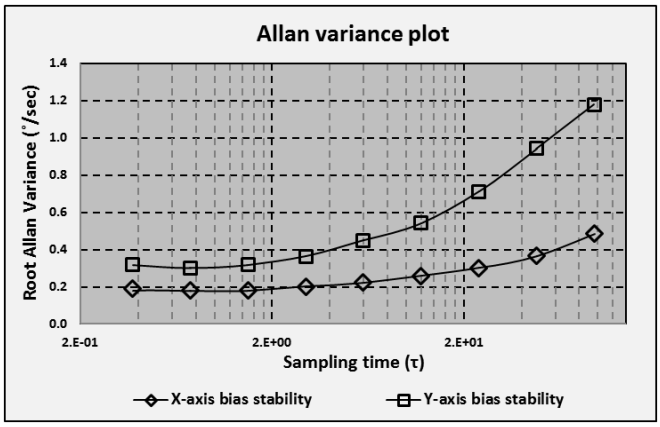

Figure 75: Measured AVAR plot from dual-axes gyroscope.

4.4.3.4. Discussions on Single Proof-mass Dual-axes Gyroscope

The dual-axes gyroscope using three resonance modes matched at an identical frequency can measure input rotation rate from two orthogonal lateral axes, pitch-and-roll. The employed modes of operation, high-Q behavior, and wide electrical frequency tunability can satisfy the demands of tri-axial gyroscope required for the consumer grades applications. In addition, design optimizations of the physical dimension of the sensor, fabrication facility, and targeted performance is successfully fulfilled.

The batch-processibility of the modified HARPSS^{TM} ver.4 process platform is proven to yield tri-axial accelerometers and resonant magnetometers for six or nine degree-of-freedom inertial navigation sensor integration. In addition, the process flow obviates vertical assembly process of inertial sensors to detect angular rotation rate from multi-axes. Hence, angular offset that can cause cross-axis sensitivity followed by post-fabrication calibration sequence is fundamentally eliminated.

Temperature and pressure dependency of the device exhibit promising reliability over the wide range of operational environment with inexpensive packaging costs. Furthermore, wide frequency tunability proves the mode-matching of the resonant frequencies is guaranteed under the thickness and lateral dimension variations that can possible pose yield issues.

4.5. Pitch/Roll Rate Gyroscope

4.5.1. Introduction

The design, fabrication, and characterization of single-proof mass dual-axes gyroscope was explained in Chapter 4.4. However, the high cross-axis sensitivity was an issue in the application requirements. The possible solution to reduce the cross-axis

sensitivity was suggested to include quadrature-cancellation electrodes to align the anti-nodes of the out-of-plane sense-modes toward sensing electrodes. However, the additional quadrature electrodes necessitate extra area that will increase the die size. In addition, electrical post-calibration still remains as a required effort that involves time-consuming sequence in the characterization of individual sensors.

In this chapter, single lateral-axis sensing high frequency gyroscope for pitch/roll detection is investigated. Instead of mode-matching three resonance modes, i.e. an in-plane drive mode and two out-of-plane sense modes, the sensor will employ a mode-matching between the in-plane drive mode and an out-of-plane sensing mode. The dual-axes sensing can be done by co-fabricating the same sensor with 90° spatial offset as shown in Figure 76.

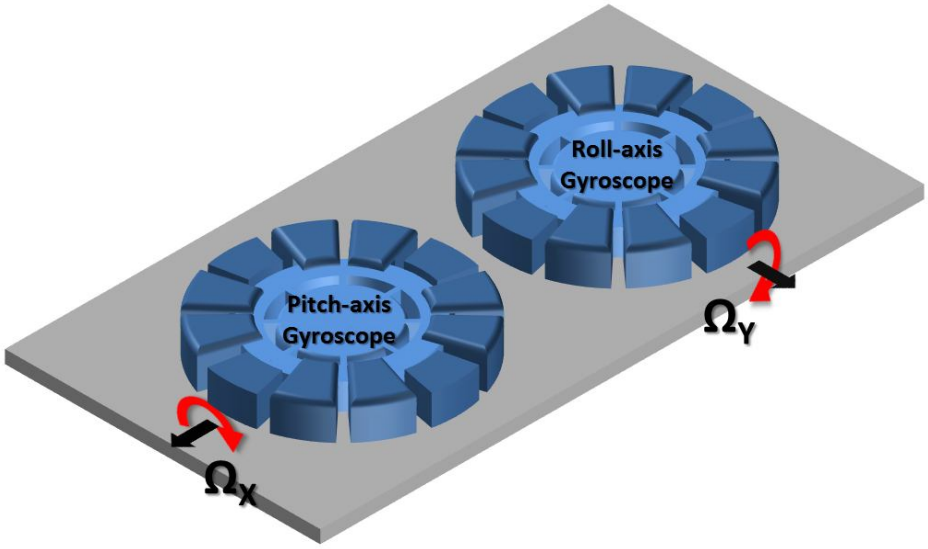

Figure 76: Schematic view of dual-axes annulus gyroscope and pitch/roll gyroscopes in a planar configuration.

4.5.2. Design and Modeling of Pitch/Roll Gyroscope

4.5.2.1. Operating Principle

The annulus gyroscope employs an in-plane drive mode and two orthogonal out-of-plane sense modes for pitch/roll rate sensing. When the primary elliptical in-plane drive mode is generated to create a finite linear velocity in the resonant mass, Coriolis force transfers the in-plane mode's resonant energy toward out-of-plane direction causing a deflection towards Z-axis under mode-matched condition. However, the Coriolis force is not transferred to the out-of-plane sense mode under mode-split condition. The mode-matching and mode-split conditions applied to the out-of-plane modes make the sensor responds to the desired axis of rotation with zero cross-axis sensitivity.

The patterned top electrodes are used to sense the amount of rotation rate through differential capacitive gap changes. To prevent cross-axis sensitivity, the unwanted secondary out-of-plane sense mode is intentionally detuned from the mode-matched resonance modes thus Coriolis-force induced response is transferred only to the out-of-plane mode that is mode-matched with the in-plane drive mode.

Figure 77 shows the schematic of the annulus gyroscope used for pitch rotation rate sensing. The device has four side electrodes for device excitation and drive mode tuning, and eight top electrodes for rotation-rate sensing and tuning/detuning of out-of-plane sense modes. Polarization voltage (V_P) is applied at the center of proof mass through a vertical feedthrough defined during wafer-level packaging (WLP) process. The center of resonant mass and electrodes are rigidly fixed at the bottom by remaining buried oxide layer after release process. The roll rotation sensing can be done by arranging the electrodes spatially off by 90° compared to pitch sensing device.

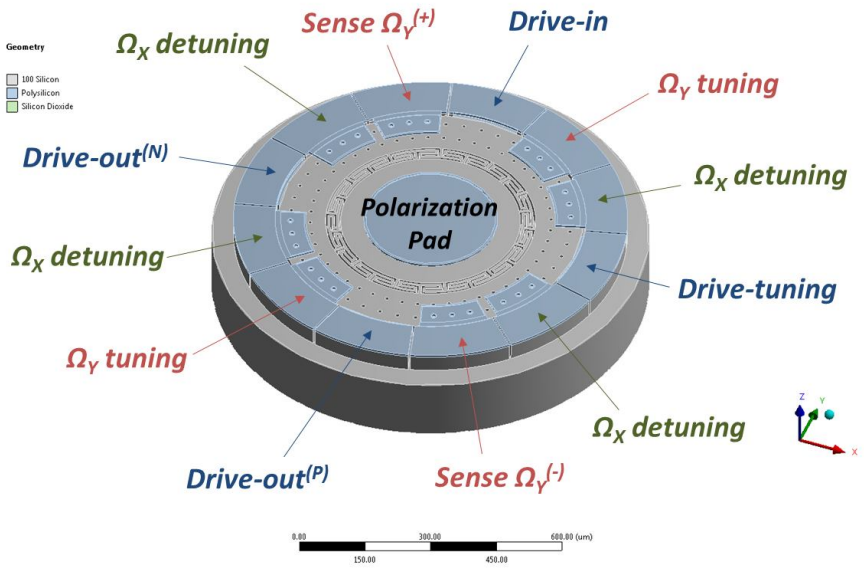

Figure 77: Schematic view of an annulus gyroscope. The unit can sense roll rotation rate without cross-axis sensitivity.

The device is excited from the *Drive-in* side electrode located at <110> orientation of substrate which is, in general, parallel to the primary flat orientation of (100) silicon-on-insulator (SOI) substrate. The driving orientation of single-axis device is parallel to the primary flat direction of the SOI substrate. Therefore, the wafer dicing after wafer level capping process is easily done with minimal orientation error. Then the output current generated by N=2 in-plane elliptical drive mode is monitored from *Drive-out*$^{(P)\ (N)}$ electrodes then fed back into the *Drive-in* electrode for the closed-loop operation with interface IC. The employed differential closed-loop operation of the drive mode prevents the device from locking into wrong in-plane modes such as N=3 in-plane mode and breathing mode. The drive mode is tuned by *Drive-tuning* electrode to down shift the drive-mode frequency in case required. The set of side electrodes related to the drive mode excitation and tuning has 300nm lateral capacitive air gap against the annulus body which only allows lateral signal transduction from the in-plane drive mode. On the

contrary, the sense-modes, which resonate toward out-of-plane direction of the substrate, are detected through top *Sense*$^{(+),(-)}$ electrodes and tuned/detuned by dedicated *Tuning/Detuning* electrodes. The top electrodes have 300nm vertical capacitive air gaps with respect to the annulus mass whereas retaining 5μm-wide lateral air gap which in turn makes the top electrodes sensitive only to out-of-plane deflection induced by Coriolis-force. Consequentially, in- and out-of-plane resonance modes are excited, detected, and tuned via selectively defined side and top electrodes with minimal interferences to each other.

ANSYS Workbench^{TM} harmonic simulation using an electrostatically tuned model is performed to demonstrate frequency response of the device. Q-factor and V_P are assumed to be 20k and 25V, respectively, which are attainable using existing ASIC. Figure 78 shows the mode shapes of annulus gyroscope and its mode-matching condition implemented in the simulation environment. To sense pitch rate sensing, the in-plane drive mode and out-of-plane pitch sensing mode are matched at an identical frequency of 1.2MHz. On the other hand, roll mode is split by 900 Hz from the mode-matched frequencies to eradicate cross-axis sensitivity. The detuned frequency-split corresponds to 15 times of the mechanical bandwidth in sense mode (60 Hz), which ensures cross-axis sensitivity to be insignificant. The electrical frequency trimming procedure is performed by dedicated tuning/detuning electrodes.

Roll sensing can be done by mode-matching the in-plane drive mode and roll sensing mode with detuned pitch sensing mode. The roll device can be easily configured by organizing the electrodes and annulus mass by 90° off from pitch sensing configuration.

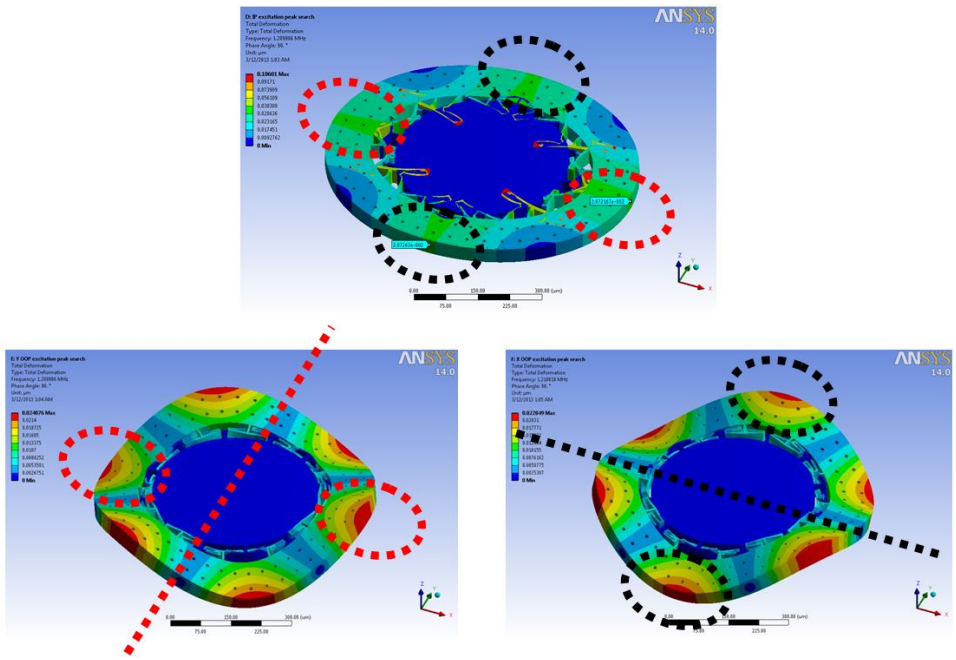

Figure 78: ANSYS Workbench™ harmonic simulation using electrostatically tuned model. Electrodes are hidden for the clarity of mode-shapes.

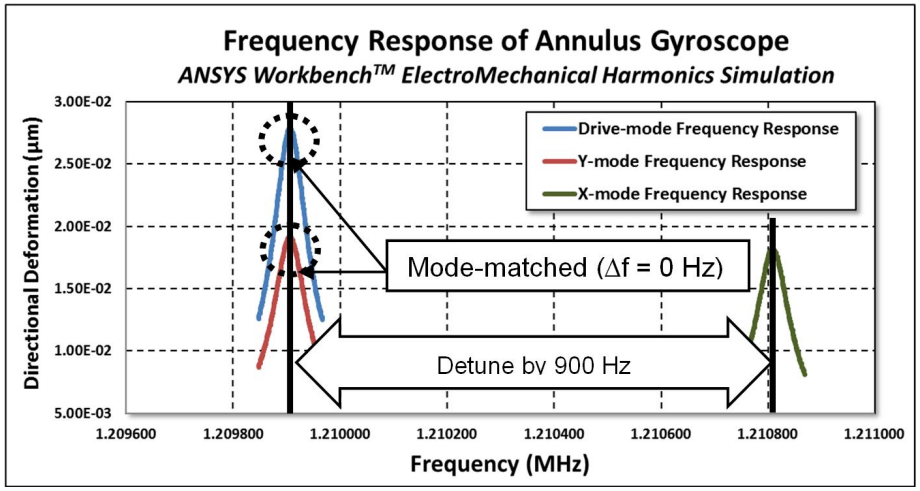

Figure 79: Mode-matching condition exhibited by frequency response from drive mode and x/y-modes.

4.5.2.2. Process Variation, Resonance Frequency Tuning and Detuning

Most of axis-symmetric yaw gyroscopes operate with inherently mode-matched degenerate in-plane resonant modes that can be tuned using low DC voltages when the

modes are split. However, pitch/roll devices necessarily require non-degenerate in- and out-of-plane modes. Therefore, the frequency response is susceptible to the process variations such as thickness deviation of SOI substrate and critical dimension (CD) loss during lithography process. For the manufacturability and stable operation of the device, the gyroscope needs to be designed to ensure sufficient frequency tunability to cover thickness variation of ±0.3μm that ±3σ of commercially available silicon-on-insulator (SOI) substrates reside in. In addition, CD loss of ±0.2μm should be accounted to address the variance in lithography process.

In order to predict drive and sense mode frequency shift under process variation, ANSYS simulations are performed using a process-biased model (Figure 80 (top)). Simulations of the frequency difference between out-of-plane sense modes and in-plane drive mode reveal +0.98kHz/0.1μm thickness variance and -2.78kHz/0.1μm lateral dimension variance. As shown, thickness variation can be offset by giving lateral bias. For example, Δf caused by +0.05μm thicker substrate that raises Δf to +0.49kHz can be counterbalanced by giving -0.15μm of lithography bias that down shifts Δf by -0.49kHz to cancel the process variation. However, having a large electrostatic tuning is desirable for improving the manufacturing yield.

Electrostatic modal simulations show drive and sense mode frequencies can be tuned by 12kHz using up to 28V DC from dedicated tuning/detuning electrodes. In addition, the tuning characteristic exhibits nearly independent frequency tuning with minimal cross-tuning behavior to each mode which results in each mode's frequency tuning without affecting the other modes (Figure 80 (bottom)).

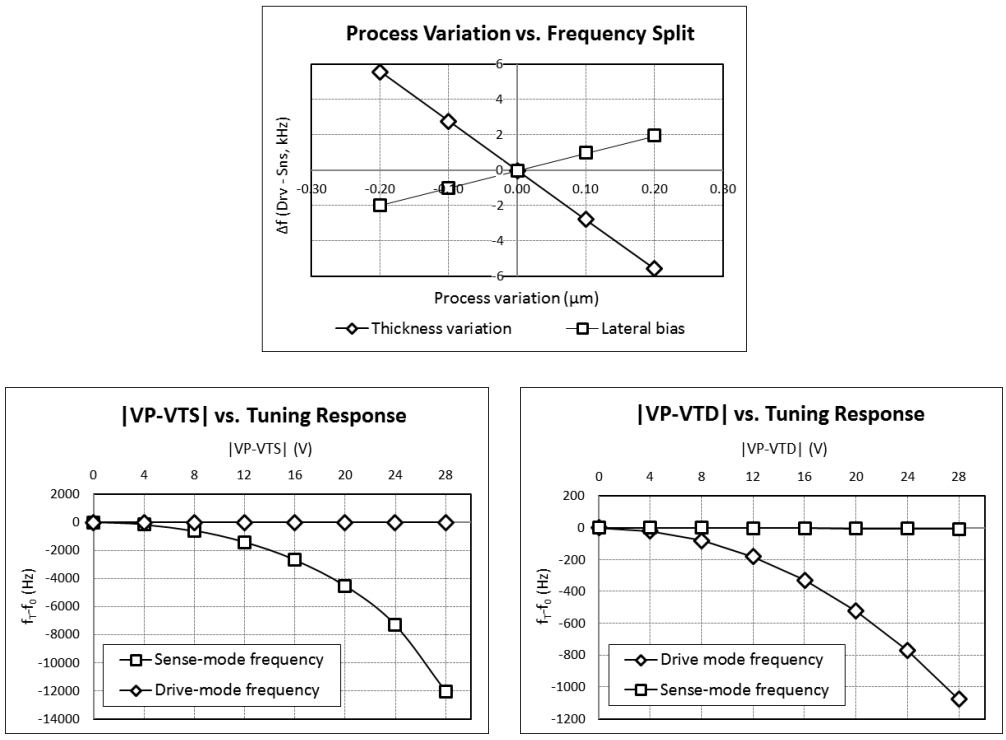

Figure 80: ANSYS Workbench™ simulation of process-tolerance (top), sense-mode tuning behavior (middle), and drive-mode tuning behavior (bottom).

4.5.2.3. Pull-in Behavior of Capacitive Annulus Gyroscope

The incorporated set of electrodes and the shape of annulus body necessarily involve electrostatic forces to in- and out-of-plane directions from side and top electrodes, respectively, that move translates the resonant mass toward the electrode with different potential. The DC pull-in limitation should be carefully investigated in order to avoid failure of the device operation during the tuning/detuning procedure. In addition, driving amplitude in excessive of 1/3 of the rest capacitive gap creates dynamic pull-in condition. As shown in Figure 81, capacitive pull-in of the device occurs over 90 V DC towards in-plane direction (Figure 81 (top)) and 33V DC to out-of-plane direction (Figure 81 (bottom)). The simulation of pull-in behavior is done by increasing V_P applied to

resonant mass while maintaining potential of electrodes to ground, which is the worst-case scenario which employs the largest electrostatic forces.

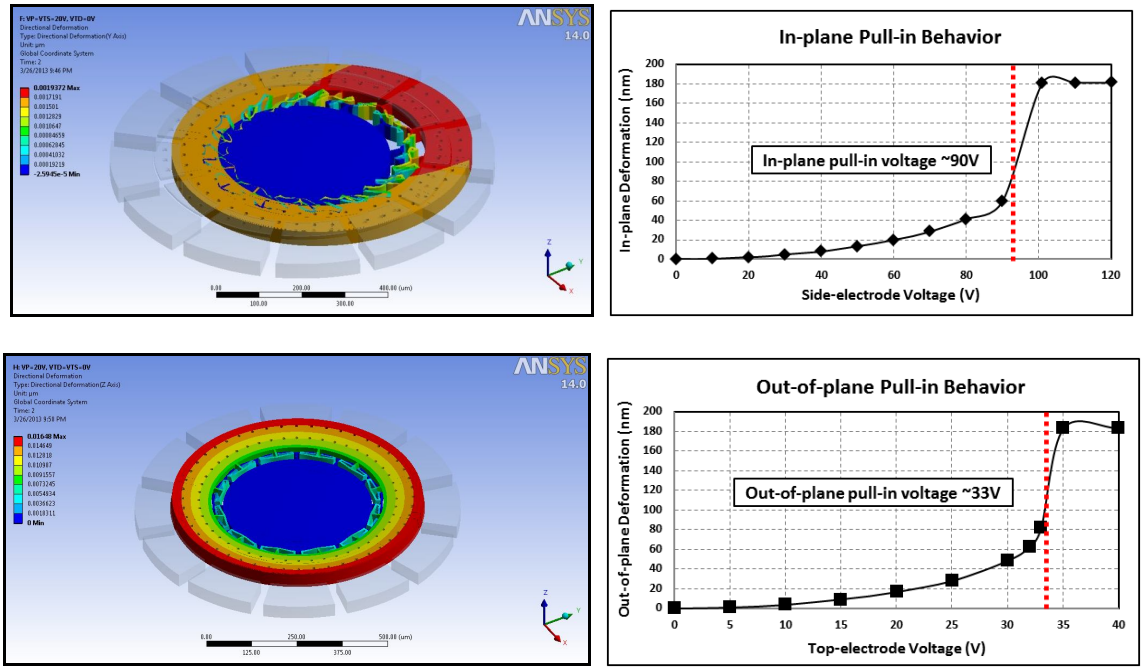

Figure 81: Pull-in behavior simulation. Proof-mass translation towards side electrode (left, top) and top electrodes (left, bottom) are presented. Corresponding pull-in voltages are plotted in (right, top) and (right, bottom), respectively.

4.5.2.4. Sensitivity and Mechanical Noise Level

The fundamental expression of Coriolis-force induced mechanical deformation in resonant gyroscope is shown as:

$$\left|q_2(j\omega_n)\right| = \frac{2\cdot\lambda'\cdot\Omega_Y\cdot\omega_0\cdot q_1}{\sqrt{\left(\omega_n{}^2-\omega_0{}^2\right)^2+\left(\frac{\omega_n\cdot\omega_0}{Q_S}\right)^2}}. \qquad \textbf{(82)}$$

In addition, the output current generated by rotation rate is expressed by

$$i_{output}(t) = (V_P - V_{Bias}) \cdot \frac{dC_S}{dt} = (V_P - V_{Bias}) \cdot \frac{dC_S}{dq_S} \cdot \frac{dq_S}{dt}$$

$$= \frac{\varepsilon_0}{d_{02}} \cdot (V_P - V_{Bias}) \cdot \left\{ \begin{aligned} & -\frac{1}{9} \cdot \cos\theta \cdot \sin\frac{3 \cdot \Delta\theta_n}{2} \cdot \left[\frac{1}{d_{02} \cdot (R - C_{anchor})} \right] \\ & \cdot \left\{ \begin{aligned} & 2 \cdot \left[R^3 - (R-w)^3 \right] \\ & -3 \cdot C_{anchor} \cdot \left[R^2 - (R-w)^2 \right] \end{aligned} \right\} \end{aligned} \right\}$$

$$\cdot \frac{2 \cdot \lambda' \cdot \Omega_Y \cdot \omega_0 \cdot \omega_n}{\sqrt{\left(\omega_n{}^2 - \omega_0{}^2\right)^2 + \left(\frac{\omega_n \cdot \omega_0}{Q_S}\right)^2}} \cdot q_1 \cdot \cos(\omega_0 \cdot t) \qquad \textbf{(83)}$$

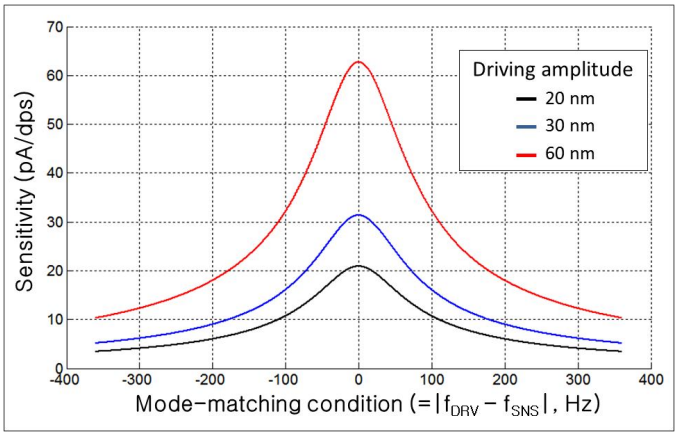

Figure 82: Plot for frequency split vs. sensitivity. Δf=0 Hz condition shows maximum sensitivity.

whereas Brownian noise level caused by random collision with surrounding medium is expressed as follows;

$$\Delta x(Brownian) = \sqrt{\frac{4 \cdot k_B \cdot T \cdot \omega_n}{M \cdot Q_S}} \times \frac{1}{\sqrt{\left(\omega_n^2 - \omega_0^2\right)^2 + \frac{\omega_n^2 \cdot \omega_0^2}{2 \cdot Q_S^2}}} \left[m/dps/\sqrt{Hz} \right] \qquad \textbf{(84)}$$

where λ', Ω_Y, q_1, ω_n, ω_0, Area, and Q_S are Coriolis-coupling coefficient, input rotation rate, driving amplitude, natural frequency of sense and drive-modes, capacitive area of sense electrodes, and sense-mode Q-factor, respectively. k_B and T denote Boltzmann's constant and operating temperature of the sensor, respectively.

Figure 83 shows the scale factor comparison between ANSYS simulation results and analysis.

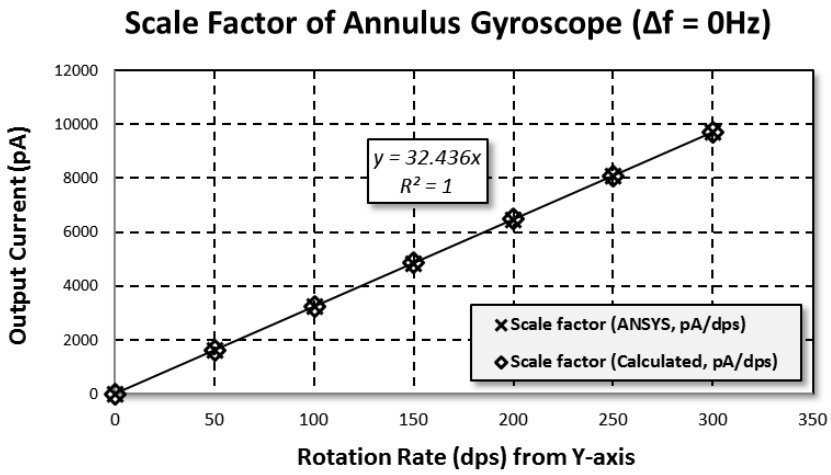

Figure 83: Scale factor comparison between ANSYS simulation and analysis.

By equating (82) and (84), mechanical noise equivalent rotation rate (MNEΩ) is derived as follows;

$$MNE\ \Omega = \Omega_Y\big|_{\min} = \frac{1}{2 \cdot \lambda' \cdot q_1} \cdot \sqrt{\frac{4 \cdot k_B \cdot T \cdot Q_S}{M_S \cdot \omega_n}} \cdot \left(\frac{\omega_n}{\omega_0}\right) \cdot \sqrt{\left(1 - \frac{\omega_0{}^2}{\omega_n{}^2}\right)^2 + \left(\frac{\omega_0}{Q_S \cdot \omega_n}\right)^2} \quad \textbf{(85)}$$

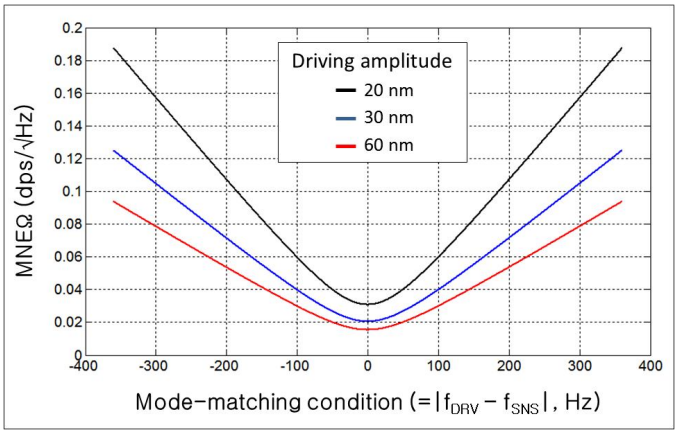

Figure 84: MNEΩ vs. mode-matching condition and driving amplitude.

At a mode-matched condition ($\omega_n = \omega_0$) with driving amplitude of 30nm and Q_S of 10,000, the sensor can resolve 0.02 dps/√Hz of input rotation rate with sensitivity of 32pA/dps/electrode.

4.5.3. Fabrication Process Flow

The revised HARPSS^{TM} process is outlined in Figure 85. The process starts from creating initial thick thermal oxide layer on a 40μm thick (100) SOI substrate (Figure 85(a)). The device layer is etched through using the thermal oxide mask after patterning and 300nm thick sacrificial oxide (SACOX) is created by thermal oxidation (Figure 85(b)). The 1st doped LPCVD polysilicon is deposited and refilled trenches and holes, then etched back from the surface by DRIE (Figure 85(c)). The trench-refilled 1st polysilicon is etched from the area where the top electrodes are supposed to be defined. 3μm-thick TEOS oxide is deposited to refill the empty trenches and patterned (Figure 85(d)). 300nm TEOS 2nd SACOX is deposited and patterned to create a vertical capacitive air gap (Figure 85(e)). The 2nd doped polysilicon is deposited, annealed and patterned to finalize the structure (Figure 85(f)). The base wafer batch is finished by release in HF with timed control (Figure 85(j)).

The fabrication process is followed by wafer-level packaging (WLP) of base MEMS substrate. To define vertical feedthroughs, single crystal silicon (SCS) wafer is partially etched to define via patterns. Then, the trench is refilled by insulator followed by cavity etching and Au metallization steps (Figure 85(h)). After grinding the backside of capping substrate, base substrate and capping wafer are merged by Si-Au eutectic

bonding. The WLP process is completed by deposition and patterning of insulators and metal pads for testing.

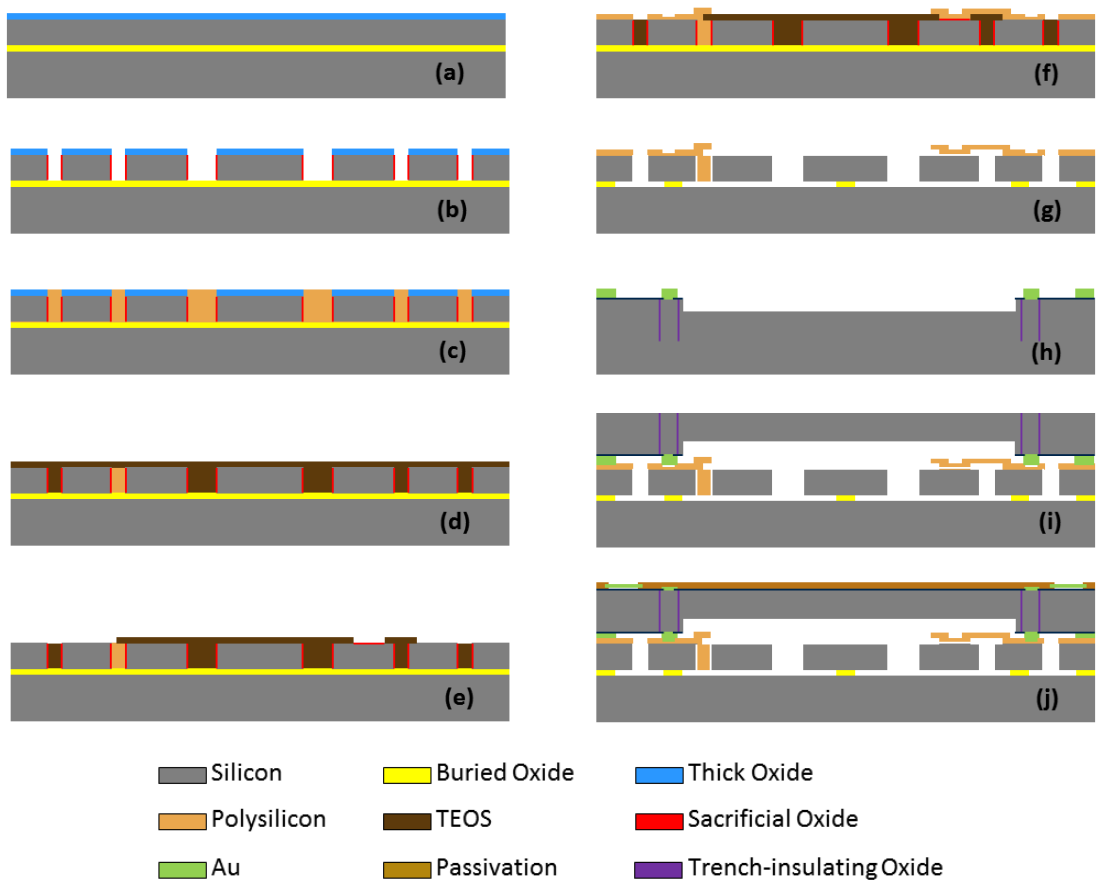

Figure 85: Base MEMS wafer and WLP process.

The SEM view of an annulus gyroscope is shown in Figure 86. It clearly shows an annulus body connected by flexural springs to the middle of the device, four side electrodes, and eight top electrodes fabricated on a SOI substrate. The zoom-in of flexural spring that connects central V_P pad and resonant mass is shown in Figure 87 (left). A top electrode has release holes to facilitate wet HF release is shown in Figure 87 (right). Figure 88 shows 6" substrate before (Figure 88 (left)) and after (Figure 88 (right)) wafer-level capping process.

Interestingly, the process platform can also co-fabricate IMUs in the same wafer. Figure 89 demonstrates pitch-and-roll gyroscopes co-fabricated with a yaw gyroscope and a single proof-mass tri-axial accelerometer. Figure 90 shows six degree-of-freedom IMU with six elements to sense each axis' rotation and acceleration. Wafer-level grinding and thickness thinning is performed and shown in Figure 91. The total thickness is reduced from 900µm (Figure 91 (left)) to 400µm (Figure 91(right)).

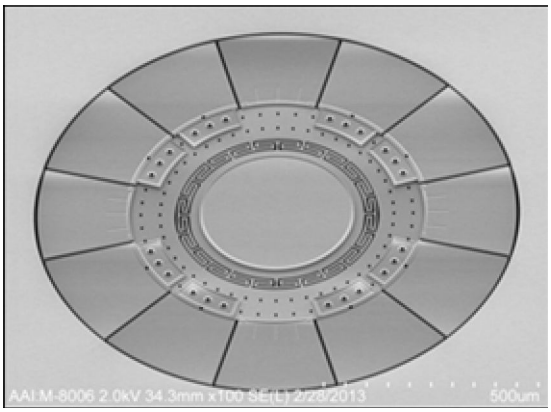

Figure 86: Fabricated annulus gyroscope (presented with courtesy of Qualtré Inc.).

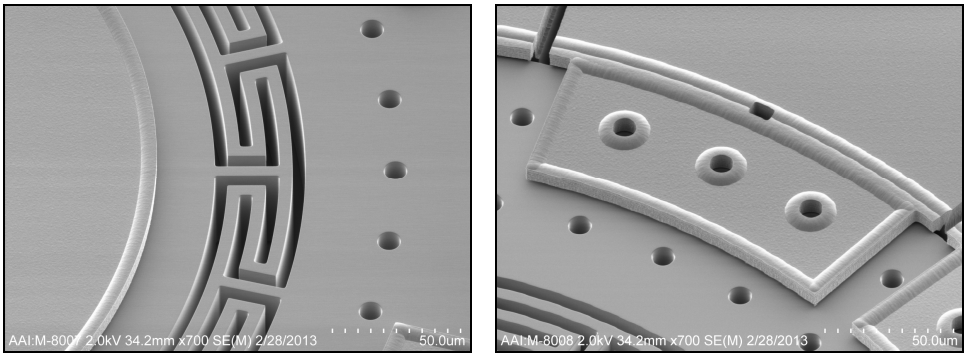

Figure 87: Zoom-in of flexural spring connecting anchor and annulus (left) and top-electrode (right) (presented with courtesy of Qualtré Inc.).

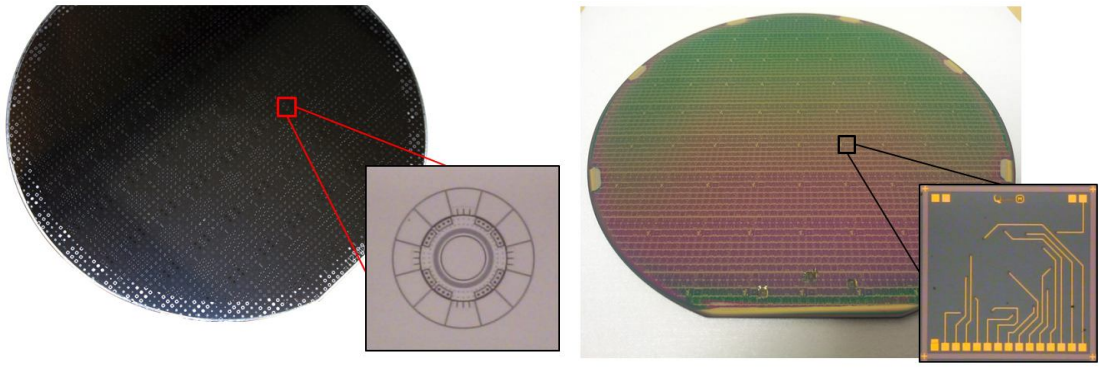

Figure 88: Processed wafer before (left) and after (right) WLP (presented with courtesy of Qualtré Inc.).

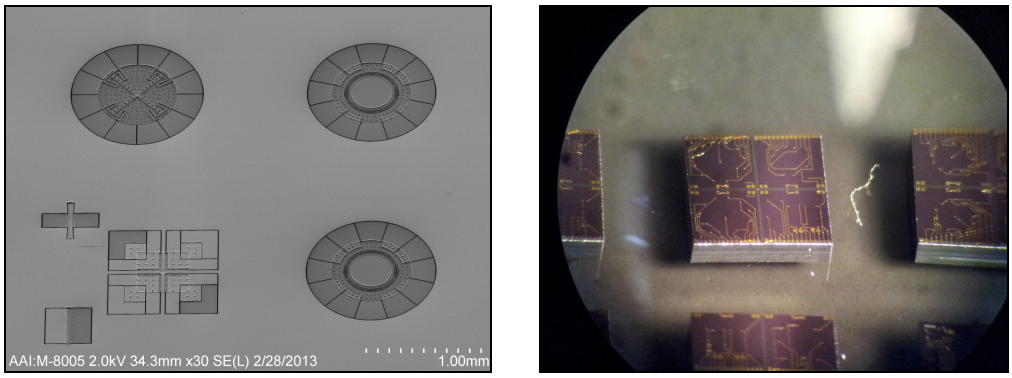

Figure 89: Co-fabricated IMU die with single proof-mass tri-axial accelerometer and tri-axial gyroscope (presented with courtesy of Qualtré Inc.).

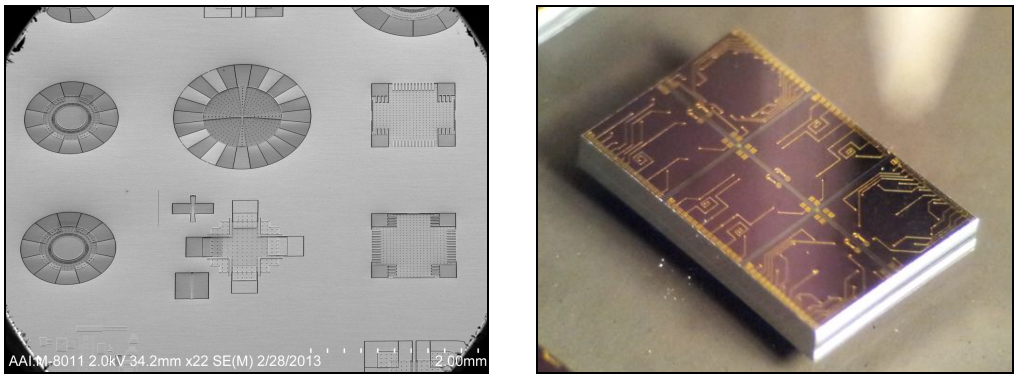

Figure 90: Co-fabricated IMU die with three single-axis accelerometer and tri-axial gyroscope (presented with courtesy of Qualtré Inc.).

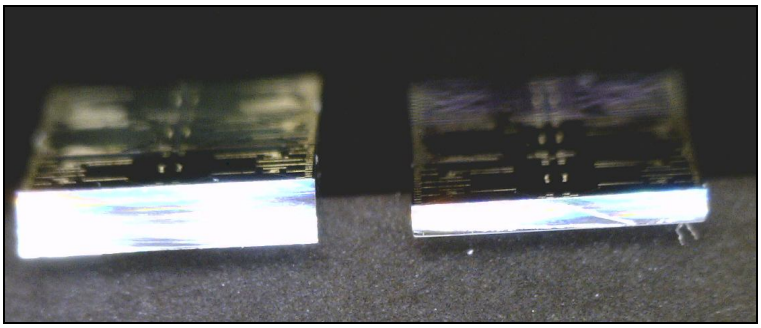

Figure 91: IMU die before and after wafer-level grinding (presented with courtesy of Qualtré Inc.).

4.5.4. Characterization

4.5.4.1. Frequency Response of Annulus Gyroscope

As explained, the annulus gyroscope has side and top electrodes with narrow horizontal and vertical capacitive air gaps, respectively. The selectively defined gap sizes result in significant signal strength differences between the side and top electrodes with the given in- and out-of-plane motion of the vibrating mass. Two different cases of device actuation and signal readout are measured and plotted in Figure 92 and Figure 93. When signal is driven from *Drive-in* side electrode, signal observed from *Sense* top electrode exhibits more than 10dB lower signal than from *Drive-out* electrode (Figure 92). A similar response is shown when the device is actuated from Ω_Y^+ electrode and readout from the side and top electrodes simultaneously (Figure 93). Consequentially, since in-plane driving resonance mode is detected from the side electrode with significant difference in signal level compared from top electrodes, locking into wrong resonance mode can be prevented. Similarly, out-of-plane sense mode is detected from top electrode with minimal influence from driving mode quadrature signal component.

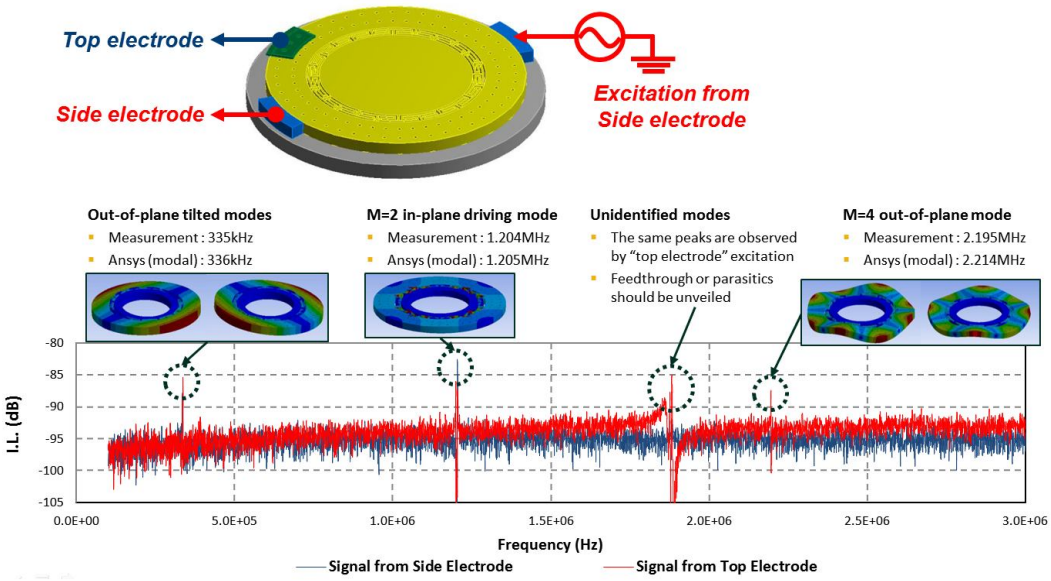

Figure 92: Measured frequency responses of the annulus gyroscope. Device is excited from a side electrode and the signals are detected from a side and top electrodes, simultaneously.

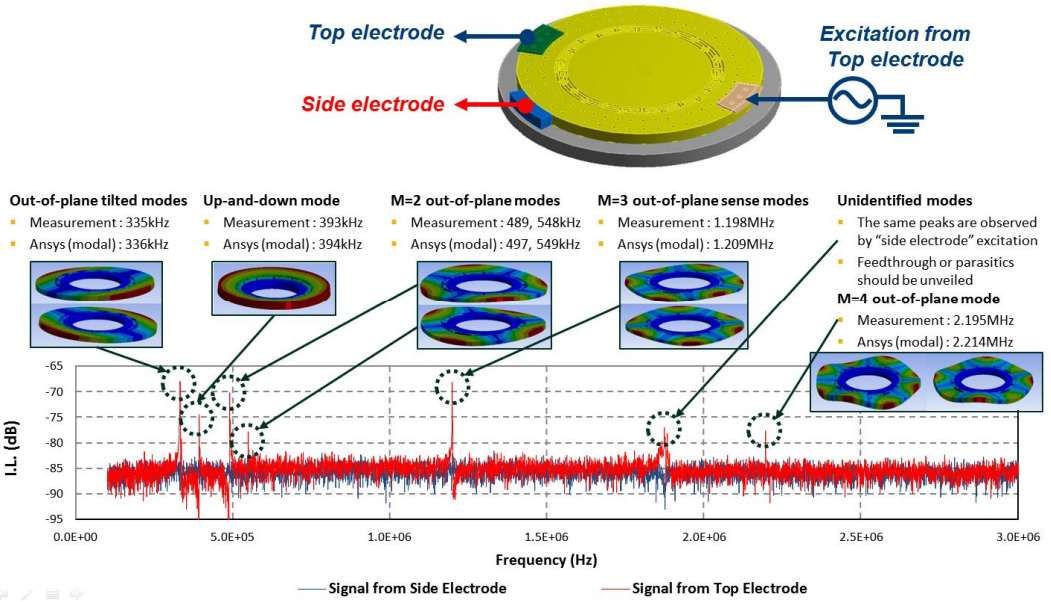

Figure 93: Measured frequency responses of the annulus gyroscope. Device is excited from a top electrode and the signals are detected from a side and top electrodes, simultaneously.

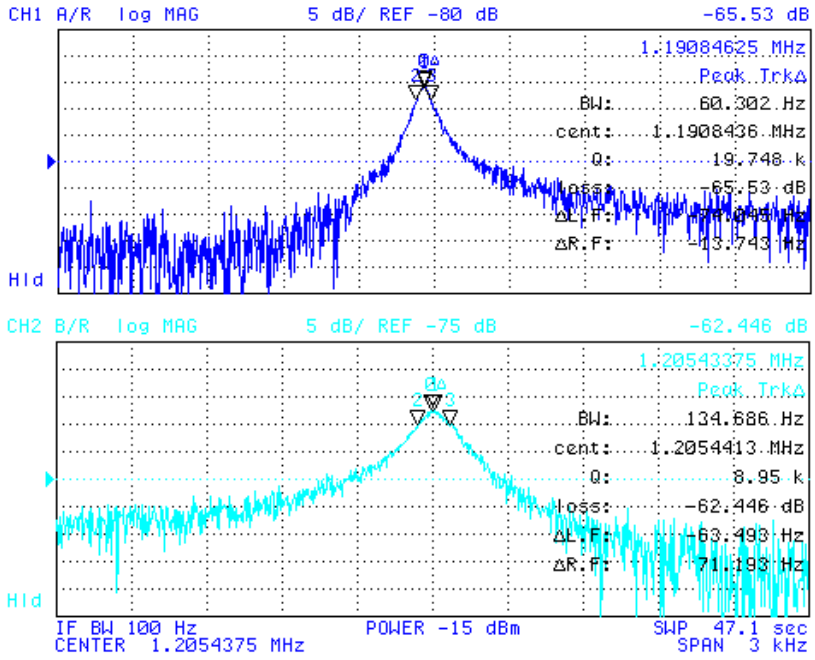

Figure 94: Measured Q-factors of the drive-mode (top) and sense-mode (bottom) at split-mode condition.

Figure 94 shows zoom-in of drive and sense mode response. High Q-factors of 20k and 9k for drive and sense modes, respectively, are observed under mode-split condition.

4.5.4.2. Resonance Frequency Allocations from Included Designs

Due to the uncertainties existing in the fabrication process, initial frequency locations of the annulus gyroscope can alter from device to device and batch to batch of the fabrication. The uncertainties include slightly different sidewall angle after DRIE process due to non-uniformity existing in the tool, critical dimension (CD) loss variations in each lithography process, thickness differences in substrates used for each batch, differences in flexure width caused by oxidation process, and possible defects in the substrates. To perform a statistical study about the process variations and the possible fabrication irregularity, lithography maskset embraced five different outer-radii. Given

center design with 348.5µm in outer-radius, ±1.5µm and ±3.0µm of offset in the dimension are applied (Figure 95). The initial drive- and sense-modes resonance frequencies are recorded and compared with FEA performed using ANSYS Workbench™ (Figure 96). The FEA shows drive mode frequency with respect to the outer radius changes at Δf_{Drive}=+4.44kHz/µm and Δf_{Sense}=+4.67kHz/µm while measurement results demonstrate Δf_{Drive}=+5.56kHz/µm and Δf_{Sense}=-4.81kHz/µm. Although discrepancy was observed between measurements and simulations, the employed model is able to expect the frequency trend and mode-matchable device.

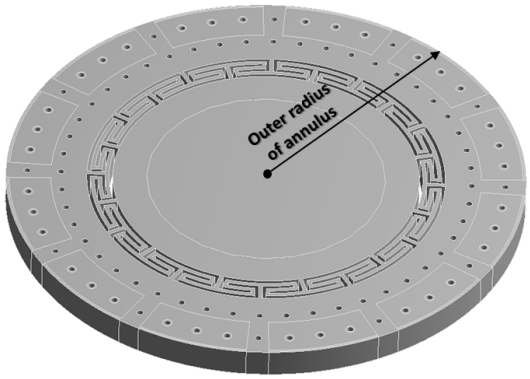

Design #	Outer radius of annulus
1	345.5 µm
2	347.0 µm
3	348.5 µm
4	350.0 µm
5	351.5 µm

Figure 95: Included designs in the lithography maskset.

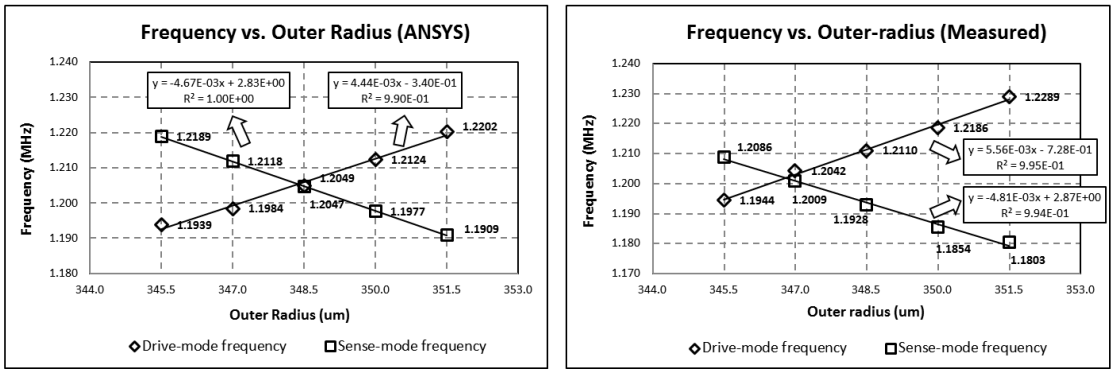

Figure 96: Resonance frequency comparison between FEA (left) and measurement (right).

To verify the batch-to-batch process variations, two wafers from separate process lots are continued for the measurements. Design 1-3 from five stepping reticles of each wafer are measured and plotted in Figure 97. Erratic behaviors are not observed in the measurement, and process variation is recorded to be equivalent to ~0.3µm of outer-radius difference.

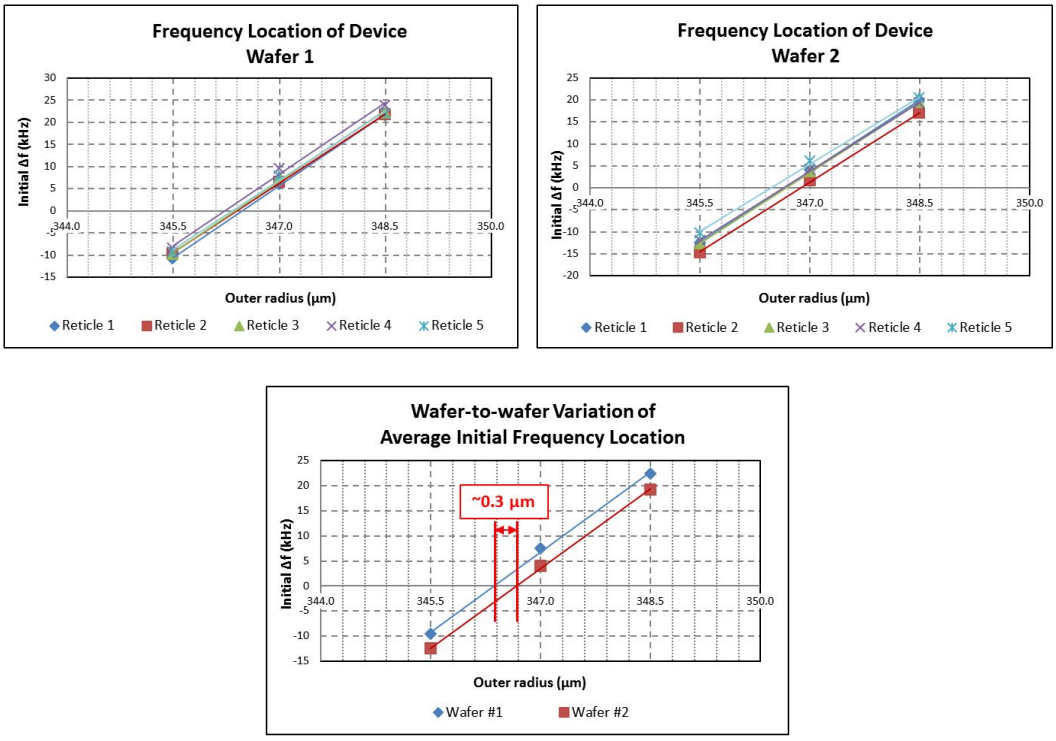

Figure 97: Wafer-to-wafer variation of frequency response (top). Averaged response of each wafer is plotted and shows average variance of 0.3µm.

4.5.4.3. Frequency Tuning and Mode-Matching

To enable high performance with low mechanical noise and high sensitivity, drive resonance mode should be mode-matched with sense mode. The mode-matching is performed by adjusting drive and sense DC tuning voltages while applying a fixed polarization voltage (V_P) to the center of annulus mass. The trace data during mode-

matching procedure is collected and plotted in Figure 98. During the frequency tuning procedure, both drive and sense-modes maintained the same insertion loss (I.L.) which proves vibration amplitude and Q-factors are not affected by tuning process. Zoom-in of the mode-matched peak shows high Q of 9.8 k (Figure 99). For the ease of DC settings in the measurements, all tuning voltages are set to have |VP-VTD| = |VP=VTS| = 9.46V with VTD = VTS = 0V, which are realistic level of potential available from the interface ASIC. The spectral purity is measured in 1 MHz frequency span. Under mode-matched condition with differential sensing scheme, all other spurious modes are not detected at the sensing electrodes suggesting the output signals are detected from the mode-matched peaks.

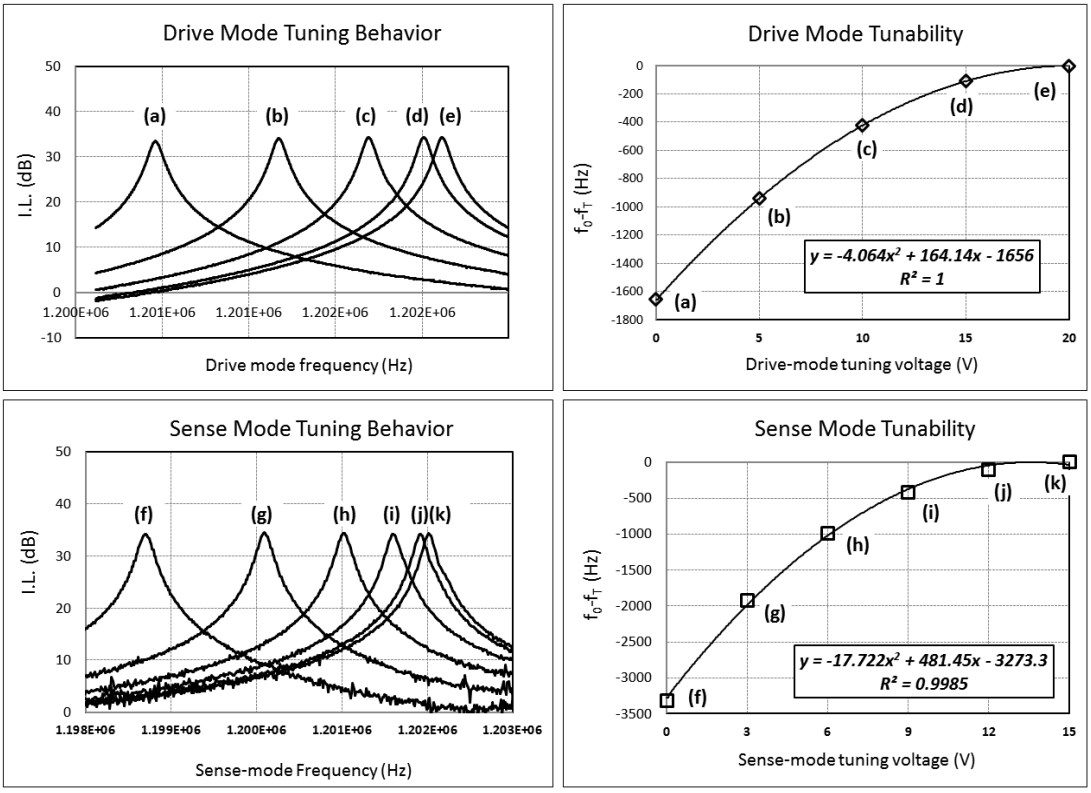

Figure 98: Measured tuning behavior of the annulus gyroscope.

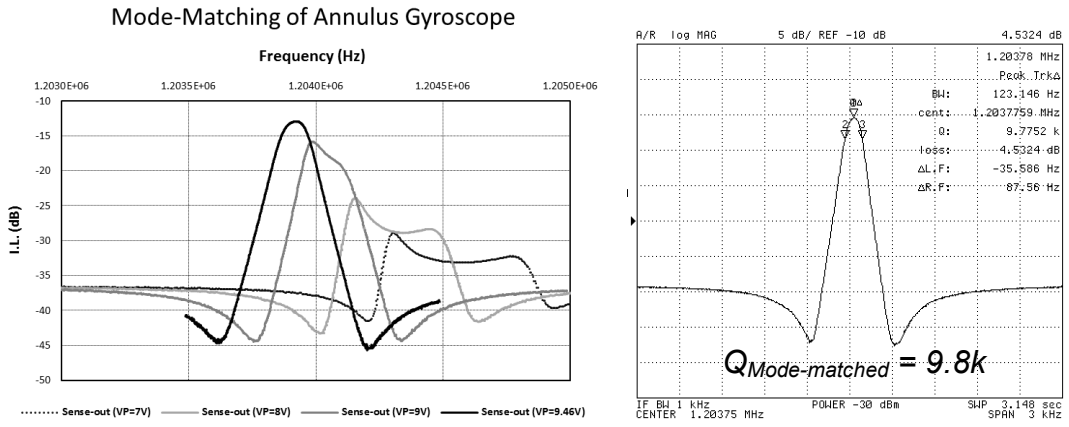

Figure 99: Measured frequency responses during mode-matching procedure (left). Zoom-in of mode-matched resonance peak. High Q-factor of 9.8k is observed (right).

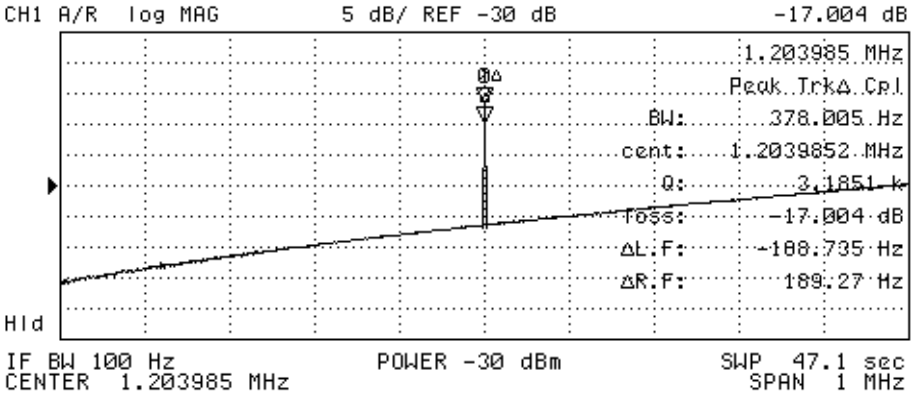

Figure 100: Measured frequency response in 1 MHz range. The response shows spurious-free output signal.

4.5.4.3. Pressure Level Dependency in Device Q-factors

In order to estimate approximate required packaging vacuum level for a certain level of performance, the Q-factors are measured in different vacuum level from 10mTorr to 10Torr (Figure 101).

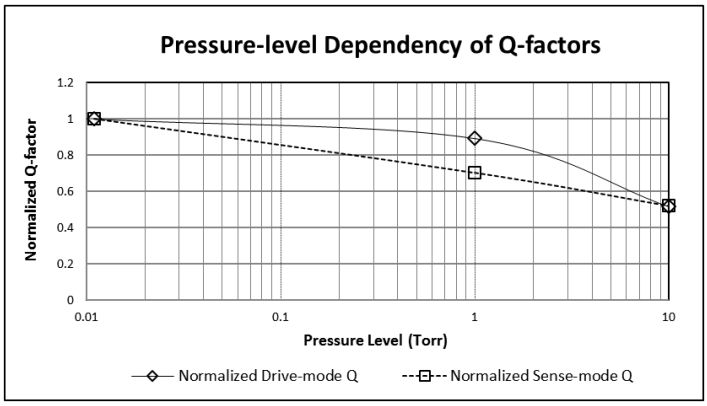

Figure 101: Measured Q-factors vs. vacuum level.

4.5.4.4. Temperature Dependency of Device

Q-factor dependency on the temperature variance is important cause of performance degradation at higher temperature than its normal operating condition [19, 20, 42, 77]. Since thermoelastic damping causes reduction in silicon-based resonant devices in Q-factor at higher operation environment, the deviation and trend of Q-factor across the temperature should be carefully characterized.

The trend of Q-factors of drive and sense modes and their hysteresis characteristic are both characterized (Figure 102). The measured drive and sense mode Q's change by 55% and 45%, respectively, and no hysteresis is observed for both modes. The trends of Q-factor follow parabolic function imposing expectable behavior that can be offset by electrical frequency tuning. Temperature coefficients of frequency from each mode are measured and plotted to be -28.5 ppm/°C and -25.2 ppm/°C for drive- and sense-modes, respectively.

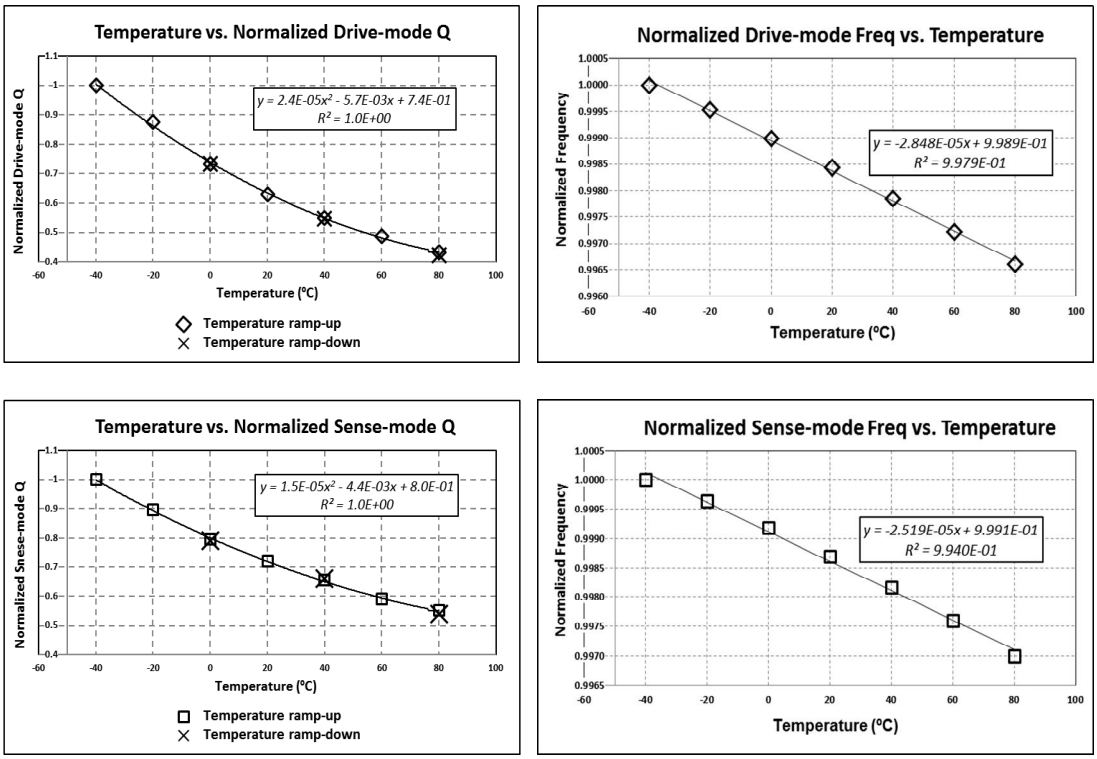

Figure 102: Temperature-dependency of Q-factors. Both drive- and sense-modes are measured to be hysteresis-free during ramping-up and down of temperature.

4.4.4.5. Scale Factor and Cross-axis Sensitivity

Figure 103 shows a schematic of the ASIC interfaced with the annulus gyroscope for the closed-loop operation and sensitivity measurement. Drive-out signal is amplified by drive transimpedance amplifier (DTIA) followed by automatic gain controller (AGC) to establish a constant vibration amplitude. An additional gain stage (Driver) is connected afterwards to the drive-loop to augment excitation force. The signal is then fed back to Drive-in electrode of packaged MEMS device for the drive-mode closed loop self-oscillation. Sense-mode signal is monitored and amplified by sense transimpedance amplifier (STIA) then quadrature component is cancelled by adding a portion of drive-out signal. The sense signal is demodulated after adding extra gain from programmable gain

amplifier (PGA_RF). Rate response is observed after low-pass filter (LPF) to screen high-frequency signals and extra amplification blocks (PGA_LF and Rate Amp).

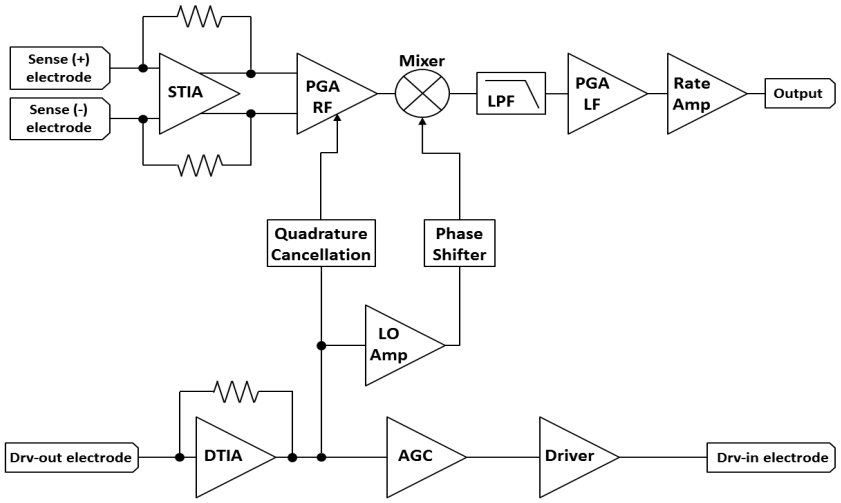

Figure 103: Schematic of interface ASIC.

Output signal after DTIA is shown in Figure 104. The amplitude of $322mV_{Peak\text{-}to\text{-}Peak}$ corresponds to 20nm of drive-mode vibration amplitude across 300nm side air gap.

Figure 105 shows interface between a MEMS die and an ASIC. An interposer is placed between MEMS and ASIC units for pin-to-pin compatibility during wirebonding.

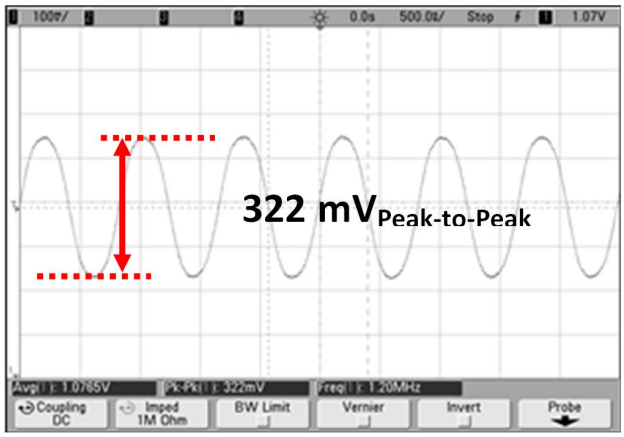

Figure 104: Measured ac signal amplitude after DTIA stage in closed-loop operation.

The package is placed on top of rotation table for the sensitivity and cross-axis sensitivity measurement (Figure 105 (right)). For the characterization of lateral rotation-axis, entire rotating stage is vertically placed with carefully measured angle to align to exact pitch-or-roll. Scale factor is measured up to 300dps of input rotation rate from pitch, and cross-axis sensitivity is observed by rotating the device at roll. Sensitivity of 481μV/dps is measured from differential sense outs without observable cross-axis sensitivity component (Figure 106). Exemplary sense-out signals after demodulation are shown in Figure 107.

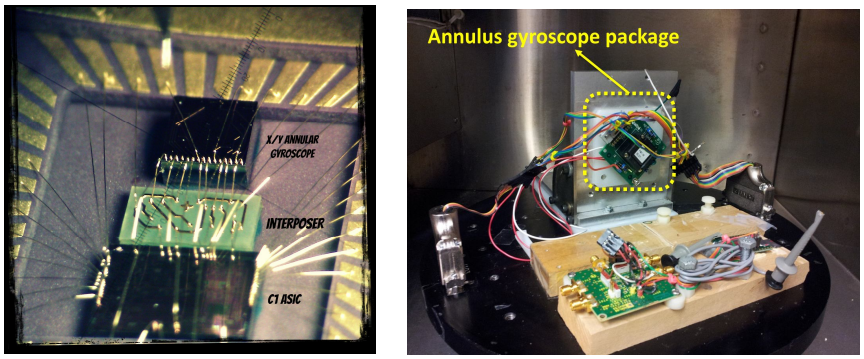

Figure 105: Interface between MEMS and ASIC (left) and device testing on rate table (right) (presented with courtesy of Qualtré, Inc.).

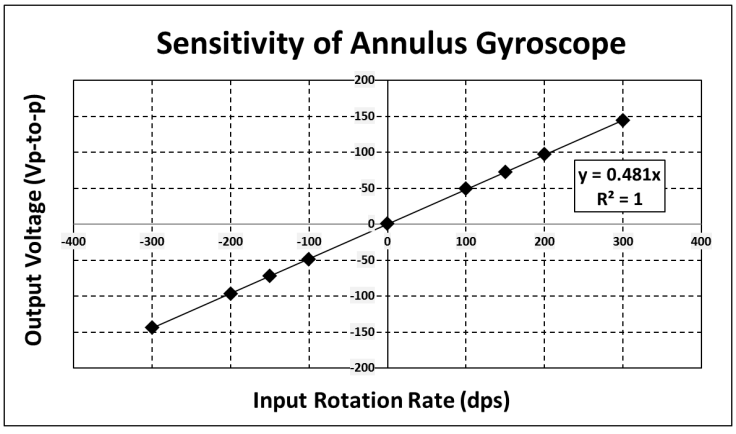

Figure 106: Measured scale factor from pitch rotation rate.

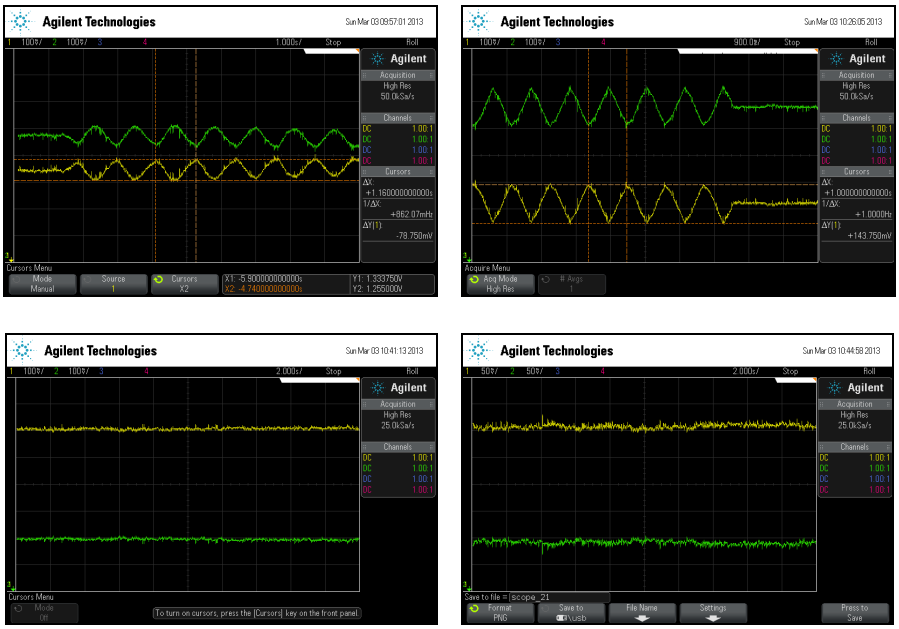

Figure 107: Rate-output signal after demodulation. Cross-axis sensitivity is not observed in the measurement.

4.6. Scaling Property of Annulus Gyroscope.

Since the noise performance and scale factor are proportionally improved by effective mass of the annulus mass in the resonant motion, the scaling property should be investigated to identify the benefits from augmented device dimension.

Simplified annulus model is used for the FEM and analysis (Figure 108). The unconstrained model has inner and outer radius that determine lateral dimension of the proof mass, and thickness. Because of the non-degenerate property of in- and out-of-plane modes, a certain condition that defines mode-matched condition exists.

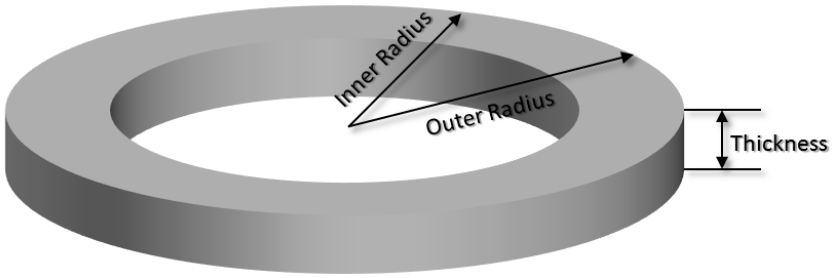

Figure 108: Simplified annulus model utilized for scaling property study.

Using 40, 60, and 80µm-thick (100) substrates, the mode-matched frequency and mechanical bandwidth with assumed Q-factor of 10,000 are plotted in Figure 109. The inner-radius is varied from 600µm to 900µm. With the increased proof-mass dimension, the effective masses of drive- and sense-modes are increased proportionally.

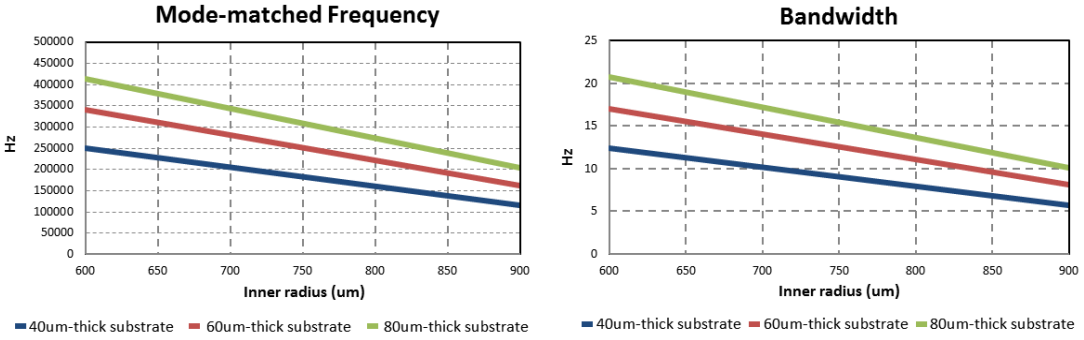

Figure 109: Mode-matched frequency and bandwidth of annulus gyroscope with scaling property.

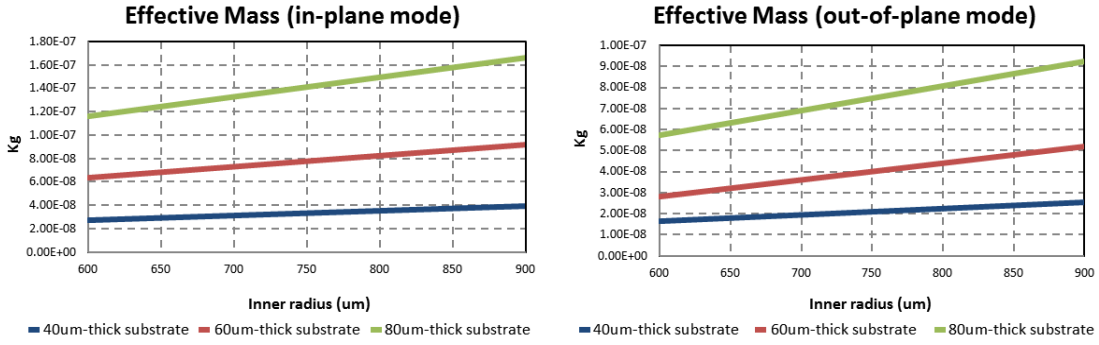

Figure 110: Effective mass of in-plane drive mode (left) and out-of-plane sense mode (right).

The mechanical noise level which is defined by (71) is plotted with respect to the dimension of proof-mass. The assumed driving amplitude is 200nm across 2μm side air gap, and sense-mode Q of 10,000 is used. Since product of frequency and effective is decreasing as the device goes to lower frequency, the noise level is proportionally increased with lateral dimension of the annulus. However, thicker substrate with same dimension is decreasing the noise level accordingly as shown in Figure 111.

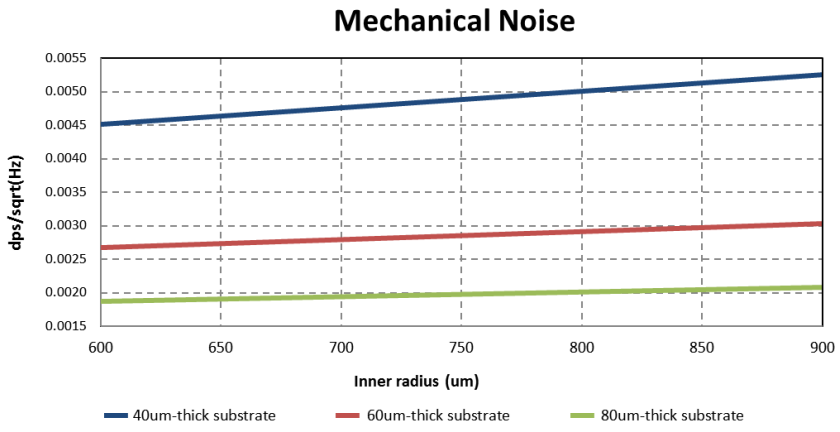

Figure 111: Noise performance of annulus gyroscope with scaling property.

CHAPTER 5

CONCLUSIONS AND FUTURE WORKS

5.1. Contributions of the Performed Research

This dissertation presented the design, modeling, fabrication, and characterization of high-frequency tri-axial gyroscopes integrated in a planar configuration. The brief summary of the technical contributions can be listed in this section.

5.1.1. Capacitive high-frequency yaw gyroscope

The design, modeling, fabrication, and characterization of high-frequency yaw gyroscope with wide full-scale range were performed. For the design works, ANSYS Workbench^{TM} was employed to identify resonant frequency of the device, electrostatic tuning/detuning of the operating frequency, and to simulate rate sensitivity with full-scale range. TRANS126 element was used to model the electromechanical component with a complete set of the device. The device was fabricated on a 60μm-thick (100) single crystal silicon SOI substrate via HARPSS^{TM} process platform. Yaw gyroscope thus retained high aspect ratio for the efficient capacitive signal transduction and wide bandwidth with bandpass-filter response. The targeted Q of 1k for bandwidth of 3kHz at 3 MHz was achieved to address the estimated worst-case frequency split of 2kHz. As a result, the device could operate with DC polarization of 10V obviating complicated DC tuning voltages in the characterization process. The rate response was measured up to 500 dps among the expected full-scale range wider than 30,000dps. Frequency drift due to the

temperature variance revealed the bandpass-filter response was maintained over (-)20°C to (+)70°C with less than 10% variance in the mode-matched Q-factor.

To meet the specification for navigational grade MEMS gyroscopes, the methods to increase Q-factor were developed in two different methods. The first method is to employ HARPSS^{TM} process with HF release from the backside of SOI substrates. This method does not require excessive release holes in the resonating disk, and thus minimize thermoelastic damping that can significantly drop overall Q-factor. The second method was to employ customized SOI substrate with prepatterned buried cavity oxide layer. The customized SOI wafer does not require HF release from the backside of substrates, therefore, wafer-level packaging becomes simplified.

5.1.2. Capacitive Dual Pitch-and-Roll Gyroscope

A single proof-mass pitch-and-roll gyroscope was designed and modeled using ANSYS Workbench^{TM}. An in-plane drive-mode and two orthogonal out-of-plane sense-modes are simulated and mode-matched at a specific dimension of the annulus resonant mass. To address the process variation and maintain the mode-matched behavior under process variations, electrostatic tuning behavior was simulated and verified its tunability to compensate thickness variation of ±0.3μm in the substrate. The characterization of the fabricated device exhibited near-independent frequency tuning response from each resonance mode, i.e. an in-plane drive-mode and out-of-plane sense-modes. High Q-factors of > 10k were observed from all modes, and the Q-factors were remained the similar level until the pressure level of 1 Bar. Although high cross-axis sensitivity of

~25% was measured, the crystalline dislocation between anisotropic substrate and electrodes was suggested as a root-cause of the issue.

5.1.3. Capacitive High-frequency Pitch/Roll Gyroscope

To eliminate cross-axis sensitivity, the device employed a mode-matching of an in-plane drive-mode and an out-of-plane sense-mode, and then the unused out-of-plane mode was detuned from the mode-matched frequencies. Since Coriolis response is not delivered to the split mode, cross-axis sensitivity could be completely eliminated. Dual lateral-axes rotation sensing can be performed by employing two annulus gyroscopes with 90˚ spatial apart.

5.1.4. Development of IMU Integration Process Platform

HARPSS^{TM} process [6, 12, 14, 63] has been providing high aspect ratio in capacitive air gap regardless of lithography process. However, the process enabled capacitive electrodes at the perimeter of resonant mass that can only sense in-plane motion of the resonant mass. The revised process platform, which is called "HARPSS^{TM} ver.4 process platform", is developed to resolve in- and out-of-plane motions of the proof-mass through selectively defined gap sizes. The different gap sizes exist in the side and top capacitive air gaps that are defined at different steps using thermal oxidation or conformal deposition of silicon dioxide. In addition, the process platform enhanced frequency tunability with minimized cross-mode tuning behavior, signal isolation between in- and out-of-plane modes, and reduced amplitude in quadrature signals component. Furthermore, accelerometers are co-fabricated with tri-axial gyroscopes thus

enabling a single chip IMU integration. Additionally, resonators as a timing element could be integrated in the same batch.

5.2. Future Works

Tri-axial gyroscopes were presented in this dissertation. However, further works are remaining to produce better performance. The future works are categorized in three domains in this section.

5.2.1. Development of ASIC with Temperature Compensation

The frequency shift and Q-factor variations with respect to the temperature change are discussed in the characterization part of each device. In order to maintain mode-matched response in the annulus gyroscope and compensate Q-factor variation across the given temperature range for commercial applications (-40°C to 85°C), interface ASIC for annulus gyroscope should be developed. The possible methods will include development of automatic mode-matching algorithm that will function in the range of frequency split caused by temperature variance. In addition, large range of controllable gain in the sense amplifier and drive-loop will be required.

5.2.2. Performance Enhancement of Yaw Gyroscope

Increasing Q-factor is the most preferable method that will enhance the performance of yaw gyroscope. Increased Q-factor will reduce mechanical and electrical noise level without augmenting proof-mass dimension. To enhance Q-factor, a solid disk

proof-mass without perforation is suggested with the promising process flows. In addition, the device operation with optimized design parameters is required.

5.2.3. Performance Enhancement of Pitch-and-roll Gyroscope

The design of annulus gyroscope starts to identify tunability of the device to compensate process variations that stays in ±0.3μm of thickness variation in the commercially available SOI substrate. Once the device is fabricated using a substrate with accurate thickness control, i.e. elimination of process variance, driving amplitude can be increased by employing large capacitive air gaps. In addition, solid annulus mass similar to increase Q-factor can be promising candidate to improve resolution of annulus gyroscope. The process flow and design strategy may be shared with solid-disk fabrication method.

APPENDIX A

CAPACITIVELY-COUPLED ELECTROMECHANICAL SIMULATION USING ANSYS WORKBENCH™

The operation of capacitive gyroscopes involves electrostatic excitation of the resonant mass and signal transduction through narrow dielectric gaps. Throughout this dissertation, ANSYS Workbench™ was employed to simulate and analyze the performance of the resonant gyroscopes. Among the various TRANS-elements that ANSYS provides with, TRANS126 elements are incorporated with pitch/roll rate gyroscopes for the simulation. This appendix will discuss about the methods in applying environmental factors and parameters for the capacitive gyroscope simulations.

The simulation should be initiated from generating 3-D model using design modeler. Considering the annulus mass involves in- and out-of-plane resonance modes, the side- and top-electrodes interacting with the mass should be defined when constructing the geometry. Figure 112 shows the geometry of the model and cross-sectional views of the device. In the ANSYS design modeler, narrow capacitive-gaps are drawn and defined to excite and readout signals. As analyzed and designed, top electrodes (shown as A-A') retain 300nm of vertical capacitive gaps and 5μm of horizontal gaps while side electrodes (shown as B-B') have 300nm of horizontal gaps only.

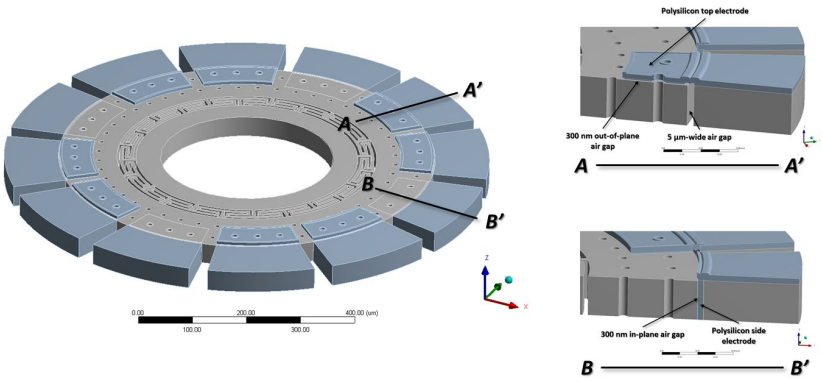

Figure 112: 3D geometry used for the pitch/roll rate gyroscope. Cross-sectional views of electrodes and annulus mass are shown.

After applying material property in the model shown in Figure 112, mechanical boundary conditions to assign fixed parts in the model should be defined. Figure 113 illustrates the mechanical fixed supports in the simulation environment. The edge of the top electrodes, whole surfaces of side electrodes, and inner part of central regions of the annulus mass are designated as the mechanical fixtures.

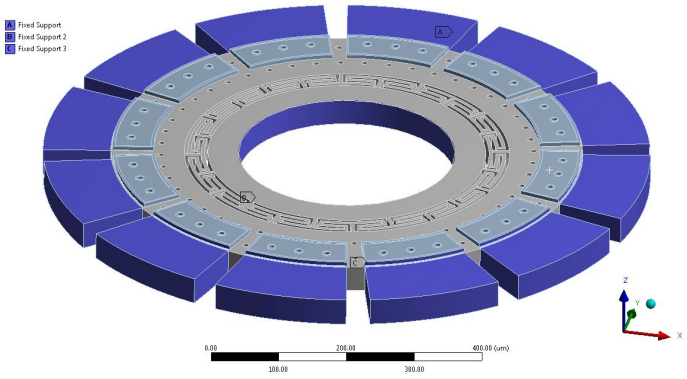

Figure 113: Mechanical boundary condition of pitch/roll annulus rate gyroscope.

In order to generate TRANS126 elements between the electrodes and the interacting surface of the annulus resonant mass, the surface names should be assigned to be incorporated in the ANSYS script as variables. Figure 114 (left) shows the annulus

mass with two exemplary interacting surfaces. Face name “eds4” and “edt3” indicate interacting surface on the side and top of the annulus mass, respectively. On the other hand, Figure 114 (right) illustrates interacting surface at the electrodes. The “eds4 (and edt3)” on the annulus mass interacts with “eps4 (and ept3)” in the electrodes.

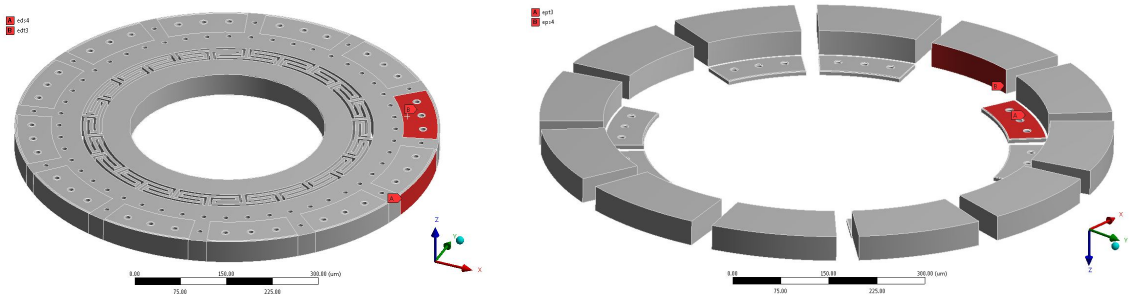

Figure 114: Interacting surfaces on the annulus mass (left) and electrodes (right).

In order to couple the mechanical motion with applied electrical signal in the simulation, TRANS126 elements should be generated. Following script can be used to generate the trans-elements.

```
nsel,s,node,,eds4                                   ! Selects all nodes from central drive of mass 1
cm,cap_eds4,node                                    ! Names the nodes of the selected area
emtgen,'cap_eds4','EMTElem_eds4',pad_eds4','ux',gap,gap/100   ! Generates TRANS126 elements

nsel,s,node,,edt3                                   ! Selects all nodes from central drive of mass 1
cm,cap_edt3,node                                    ! Names the nodes of the selected area
emtgen,'cap_edt3','EMTElem_edt3',pad_edt3','uz',gap,gap/100   ! Generates TRANS126 elements
```

The next step is to apply mechanical and electrical boundary conditions for the static electromechanical analysis.

```
nsel,s,node,,tuning_eds4          ! Selects all nodes from the electrode
d,all,all,0,,,,uy,uz              ! Sets motion DOF UX,UY,UZ of selected nodes to 0
nsel,s,node,,tuning_eds4          ! Selects all nodes from the electrode
d,all,volt,VTD                    ! Sets voltage DOF of selected nodes to the potential V_drive
nsel,s,node,,eds4                 ! Selects all nodes from the side drive in face of eds4
d,all,volt,V_mass                 ! Sets voltage DOF of selected nodes to the potential V_mass

nsel,s,node,,tuning_edt3          ! Selects all nodes from the electrode
d,all,all,0,,,,uy,uz              ! Sets motion DOF UX,UY,UZ of selected nodes to 0
nsel,s,node,,tuning_edt3          ! Selects all nodes from the electrode
d,all,volt,VTS                    ! Sets voltage DOF of selected nodes to the potential V_drive
nsel,s,node,,edt3                 ! Selects all nodes from the side drive in face of eds4
d,all,volt,V_mass                 ! Sets voltage DOF of selected nodes to the potential V_mass

outres,all,all                    ! Write the solution data to database
ANTYPE,STATIC                     ! Analysis type = static
PSTRES,ON                         ! Pre-stress effects = on
SOLVE                             ! Solve the pre-stressed modal analysis
```

After pre-stressed modal analysis, the simulation moves to the harmonic analysis. Harmonic simulation is required to show response with damping coefficient and mode-matching condition with parametric excitation of the device.

```
ANTYPE,HARMIC,NEW                 ! Start a harmonic analysis
HROPT,FULL                        ! Harmonic analysis option = full
NSUBST, NST                       ! Number of sub-steps = as designated by NST
HARFRQ,A, B                       ! Swept frequency range = A to B
DMPRAT,damp_ratio                 ! Apply damping ratio = damp_ratio
KBC,1                             ! Stepped load step
```

Figure 115 illustrates the example of harmonic frequency sweep and the resonance responses. Figure 115(left, top) and Figure 115(left, bottom) show directional deformation of drive- and sense-modes, respectively, and the plotted surface areas demonstrates directional deformation of each mode. Figure 115(right) illustrates the resonance peaks of the modes which are completely mode-matched.

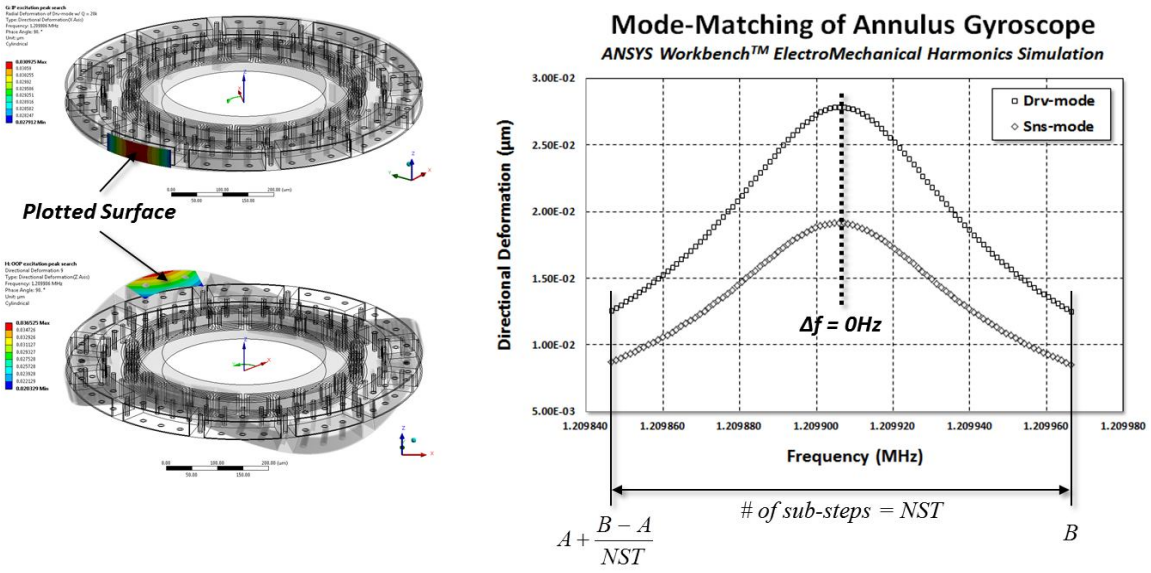

Figure 115: Example of ANSYS harmonic frequency sweep and plotted surface.

nsel,s,node,, pad_eds4	*! Selects all nodes from the electrode*
d,all,volt,V_drive	*! Sets voltage DOF of selected nodes to the potential V_drive*
nsel,s,node,,pad_edt3	*! Selects all nodes from the electrode*
d,all,volt,V_edt3_pad	*! Sets voltage DOF of selected nodes to the potential V_drive*

In three-dimensional space, rotation-rate is simulated by decomposing the desired axis of rotation into Cartesian coordinate (Figure 116). OMX, OMY, and OMZ represent rotation rate applied from X, Y, and Z-axis, respectively. The commands for rotation-applied simulation are shown below:

CORIOLIS,ON,,,OFF ! *Activate Coriolis effect to a rotating structure*

OMEGA, OMX, OMY, OMZ,0 ! *Constant rotation rate without rotating damping effect*

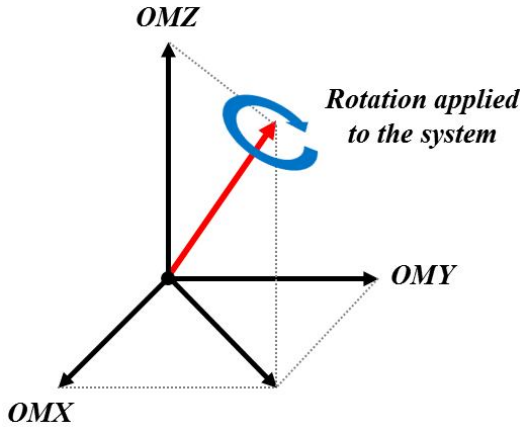

Figure 116: Rotation axis decomposed into three orthogonal axes.

REFERENCES

[1] Ayazi, F. Multi-DOF inertial MEMS: From gaming to dead reckoning. in Solid-State Sensors, Actuators and Microsystems Conference (TRANSDUCERS), 2011 16th International. 2011.

[2] Yazdi, N., F. Ayazi, and K. Najafi, Micromachined inertial sensors. Proceedings of the IEEE, 1998. **86**(8): p. 1640-1659.

[3] Zotov, S.A., et al. Chip-scale IMU using folded-mems approach. in Sensors, 2010 IEEE. 2010.

[4] Zotov, S.A., et al., Folded MEMS Pyramid Inertial Measurement Unit. Sensors Journal, IEEE, 2011. **11**(11): p. 2780-2789.

[5] Ayazi, F. and K. Najafi, High aspect-ratio combined poly and single-crystal silicon (HARPSS) MEMS technology. Microelectromechanical Systems, Journal of, 2000. **9**(3): p. 288-294.

[6] Johari, H. and F. Ayazi. Capacitive Bulk Acoustic Wave Silicon Disk Gyroscopes. in Electron Devices Meeting, 2006. IEDM '06. International. 2006.

[7] Jeong, Y., et al. Wafer-level vacuum-packaged triaxial accelerometer with nano airgaps. in Micro Electro Mechanical Systems (MEMS), 2013 IEEE 26th International Conference on. 2013.

[8] Sung, W.K., M. Dalal, and F. Ayazi. A mode-matched 0.9 MHZ single proof-mass dual-axis gyroscope. in Solid-State Sensors, Actuators and Microsystems Conference (TRANSDUCERS), 2011 16th International. 2011.

[9] Johari, H. and F. Ayazi. High-frequency capacitive disk gyroscopes in (100) and (111) silicon. in Micro Electro Mechanical Systems, 2007. MEMS. IEEE 20th International Conference on. 2007.

[10] Zhijun, Z., S. Jiyu, and W. Keyong. Study on Technology of Orientation and North-Finding Based on Fiber Optic Gyroscope. in Mechatronics and Automation, 2007. ICMA 2007. International Conference on. 2007.

[11] Moslehi, B., et al. Low-cost and compact fiber-optic gyroscope with long-term stability. in Aerospace Conference, 2011 IEEE. 2011.

[12] Ayazi, F. and K. Najafi, A HARPSS polysilicon vibrating ring gyroscope. Microelectromechanical Systems, Journal of, 2001. **10**(2): p. 169-179.

[13] Guohong, H. and K. Najafi. A single-crystal silicon vibrating ring gyroscope. in Micro Electro Mechanical Systems, 2002. The Fifteenth IEEE International Conference on. 2002.

[14] Zaman, M.F., A. Sharma, and F. Ayazi, The Resonating Star Gyroscope: A Novel Multiple-Shell Silicon Gyroscope With Sub-5 deg/hr Allan Deviation Bias Instability. Sensors Journal, IEEE, 2009. **9**(6): p. 616-624.

[15] Zaman, M.F., et al. The resonating star gyroscope. in Micro Electro Mechanical Systems, 2005. MEMS 2005. 18th IEEE International Conference on. 2005.

[16] Pai, P., et al. MEMS-based hemispherical resonator gyroscopes. in Sensors, 2012 IEEE. 2012.

[17] Yan, X., et al. Precision curved micro hemispherical resonator shells fabricated by poached-egg micro-molding. in Sensors, 2012 IEEE. 2012.

[18] Cho, J., J.A. Gregory, and K. Najafi. Single-crystal-silicon vibratory cylinderical rate integrating gyroscope (CING). in Solid-State Sensors, Actuators and Microsystems Conference (TRANSDUCERS), 2011 16th International. 2011.

[19] Mohammad Faisal Zaman, A.S., Zhili Hao, and Farrokh Ayazi, A Mode-Matched Silicon-Yaw Tuning-Fork Gyroscope With Subdegree-Per-Hour Allan Deviation Bias Instability. Journal of Microelectromechanical Systems, 2008. **17**(6): p. 1526-1536.

[20] Zaman, M.F., et al., A Mode-Matched Silicon-Yaw Tuning-Fork Gyroscope With Subdegree-Per-Hour Allan Deviation Bias Instability. Microelectromechanical Systems, Journal of, 2008. **17**(6): p. 1526-1536.

[21] Gallacher, B.J., Principles of a Micro-Rate Integrating Ring Gyroscope. Aerospace and Electronic Systems, IEEE Transactions on, 2012. **48**(1): p. 658-672.

[22] Gallacher, B.J., et al., Initial Test Results from a 3-axis Vibrating Ring Gyroscope. Journal of Physics: Conference Series, 2006. **34**: p. 662-667.

[23] Harish, K.M., et al., Experimental investigation of parametric and externally forced motion in resonant MEMS sensors. Journal of Micromechanics and Microengineering, 2009. **19**(1): p. 015021.

[24] Hu, Z.X., et al., A parametrically amplified MEMS rate gyroscope. Sensors and Actuators A: Physical, 2011. **167**(2): p. 249-260.

[25] Greiff, P., et al. Silicon monolithic micromechanical gyroscope. in Solid-State Sensors and Actuators, 1991. Digest of Technical Papers, TRANSDUCERS '91., 1991 International Conference on. 1991.

[26] Bernstein, J., et al. A micromachined comb-drive tuning fork rate gyroscope. in Micro Electro Mechanical Systems, 1993, MEMS '93, Proceedings An Investigation of Micro Structures, Sensors, Actuators, Machines and Systems. IEEE. 1993.

[27] Clark, W.A., R. T. Howe, and R. Horowitz, Surface Micromachined Z-axis Vibratory Rate Gyroscope. Digest of Solid-State Sensors and Actuator Workshop, 1996.

[28] Juneau, T., A.P. Pisano, and J.H. Smith. Dual axis operation of a micromachined rate gyroscope. in Solid State Sensors and Actuators, 1997. TRANSDUCERS '97 Chicago., 1997 International Conference on. 1997.

[29] Geiger, W., et al., The silicon angular rate sensor system DAVED®. Sensors and Actuators A: Physical, 2000. **84**(3): p. 280-284.

[30] Sato, H., et al., Improvement of sensing and actuating property of parallel beam gyroscope. Micromechatronics and Human Science, 1999, p. 249-254.

[31] Bhadbhade, V., N. Jalili, and S. Nima Mahmoodi, A novel piezoelectrically actuated flexural/torsional vibrating beam gyroscope. Journal of Sound and Vibration, 2008. **311**(3-5): p. 1305-1324.

[32] Sato, H., et al., Suppression of mechanical coupling for parallel beam gyroscope. Robotics and Automation, 2000, p. 3939-3944.

[33] Sato, H., et al., Analysis of parallel beam gyroscope. Robotics and Automation, 1999, p. 1632-1637.

[34] Sato, H., et al. Improvement of sensing and actuating property of parallel beam gyroscope. in Micromechatronics and Human Science, 1999. MHS '99. Proceedings of 1999 International Symposium on. 1999.

[35] Sato, H., et al., Parallel-beam sensor/actuator unit and its application to the gyroscope. Mechatronics, IEEE/ASME Transactions on, 2000. **5**(3): p. 266-272.

[36] Dao, D., et al., A dual axis gas gyroscope based on convective and thermo-resistive effects in silicon with low thermal-induced stress sensing element, MEMS 2006, p. 594-597.

[37] Dau, V.T., et al., Simulation and fabrication of a convective gyroscope. IEEE Sensors Journal, 2008, p. 1530-1538.

[38] Dau, V.T., et al., Development of a dual-axis thermal convective gas gyroscope. Journal of Micromechanics and Microengineering, 2006. **16**(7): p. 1301-1306.

[39] Zhu, R., et al., Micromachined gas inertial sensor based on convection heat transfer. Sensors and Actuators A: Physical, 2006. **130-131**: p. 68-74.

[40] Lutz, M., et al. A precision yaw rate sensor in silicon micromachining. in Solid State Sensors and Actuators, 1997. TRANSDUCERS '97 Chicago., 1997 International Conference on. 1997.

[41] Acar, C. and A.M. Shkel, An approach for increasing drive-mode bandwidth of MEMS vibratory gyroscopes. Microelectromechanical Systems, Journal of, 2005. **14**(3): p. 520-528.

[42] Lee, S.H., et al. A Low-Power Oven-Controlled Vacuum Package Technology for High-Performance MEMS. in Micro Electro Mechanical Systems, 2009. MEMS 2009. IEEE 22nd International Conference on. 2009.

[43] Trusov, A.A., et al. High-Q and wide dynamic range inertial MEMS for north-finding and tracking applications. in Position Location and Navigation Symposium (PLANS), 2012 IEEE/ION. 2012.

[44] Prikhodko, I.P., A.A. Trusov, and A.M. Shkel. North-finding with 0.004 radian precision using a silicon MEMS quadruple mass gyroscope with Q-factor of 1 million. in Micro Electro Mechanical Systems (MEMS), 2012 IEEE 25th International Conference on. 2012.

[45] Prikhodko, I.P., et al. Sub-degree-per-hour silicon MEMS rate sensor with 1 million Q-factor. in Solid-State Sensors, Actuators and Microsystems Conference (TRANSDUCERS), 2011 16th International. 2011.

[46] Prikhodko, I.P., et al. Foucault pendulum on a chip: angle measuring silicon MEMS gyroscope. in Micro Electro Mechanical Systems (MEMS), 2011 IEEE 24th International Conference on. 2011.

[47] Trusov, A.A., et al. Ultra-high Q silicon gyroscopes with interchangeable rate and whole angle modes of operation. in Sensors, 2010 IEEE. 2010.

[48] Ayazi, F. and K. Najafi. Design and fabrication of high-performance polysilicon vibrating ring gyroscope. in Micro Electro Mechanical Systems, 1998. MEMS 98. Proceedings., The Eleventh Annual International Workshop on. 1998.

[49] Wang-kyung, S., M. Dalal, and F. Ayazi. A 3MHz spoke gyroscope with wide bandwidth and large dynamic range. in Micro Electro Mechanical Systems (MEMS), 2010 IEEE 23rd International Conference on. 2010.

[50] Gallacher, B.J., J.S. Burdess, and A.J. Harris, Principles of a three-axis vibrating gyroscope. Aerospace and Electronic Systems, IEEE Transactions on, 2001. **37**(4): p. 1333-1343.

[51] Hu, Z.X., et al. Precision mode matching of MEMS gyroscope by feedback control. in Sensors, 2011 IEEE. 2011.

[52] IEEE Standard for Inertial Systems Terminology. IEEE Std 1559-2009, 2009: p. c1-30.

[53] IEEE Standard Specification Format Guide and Test Procedure for Single-Axis Laser Gyros. IEEE Std 647-2006 (Revision of IEEE Std 647-1995), 2006: p. 0_1-83.

[54] Zaman, M.F., Degree-per-hour mode-matched micromachined silicon vibratory gyroscopes, in Electrical and Computer Engineering2008, Georgia Institute of Technology: Atlanta.

[55] Geen, J.A., et al. Single-chip surface-micromachined integrated gyroscope with 50°/hour root allan variance. in Solid-State Circuits Conference, 2002. Digest of Technical Papers. ISSCC. 2002 IEEE International. 2002.

[56] www.analog.com.

[57] www.invensense.com.

[58] Meirovitch, L., Analytical methods in vibrations. 1967.

[59] Zhili, H., S. Pourkamali, and F. Ayazi, VHF single-crystal silicon elliptic bulk-mode capacitive disk resonators-part I: design and modeling. Microelectromechanical Systems, Journal of, 2004. **13**(6): p. 1043-1053.

[60] Shah, J., et al. CMOS ASIC for MHz silicon BAW gyroscope. in Circuits and Systems, 2008. ISCAS 2008. IEEE International Symposium on. 2008.

[61] Sharma, A., M.F. Zaman, and F. Ayazi. A 104dB SNDR Transimpedance-based CMOS ASIC for Tuning Fork Microgyroscopes. in Custom Integrated Circuits Conference, 2006. CICC '06. IEEE. 2006.

[62] Sharma, A., M.F. Zaman, and F. Ayazi. A Smart Angular Rate Sensor System. in Sensors, 2007 IEEE. 2007.

[63] Pourkamali, S., H. Zhili, and F. Ayazi, VHF single crystal silicon capacitive elliptic bulk-mode disk resonators-part II: implementation and characterization. Microelectromechanical Systems, Journal of, 2004. **13**(6): p. 1054-1062.

[64] Gabrielson, T.B., Mechanical-thermal noise in micromachined acoustic and vibration sensors. Electron Devices, IEEE Transactions on, 1993. **40**(5): p. 903-909.

[65] Ayazi, F. MEMS and microsystems for navigation, sensing, and spectral processing. in Micro-NanoMechatronics and Human Science (MHS), 2012 International Symposium on. 2012.

[66] Trusov, A.A., et al., Low-Dissipation Silicon Tuning Fork Gyroscopes for Rate and Whole Angle Measurements. Sensors Journal, IEEE, 2011. **11**(11): p. 2763-2770.

[67] Zhili, H., et al. Energy Loss Mechanisms in a Bulk-Micromachined Tuning Fork Gyroscope. in Sensors, 2006. 5th IEEE Conference on. 2006.

[68] Zhili, H. and F. Ayazi. Support loss in micromechanical disk resonators. in Micro Electro Mechanical Systems, 2005. MEMS 2005. 18th IEEE International Conference on. 2005.

[69] Abdolvand, R., et al. Thermoelastic damping in trench-refilled polysilicon resonators. in TRANSDUCERS, Solid-State Sensors, Actuators and Microsystems, 12th International Conference on, 2003. 2003.

[70] Abdolvand, R., et al., Quality factor in trench-refilled polysilicon beam resonators. Microelectromechanical Systems, Journal of, 2006. **15**(3): p. 471-478.

[71] Pourkamali, S., et al., High-Q single crystal silicon HARPSS capacitive beam resonators with self-aligned sub-100-nm transduction gaps. Microelectromechanical Systems, Journal of, 2003. **12**(4): p. 487-496.

[72] Dulmet, B. Finite element analysis of activity-dips in BAW resonators and sensors. in Frequency Control Symposium and PDA Exhibition, 2002. IEEE International. 2002.

[73] Boyd, E.J. and D. Uttamchandani, Measurement of the Anisotropy of Young's Modulus in Single-Crystal Silicon. Microelectromechanical Systems, Journal of, 2012. **21**(1): p. 243-249.

[74] Hopcroft, M.A., W.D. Nix, and T.W. Kenny, What is the Young's Modulus of Silicon? Microelectromechanical Systems, Journal of, 2010. **19**(2): p. 229-238.

[75] www.okmetic.com.

[76] Mehregany, M., Three-axis accelerometers. US Patent 7,578,189 B1, 2009.

[77] Zaman, M.F., A. Sharma, and F. Ayazi. High Performance Matched-Mode Tuning Fork Gyroscope. in Micro Electro Mechanical Systems, 2006. MEMS 2006 Istanbul. 19th IEEE International Conference on. 2006.

VITA

WANG-KYUNG SUNG

Wang-Kyung Sung was born in Seoul, South Korea, on October 28, 1980. He received B.S. degree in Electrical and Computer Engineering in 2006 with honors from the Hanyang University, Seoul, South Korea. He came to US in 2007 and received his Ph.D from the School of Electrical and Computer Engineering from the Georgia Institute of Technology, Atlanta, GA, in 2013. From August 2012 to August 2013, during his grad-years, he worked for Qualtré Inc. in Marlborough, MA, as an internship student for the design and characterization of high-frequency multi-axis gyroscopes and foundry management. His research interests include the design of MEMS gyroscopes and MEMS process development for inertial measurement unit (IMU) integration.